# IN SITU NMR METHODS FOR LITHIUM-ION BATTERIES

# THE DEVELOPMENT AND APPLICATION OF IN SITU NMR METHODS FOR LITHIUM-ION BATTERIES

BY ANNICA I. FREYTAG, B. SC., M. SC.

A Thesis Submitted to the School of Graduate Studies in Partial Fulfilment of
the Requirements for the Degree Doctor of Philosophy

McMaster University DOCTOR OF PHILOSOPHY (2020) Hamilton, Ontario (Chemistry)

TITLE: The Development and Application of In Situ NMR Methods for Lithium-Ion Batteries

AUTHOR: Annica I. Freytag, B.Sc. (Universität Potsdam), M.Sc. (Queen's University)

SUPERVISOR: Professor Gillian R. Goward

NUMBER OF PAGES: ix, 173

## Lay Abstract

Lithium-ion batteries have gained a lot of attention over the past few decades, especially in the automotive industry. Some of the main challenges, which persist today, include the moderate driving range and fast-charging capabilities of electric vehicles.

This work introduces different nuclear magnetic resonance (NMR) techniques which can shed light onto the inner-workings of a battery by monitoring them in real-time. One material of interest is silicon as it is a promising candidate to overcome the issues concerning driving range and fast-charge. This, however, requires the development of new characterization techniques. Three different battery cells are introduced, which all serve a different purpose to gain knowledge that can advance the lithium-ion battery field.

# Abstract

This body of work is tackling some of the challenges in the field of lithium-ion batteries (LIBs) for electric vehicles through in situ nuclear magnetic resonance (NMR). In situ NMR allows for the simultaneous monitoring of both liquid and solid components (electrolyte, cathode, anode, separator) and provides timely data acquisition making it a great method to extract real-time information about structural changes, degradation products and failure mechanisms in batteries.

A combined in situ $^{7}$Li NMR and ex situ $^{29}$Si magic-angle spinning (MAS) NMR study on silicon and silicon monoxide was used to compare structural differences in these anode materials using a custom-made in situ cell. Some key differences between the two materials were obtained, highlighting the importance of in situ NMR to be used for identifying phases, which are not present under ex situ conditions. In addition, fast charging of silicon anodes was investigated to gain a better understanding of their performance at high current rates. Magnetic resonance imaging was also implemented to localize lithium metal deposition under these conditions, which was made possible by a unique in situ parallel-plate resonator setup. Finally, the successful development of a novel in situ MAS NMR technique is introduced, which for the first time allows for an in situ analysis of a LIB under MAS. This strategy paves the way toward acquisition of valuable in situ data on the formation and transformations of metastable states within the active materials of both electrodes; data that is difficult to obtain from static in situ NMR experiments alone.

# Acknowledgements

First and foremost special thanks goes to my supervisor Dr. Gillian Goward who has given me the creative freedom over the past four years to work on interesting projects and present my work all over the world.

In addition, I would like to express my deepest thanks to my committee member Dr. Gianluigi Botton and Dr. Giuseppe Melacini for their support throughout my PhD and for their helpful advice during our committee meetings.

To past and present group member of the Goward Group for all their support inside and outside the lab, thank you! You were the pillars of strength when needed.

To the Brains: Dr. David Bazak, Dr. Adam MacIntosh, Dr. Danielle Smiley, Dr. Blossom Yan and Christopher Franko. Thank you for all the insightful (and not so insightful) conversations over the past years.

Thank you Dr. Kris Harris, Dr. Sergey Krachkovskiy, Dr. Allen Pauric and Dr. Kevin Sanders for being my mentors.

I would also like to thank my family for their support since day one. I would not be the person I am today without the endless trust from you.

To Sean, my partner and soon-to-be husband: You deserve all the acknowledgements in the world. Thank you for always being there for me, cheering me up with your infectious laugh and for being just the best in general.

# Contents

# List of Figures

# List of Tables

# List of Abbreviations and Symbols

| | |
|---|---|
| $\alpha$ | energy level for $m = +\frac{1}{2}$ (Chapter 2.1) |
| $\beta$ | energy level for $m = -\frac{1}{2}$ (Chapter 2.1) |
| $\beta$ | flip angle |
| $\hat{\boldsymbol{\mu}}$ | magnetic moment |
| $\hat{\boldsymbol{S}}$ | spin angular momentum |
| $\boldsymbol{\sigma}$ | nuclear shielding tensor |
| $\boldsymbol{I}$ | spin I |
| $\boldsymbol{k}$ | reciprocal space vector |
| $\boldsymbol{S}$ | spin S |
| $\chi_s^e$ | Pauli susceptibility |
| $\Delta E$ | separation of energy levels |
| $\Delta$ | anisotropy (Chapter 2.3) |
| $\Delta$ | diffusion time |
| $\delta$ | gradient pulse length |
| $\eta$ | asymmetry parameter |
| $\eta_Q$ | asymmetry parameter |
| $\gamma$ | gyromagnetic ratio |
| $\gamma_I$, $\gamma_S$ | gyromagnetic constant for spin I and S |
| $\hat{H}_Q$ | first-order quadrupolar Hamiltonian |

| | |
|---|---|
| $\hat{H}_D$ | interaction Hamiltonian for two spins |
| $\hat{I}_+$, $\hat{I}_-$, $\hat{S}_+$, $\hat{S}_-$ | raising (+) and lowering (-) operator for spin I and S |
| $\hat{I}_z$, $\hat{S}_z$ | nuclear spin angular momentum operators for spin I and S along the z-axis |
| $\hbar$ | reduced Planck constant |
| $\mu_0$ | vacuum permeability constant |
| $\omega_0$ | Larmor frequency |
| $\omega_1$ | RF nutation frequency |
| $\omega_S$ | Larmor frequency with shielding contributions |
| $\sigma_{iso}$ | isotropic parameter |
| $\theta, \phi$ | angles which relate the orientation of the molecule to $\vec{B}_0$ along the z-axis |
| $\theta_R$ | magic angle |
| $\vec{\mu}_1$, $\vec{\mu}_2$ | two magnetic dipole moments |
| $\vec{B}_0$ | magnetic field strength of the applied field along the z-axis |
| $\vec{B}_1$ | applied RF field perpendicular to the $\vec{B}_0$ field |
| $\vec{B}_{\mathbf{eff}}$ | effective field |
| $\vec{G}$ | magnetic field gradient |
| $\vec{r}$ | vector between two dipoles |
| $C_Q$ | quadrupolar coupling constant |
| $D$ | diffusion coefficient |
| $e$ | charge of an electron |
| $E_D$ | dipolar coupling energy |
| $E_J$ | spin-spin coupling or J-coupling energy |
| $E_K$ | Knight shift energy |
| $E_m$ | energy levels |
| $E_P$ | paramagnetic energy |

| | |
|---|---|
| $E_Q$ | quadrupolar energy |
| $E_S$ | shielding energy |
| $E_z$ | Zeeman energy |
| $E_{NMR}$ | nuclear spin energy |
| $E_{RF}$ | RF field interaction |
| $F$ | Faraday constant |
| $g$ | gradient strength |
| $G_{max}$ | maximum gradient strength in units of G/cm |
| $I$ | spin quantum number |
| $I$, $I_0$ | signal intensity with and without attenuation |
| $k_B$ | Boltzmann constant |
| $M$ | molecular weight of active material |
| $m$ | magnetic quantum number |
| $M_0$ | magnetization vector |
| $M_x$ | x-component of $M_0$ |
| $M_y$ | y-component of $M_0$ |
| $m_{\mathbf{negative}}$ | active mass of negative electrode |
| $m_{\mathbf{positive}}$ | active mass of positive electrode |
| $M_{eq}$ | magnetization at equilibrium along the z-axis |
| $N$ | number of phase-encoded steps |
| $n$ | number of charge carriers |
| $N_\alpha$ | spin state populations for $\alpha$ |
| $N_\beta$ | spin state populations for $\beta$ |
| $Q$ | electric quadrupolar moment |
| $Q_{\mathbf{discharge}}$ | discharge capacity |
| $q_{\mathbf{negative}}$ | specific capacity of negative electrode |

| | |
|---|---|
| $q_{\mathbf{positive}}$ | specific capacity of positive electrode |
| $Q_{theo}$ | theoretical capacity |
| $r$ | distance |
| $T_1$ | spin-lattice relaxation time constant |
| $t_1$ | time in the direct dimension |
| $T_2$ | spin-spin relaxation time constant |
| $t_2$ | time in the indirect dimension |
| $t_p$ | pulse length, gradient pulse length |
| $U$ | interaction energy |
| $V_{XX}$, $V_{YY}$, $V_{ZZ}$ | tensor elements of the EFG |
| **+g, -g** | field gradients |
| **2D** | two-dimensional |
| **3D** | three-dimensional |
| **a-SiO** | silicon monoxide |
| **BMS** | bulk magnetic susceptibility |
| **BNC** | Bayonet Neill-Concelman |
| **C-rate** | current/charge rate |
| **CAD** | computer-aided design |
| **CEV** | combustion engine vehicle |
| **CMC** | carboxy(methyl)cellulose |
| **CSE** | composite solid-state electrolyte |
| **CSI** | chemical shift imaging |
| **DEC** | diethyl carbonate |
| **DI** | deionized |
| **DMC** | dimethyl carbonate |
| **DOS** | density of states |

| | |
|---|---|
| **EC** | ethylene carbonate |
| **EFG** | electric field gradient |
| **EV** | electric vehicle |
| **FEC** | fluoro ethylene carbonate |
| **FID** | free induction decay |
| **FOV** | field of view |
| **FT** | Fourier transform |
| **K** | Knight shift |
| **LCO** | lithium cobalt oxide ($LiCoO_2$) |
| **LFP** | lithium iron phosphate ($LiFePO_4$) |
| **Li** | lithium |
| **LIB** | lithium-ion battery |
| **LiFSI** | lithium bis(fluorosulfonyl) imide ($F_2LiNO_4S_2$) |
| **$LiPF_6$** | lithium hexafluorophosphate |
| **LiTFSI** | lithium bis(trifluoromethanesulfonyl)imide ($LiC_2F_6NO_4S_2$) |
| **LLTO** | $Li_{0.33}La_{0.55}TiO_3$ |
| **MAH** | magic-angle hopping |
| **MAS** | magic-angle spinning |
| **MAT** | magic-angle turning |
| **MATPASS** | magic-angle turning and phase-adjusted spinning sideband separation |
| **MRI** | magnetic resonance imaging |
| **Mw** | molecular weight |
| **N** | negative electrode |
| **NCA** | nickel cobalt aluminum oxide ($LiNi_{0.8}Co_{0.15}Al_{0.05}O_2$) |
| **NMC** | nickel manganese cobalt oxide ($LiNi_{0.33}Mn_{0.33}Co_{0.33}O_2$) |

| | |
|---|---|
| **NMC532** | $LiNi_{0.5}Mn_{0.3}Co_{0.2}O_2$ |
| **NMC622** | $LiNi_{0.6}Mn_{0.2}Co_{0.2}O_2$ |
| **NMR** | nuclear magnetic resonance |
| **P** | positive electrode |
| **PAS** | principal axis system |
| **PASS** | phase-adjusted spinning sideband separation |
| **PC** | propylene carbonate |
| **PE** | polymer electrolyte |
| **PEO** | polyethylene oxide |
| **PFG** | pulsed-field gradient |
| **PP** | parallel-plate |
| **RF** | radio-frequency |
| **S-ISIS** | scanning image-selected in situ spectroscopy |
| **SEI** | solid-electrolyte interphase |
| **SEM** | scanning electron microscopy |
| **Si** | silicon |
| **SN** | succino nitrile ($C_2H_4(CN)_2$) |
| **SOH** | state-of-health |
| **ssNMR** | solid-state NMR |
| **T** | temperature |
| **TEM** | transmission electron microscopy |
| **TTMSS** | Tris(trimethylsilyl)silane ($[(CH_3)_3Si]_3SiH$) |
| **VC** | vinylene carbonate |
| **XRD** | X-ray diffraction |
| **XX, YY, ZZ** | principal values of the shielding tensor |

## Declaration of Academic Achievement

Allen D. Pauric (ADP) designed the in situ NMR cell in Chapter 3 and performed the in situ $^{7}$Li NMR measurements on silicon and silicon monoxide. The ex situ $^{29}$Si NMR data was collected by ADP and Annica I. Freytag. ADP contributed to the initial technique development for the in situ cell design in Chapter 4 by developing the cellulose-based electrode synthesis procedure. Kristopher J. Harris assisted in the collection of MATPASS spectra for the in situ MAS NMR project. Kevin J. Sanders assisted in the collection of magnetic resonance images in Chapter 5. Nafiseh Zaker collected the scanning electron microscopy image of the silicon anode. Sergey Krachkovskiy developed the capillary parallel-plate resonator in situ cell used in Chapter 5. Hilal Al-Salih conducted the synthesis and electrochemical analysis of the polymer electrolytes as well as the conductivity study in Appendix A. All other technique development, data collection and analysis was performed by Annica I. Freytag.

## Chapter 1

# Introduction

## 1.1 Motivation

Over the past few decades, a rise in popularity of lithium-ion batteries (LIBs) has fuelled the automotive industry. LIBs were first introduced commercially in 1991 by Sony, and exhibit superior properties over other electrochemical storage devices due to their inherently larger energy density, power density and long cycle life.[1] This has lead to the successful development of commercial electric vehicles (EVs), which have shown an average annual increase of 60% in electric car stock worldwide with over 7.2 million units on the road in 2019.[2]

However, to be competitive with conventional combustion engine vehicles (CEVs), several challenges must be overcome. Namely, the cost, driving range and fast-charging capabilities of EVs are still inferior to CEVs. Although tremendous efforts have led to a decrease in battery cost by more than 85% since 2010[2], the challenges regarding driving range and fast-charging capabilities require fundamental research and clever engineering of all components in a LIB in order to achieve a comparable experience to CEVs. The driving range of an EV is largely dependent on the energy density of the electrode materials and is expected to reach around 350 km to 400 km by 2030.[2] In order to achieve these goals, the composition of LIBs has to be optimized. Current forerunners for cathode materials include intercalation oxides such as lithium cobalt oxide (LCO), nickel cobalt aluminum oxide (NCA), nickel manganese cobalt oxide (NMC) and lithium iron phosphate (LFP).[3] The balancing act between safety, performance and high capacity is crucial in choosing the optimal material. LCO shows great performance but suffers from a relatively low capacity ($140\,\mathrm{mA\,h\,g^{-1}}$). NMC and NCA can reach higher capacity values, $160\,\mathrm{mA\,h\,g^{-1}}$ to $170\,\mathrm{mA\,h\,g^{-1}}$ for NMC and $180\,\mathrm{mA\,h\,g^{-1}}$ to $200\,\mathrm{mA\,h\,g^{-1}}$ for NCA, but suffer from safety issues and resource limitations due to the high cost of Ni and Co. LFP is an excellent candidate for use in grid-storage because of its great cycling stability, great safety features and low cost.[4] Current research efforts for EV applications concentrate on minimizing the amount of Ni and Co to reduce cost and increase safety.

On the anode side, graphite is used in the majority of LIBs since the advent of LIBs. However, silicon-doped chemistries are slowly being implemented in order to increase the overall energy density. This does not come without obstacles as silicon undergoes a different lithiation mechanism than graphite, which makes it increasingly difficult to implement anodes with large silicon-doping levels.[5] In addition, fast-charging capabilities of LIBs and therefore EVs is still not optimal. Graphite suffers from slow lithium diffusion at high charge rates leading to lithium deposition on the anode surface, which can lead to detrimental results such as battery failure or thermal runaway.[6] This is even more pronounced at low temperatures, which leads to immense differences in charging time at varying temperatures. This is by no means a trivial challenge and requires optimization of not only the anode material but also the heat management system in an EV, as a large amount of heat can be released at high charging rates. In order to compete with CEVs, where refuelling usually takes no longer than five minutes, fast-charging capabilities have to be optimized.

The above mentioned challenges require research in a variety of different fields, ranging from materials design and characterization to engineering. This work is tackling some of the fundamental challenges in the field of LIBs for EVs through in situ NMR. In addition, advancement in in situ NMR techniques are introduced, which are designed in such a way that they can be used to answer relevant questions in the battery field.

## 1.2 Lithium-Ion Batteries

A LIB is a type of electrochemical cell which has the ability to store energy reversibly. Figure 1.1 shows a typical schematic of a LIB. In the most general sense it consists of an anode, cathode, separator and electrolyte. During charge, a current is applied to the cell which forces the lithium-ions to travel from the cathode to the anode. The separator is permeable to the ions but resistant to electrons to ensure that anode and cathode are not in electrical contact, which would lead to a failed battery caused by a short. The electrolyte serves as a transport medium for the lithium-ions, while the electrons are routed through an external circuit. The redox reaction occurring on both electrodes has to be reversible in order to allow for repeated charging and discharging of the battery. The theoretical capacity of an electrode material can be calculated using the following formula

$$Q_{theo} = \frac{nF}{3.6 \cdot M} \qquad \left[\frac{\mathrm{mAh}}{\mathrm{g}}\right] \tag{1.1}$$

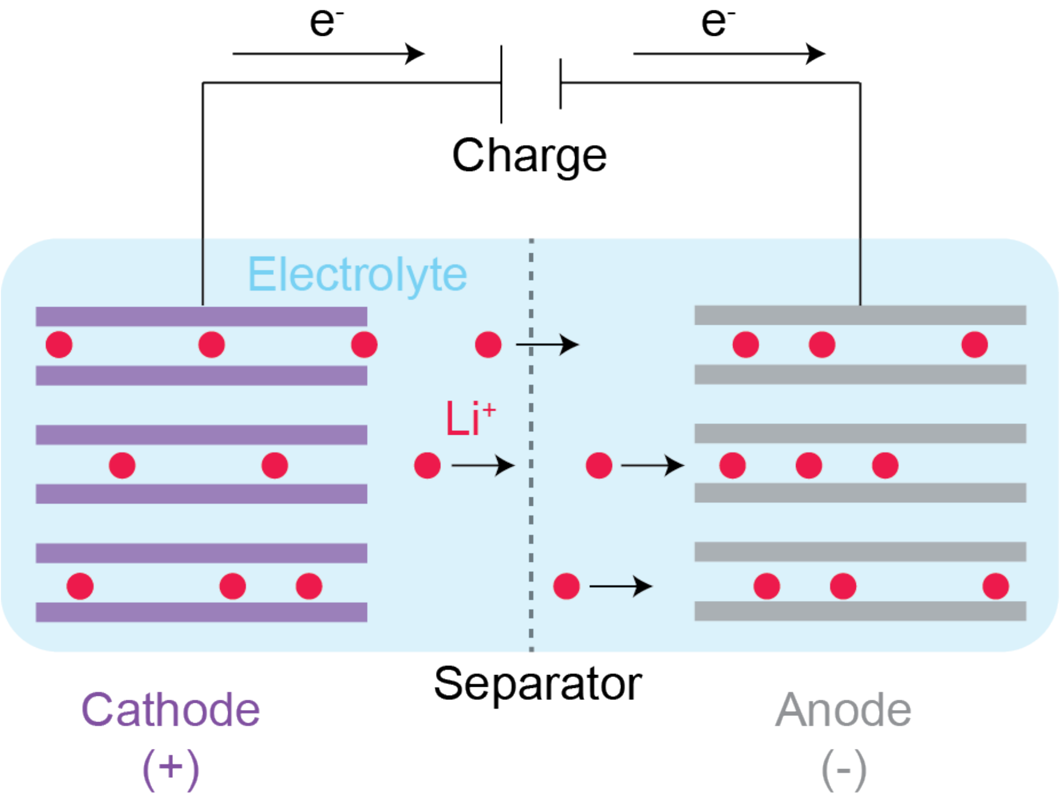

Figure 1.1: Schematic of a lithium-ion battery during charge. The lithium-ions move from the cathode (purple) to the anode (grey) while electrons move through an external circuit.

where $Q_{theo}$ is the theoretical capacity in mAh/g, $n$ the number of charge carriers, $F$ the Faraday constant in C/mol, and $M$ the molecular weight of the active material. It is evident that it is desirable to increase the number of charge carriers and to decrease the molecular weight of the active material in order to achieve a high capacity. Lithium-ions are monovalent, which limits the amount of charge carriers to one for LIBs. This is inferior to multivalent cations like $Be^{2+}$, $Al^{3+}$, $Zn^{2+}$, and $Mg^{2+}$. However, multivalent ions show sluggish diffusion making it challenging to design a battery on a competitive level to LIBs.[7] With the charge carrier limited to one, the other variable is the amount of lithium which can be incorporated in the active material.

In graphite anodes, the highest lithiated state is $LiC_6$ which corresponds to a theoretical capacity of $372\,\mathrm{mA\,h\,g^{-1}}$. This is relatively low compared to other anode materials. However, due to its low cost and remarkable cycling stability it is the preferred anode material for LIBs. Other anode materials, in particular silicon and lithium metal, are actively investigated as a possible replacement for graphite. They exhibit much higher theoretical capacities than graphite. Silicon undergoes an alloying mechanism with lithium and can therefore incorporate a larger amount of lithium per silicon. The lithiation mechanism of graphite and the current challenges of commercializing silicon anodes for LIBs is given in Section 1.3. Lithium metal, even though attractive due to its low electrode potential and high capacity, suffers from high reactivity with the electrolyte, uneven lithium deposition on the electrode surface upon cycling and as a result immense safety risks which can lead to battery failure and in the worst case thermal runaway.[8] However, with the rise in solid-state electrolytes and clever manipulation of the electrode interfaces, solid-state lithium batteries are slowly regaining prominence in the battery field.

Common cathode materials for LIBs include transition metal oxides like LCO, NCA, NMC and LFP. Table 1.1 summarizes the characteristics of the most common cathode materials. While LCO is still widely used in commercial batteries for hand-held devices (smartphones, laptops, etc.), high capacity and high power cathodes (like NCA and NMC) are on the forefront for EV applications. NMC has gained popularity over the years as it can be cycled to greater voltages (up to 4.7 V) and it exhibits a higher experimental capacity compared to other cathode materials.[9] The work in the following chapters concentrates on the anode side of LIBs. For a more detailed review on cathode materials the reader is referred to multiple great review articles elsewhere.[3,9–11]

| Electrode Material | Average potential vs. Li/Li$^+$ (V) | Specific Capacity (mAh/g) | Advantages | Disadvantages |
|---|---|---|---|---|
| LCO | 3.9 | 140 | Performance | Cost and resource limitations of Co, low capacity |
| NCA | 3.8 | 180-200 | High capacity and voltage, excellent rate performance | Safety, cost and resource limitations of Ni and Co |
| NMC111 | 3.8 | 160-170 | High voltage, moderate safety | Cost and resource limitations of Ni and Co |
| LFP | 3.5 | 170 | excellent safety, cycling, and rate capability, low cost and abundance of Fe, low toxicity | Low voltage and capacity, low energy density |

Table 1.1: Potential, specific capacities, advantages and disadvantages of common cathode materials for LIBs. Table adapted from Kam et al. Material Matters, 2012, 7, 56-60[12]

Of similar importance is the choice of an adequate electrolyte for LIBs. The electrolyte functions as the transport medium for lithium-ions between the cathode and the anode. It therefore has to exhibit excellent diffusive and conductive properties. In addition, safety is a major factor when it comes to choosing the optimal electrolyte. Preferably, a non-toxic, non-flammable and oxidatively stable electrolyte is desired. Lithium hexafluorophosphate ($LiPF_6$) dissolved in carbonate solvents like ethylene carbonate (EC), diethyl carbonate (DEC) and dimethyl carbonate (DMC) is a standard liquid electrolyte for LIBs. One important characteristic of liquid electrolytes like $LiPF_6$ is that it forms a thin passivating layer on the anode (e.g. graphite) during the first electrochemical cycle. This layer consists of electrolyte breakdown products, which is known as the solid-electrolyte interphase (SEI). It contains mainly lithium carbonates, oxides and fluorides depending on the composition of the electrolyte.[13] This elusive layer is critical in obtaining excellent cycling stability in LIBs and is a major field of interest in the battery community.[14] By introducing electrolyte additives like fluoro ethylene carbonate (FEC) or vinylene carbonate (VC), the SEI can be modified to enhance its stability.[15] This is of great importance when it comes to optimizing the SEI for other anode materials like silicon.

Other types of electrolyte such as polymer and solid state electrolytes are actively investigated as a replacement for liquid electrolytes.[16,17] However, one of the main issues in the implementation of those kinds of electrolytes is the interfacial chemistry between the electrolyte and the electrodes, because it is difficult to obtain a similarly stable SEI compared to LIBs prepared with liquid electrolyte.[17] Polymer electrolytes (PEs) usually consist of a polymer matrix such as polyethylene oxide (PEO) and a lithium-conducting ceramic and/or salt. The salt (e.g., LiTFSI) is dissolved into the polymer matrix and acts as the lithium conductor. PEs show great thermal stability and flexibility and are therefore safer to use than their liquid counterparts. However, the ionic conductivity of PEs is inferior to liquid electrolytes due to their rigid structure. Manipulation of the PE composition by introducing ceramic solid electrolytes and by increasing the amorphicity of the polymeric network can improve the performance of PEs immensely. In Appendix A a novel quaternary PE is introduced, which utilizes succino nitrile (SN) to increase the amount of amorphous domains in the polymeric structure leading to a well-connected conductive network. In addition, a ceramic solid state electrolyte

($Li_{0.33}La_{0.55}TiO_3$, LLTO) is incorporated to improve the mechanical properties and ionic conductivity of the PE.[18]

It is evident from the description of LIBs above, that no perfect combination of anode, cathode, separator and electrolyte exists. In addition, a variety of other factors (e.g. pressure, temperature and upscaling) which have a tremendous influence on the workings of a LIB were excluded from this introduction. It is therefore of utmost importance to pursue all different kinds of avenues in order to advance LIB technology.

## 1.3 Anode Materials Studied in This Thesis

### 1.3.1 Graphite

Graphite is the most commonly used anode material for LIBs. It lithiates through an intercalation mechanism with the highest lithiated stage corresponding to $LiC_6$. The volume expansion during lithiation is limited to 13%, which is one major reason of the great stability of this anode material as it mitigates cracking of the electrode surface.[19] Graphite's excellent cycling performance over hundreds of cycles is also due to the formation of a protective SEI layer, which forms during the first discharge.[14] The lithiation mechanism in graphite occurs in stages, with the main classifications being the dilute and concentrated stages.[20] Figure 1.2 summarizes the intercalation steps in graphite. The dilute stages correspond to $LiC_{36}$, $LiC_{27}$ and $LiC_{18}$ and are commonly described by the interlayer spacing of occupied to unoccupied graphene layers in the structure. As an example, in stage 2 there are two graphene layers between each occupied layer. The concentrated stages correspond to $LiC_{12}$ and $LiC_6$. One main disadvantage of graphite anodes is their poor performance under fast-charging conditions. This becomes even more problematic at low temperatures, where this effect is enhanced.[21,22]

In graphite, lithium plating occurs when the current rate (or C-rate) is larger than the rate of lithium diffusion into the graphite structure. The C-rate of a battery is defined as the amount of hours it takes to reach the full capacity of a cell. As an example, if a LIB has a capacity of 10 mA h, in order to reach a full charge in 10 hours, a current of 1 mA has to be applied. This is known as a C/10 charge rate. To reach the same capacity within one hour, the current has to be increased to 10 mA resulting in a 1C charge rate. Figure 1.3 illustrates the current rate effects in graphite anodes.[23] It shows that at moderate charge rates, lithium (Li) can intercalate into the graphite network (i, ii). However, at high currents Li is plated onto the surface as metallic Li (iv), which is partially reversible on discharge (iii). Interestingly, some of the plated Li can diffuse into graphite during a rest period, when no current is applied but a direct contact between the Li metal and graphite is given. The irreversibly plated lithium can cause long-term issues, such as an increase in cell resistance,

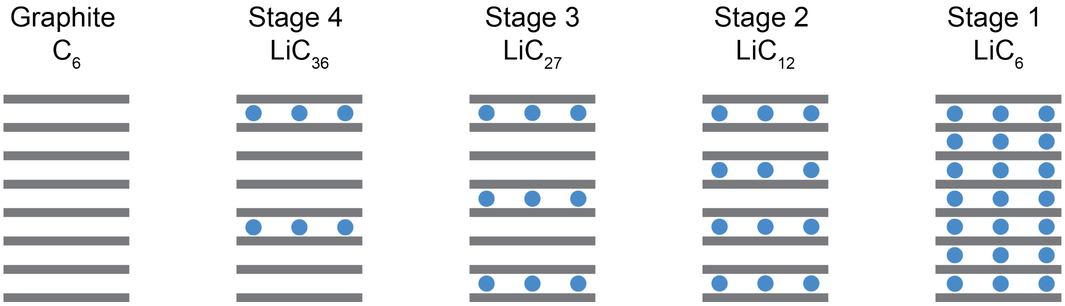

Figure 1.2: Schematic of the dilute and concentrated stages during graphite lithiation. Purple circles indicate lithium-ions and grey bars indicate graphene layers. $LiC_{36}$ and $LiC_{27}$ correspond to dilute stages, whereas $LiC_{12}$ and $LiC_6$ correspond to concentrated stages.

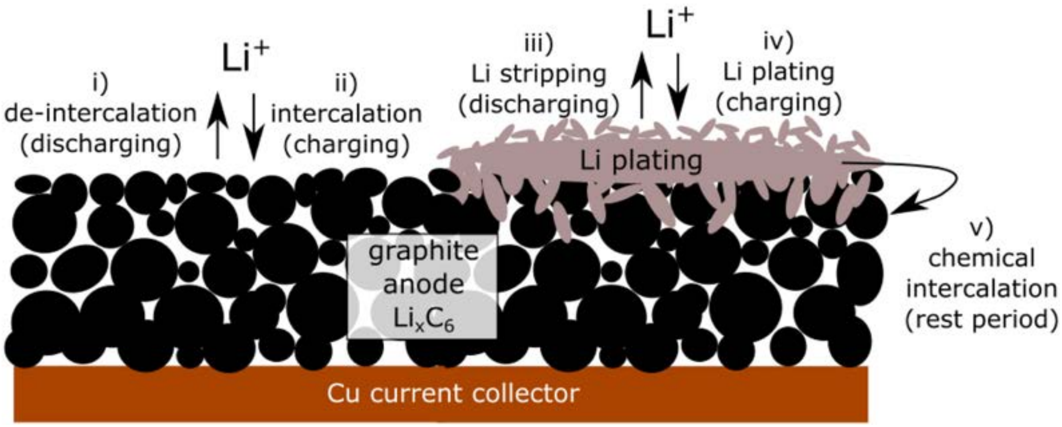

Figure 1.3: Illustration of different mechanisms during charging of graphite anodes (i) Li de-intercalation from lithiated graphite (ii) Li intercalation into graphite during charging (iii) removal of plated lithium during discharge (iv) Li plating during charge at high currents (v) Diffusion of lithium into the graphite network during a rest period. Reprinted with permission from Electrochimica Acta, 2017,230, 454 - 460[23]. Copyright © 2017, Elsevier.

electrolyte degradation and loss of lithium inventory. Different techniques exist to detect lithium plating under fast-charging conditions including high-precision coulometry,[24] and the use of a reference electrode.[25,26] A reference electrode is an electrode of known potential, which does not change significantly during cycling of a battery. It is used to get accurate potential values for anode and cathode in a full-cell format. In order to avoid lithium deposition on the anode surface, it is important to keep the anode potential above the plating potential of lithium (0 V vs. $Li/Li^+$). Plated lithium can deposit in different ways. The two main morphologies are the dendritic needle-like and the film-like flat type. The dendritic type is much more dangerous as it can lead to piercing of the separator, which can cause a short-circuit. However, industry is shifting towards doping the graphite anode with small loadings of silicon, which not only has a higher energy density, but it is also less prone to lithium plating. High currents can be applied to silicon anodes without suffering from lithium deposition.[27]

A closer look at the effects of high charge currents on pure silicon anodes in Chapter 5 will give more insight into the plating behaviour of such electrodes.

### 1.3.2 Silicon

In order to increase the capacity of LIBs, new and emerging materials are investigated which theoretically exhibit a larger capacity than the commercially used materials. In Chapter 3 and 5, silicon (Si) and silicon-containing anodes are looked at in more detail as they show higher specific capacities than graphite; $3578\,\mathrm{mA\,h\,g^{-1}}$ for silicon versus $372\,\mathrm{mA\,h\,g^{-1}}$ for graphite. This is due to the different lithiation mechanism of these materials.[28]

Silicon undergoes an alloying mechanism with lithium. The Li-Si phase diagram reveals several crystalline lithium silicide phase, namely $Li_{12}Si_7$, $Li_7Si_3$, $Li_{13}Si_4$, and $Li_{21}Si_5$, which are illustrated in Figure 1.4.[29] Interestingly, during electrochemical cycling the initial crystalline silicon network undergoes a phase transition to form amorphous lithium silicides instead of crystalline ones. At the end of discharge a crystalline phase appears corresponding to $Li_{15}Si_4$. In addition, the crystalline phase $Li_{21}Si_5$ is absent during electrochemical lithiation, limiting the capacity to $3578\,\mathrm{mA\,h\,g^{-1}}$ corresponding to 3.75 Li per Si. The amorphous silicide phases formed electrochemically can be grouped into three types. Ot low states of lithiation, the silicon network gets broken down into large Si clusters with isolated Li (phase 1). These clusters are broken down further at around $Li_2Si$, where they form smaller Si clusters (phase 2). The highest electrochemically lithiated phase is $Li_{15}Si_4$ (phase 3), where all Si clusters are broken up and only isolated Si are present. Phase 3 is known to be the major culprit for the dramatic volume expansion occurring in Si anodes.[29,30] This

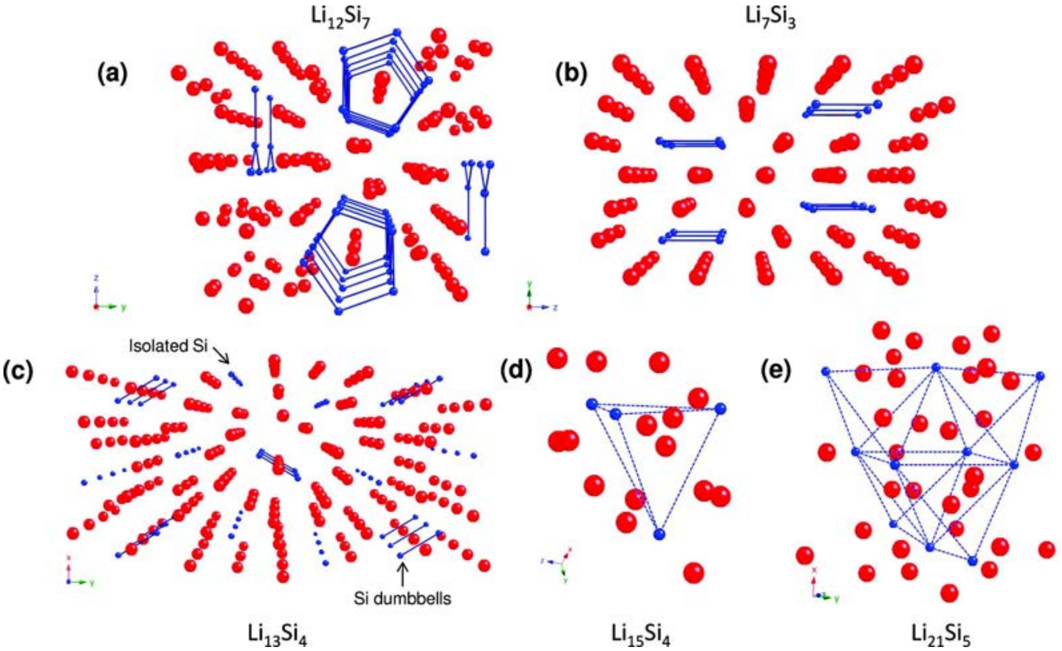

Figure 1.4: Structural representations of $Li_{12}Si_7$, $Li_7Si_3$, $Li_{13}Si_4$, $Li_{15}Si_4$, and $Li_{21}Si_5$. Reprinted with permission from The Journal of the American Chemical Society, 2009, 131, 26, 9239-9249[29]. Copyright © 2009, American Chemical Society.

is due to the large uptake in lithium, which leads to repeated expansion and contraction of the electrode material leads to breakdown and cracking of the electrode surface.[31] This breakdown does not only cause a disruption of the conductive network but also has a negative effect on the SEI. In graphite the SEI is stable and is crucial for a working battery. The SEI on silicon anodes is more elusive and expected to be of dynamic nature, where it is constantly reforming during cycling. This is partially due to the "breathing" of the anode with each cycle, which induces cracks that reveal pristine silicon surfaces.[32]

A vast amount of research has gone into finding ways to mitigate the volume expansion of silicon in electrochemical cells, e.g., by nano-sizing silicon particles,[33–35] optimizing binder materials and electrolyte additives,[36–38] or by limiting the potential range (in order to avoid the formation of the $Li_{3.75}Si$ phase, which exhibits the largest volume expansion).[39–41] In Chapter 3 silicon monoxide is investigated through in situ and ex situ NMR spectroscopy as it forms irreversible silicates, which mitigate the volumetric expansion and therefore improve the long-term cycling performance of these types of materials.[42]

## 1.4 In Situ Methods for Battery Materials

In situ techniques are important in understanding the electrochemical processes in a working LIB and have gained popularity due to their unique ability to monitor physical and chemical changes in batteries in real time.[43] The term in situ has Latin origin and can be translated as "in position", which in this case means that the battery is analyzed without being disassembled. An extension to in situ analysis is the so-called "in operando" analysis, which deals with the analysis of batteries while being under operating conditions (a charging or discharging current is applied). Several different techniques exist and are constantly being improved. In situ measurements of batteries are difficult to implement as they require the design of specialized in situ cells to fit the corresponding analysis technique.

X-ray diffraction (XRD) is commonly used to analyze the crystallographic structures of materials and has been adapted to investigate LIBs through an in situ strategy utilizing modified coin cell designs (and other types of designs) with a window made of X-ray transparent material. Some interesting studies have been performed on a variety of cathode materials in the past.[44–46] One study focussed on the influence of vanadium additives in a $LiFePO_4$ cathode. They found that by adding small amounts of vanadium, a significant improvement of the rate capability was apparent due to the formation of less non-crystalline phases in the case of vanadium doping.[44] In addition, in situ XRD can provide insights into the alloying mechanism of silicon anodes. Although, most intermediate phases are of amorphous nature during electrochemical cycling of silicon, Misra et al. showed that a crystalline phase $Li_{15}Si_4$ forms at high lithiation levels of silicon nanowires through in situ XRD measurements.[47] They used this information to modify the synthesis procedure to avoid the formation of this phase, as its known to be the cause of long-term cycling performance issues. However, XRD is limited to observing crystalline species with large long-range order, which restricts the versatility of this technique.

Microscopy in situ studies using techniques such as scanning electron microscopy (SEM) and transmission electron microscopy (TEM) have also been developed. These techniques require more complicated and advanced cell designs in order to perform in situ studies on batteries. In situ SEM studies are performed under vacuum, which makes it difficult to design a cell that is able to be cycled under these conditions. However, some studies utilizing ingenious cell designs have been successfully implemented.[48–50] For example, Sagane et al. conducted an in situ SEM study on the stripping and plating reactions on the surface of lithium metal anodes. They were able to distinguish different morphologies during in situ cycling.[51]

Nuclear magnetic resonance in situ studies have advantages over the above mentioned techniques as NMR is a non-invasive method, which does not require inert conditions and is able to resolve both crystalline and amorphous species. However, the cells need to be carefully designed to minimize undesired interferences with the magnetic field. Various effects such as the bulk magnetic susceptibility effect and radiofrequency shielding due to metallic components can influence the NMR signal. In addition, the cells are usually encased in plastic bags, which are permeable to the electrolyte solution and can cause issues in terms of long-term stability of these cells. A detailed description of the different designs, challenges and applications of in situ NMR methods for LIBs is given in Chapter 2.6.

## 1.5 Thesis Outline

This work aims to use various in situ NMR techniques and apply them to relevant issues in the battery community. In particular, the focus is on investigating LIBs under conditions as close to real-time as possible.

Chapter 2 provides an overview of the fundamentals of NMR and some selected techniques, which were used in this work including MAS NMR, pulsed-field gradient NMR and MRI and an introduction to in situ NMR on battery materials is given.

In Chapter 3 the difference between using silicon monoxide (a-SiO) and pure silicon as an anode material is being investigated.[52] Ex situ $^{29}$Si and in situ $^{7}$Li NMR is used to provide insight into the reaction mechanism of lithium alloying of a-SiO.

Chapter 4 introduces a novel in situ MAS NMR technique to monitor an electrochemical cell during cycling.[53] By designing an electrochemical cell with MAS capability both anode and cathode sides can be monitored concurrently (which in the past has not been possible). This innovative design essentially allows us to perform qualitative and quantitative study of a spinning metal-ion battery inside a magnet, which is substantially valuable in tracking the lithium distribution inside the cell as well as identifying reasons for capacity loss in real time. In Appendix A a pulsed-field gradient (PFG) NMR study of a quaternary polymer electrolyte is demonstrated. Diffusive properties at varying temperatures were analyzed in order to extract information about their feasibility in LIBs. In addition, this polymer electrolyte is of interest to advance the MAS NMR technique developed in Chapter 4.

Chapter 5 focusses on using a parallel-plate in situ NMR technique developed in our group to investigate lithium plating due to fast-charging in pure silicon-based electrodes.

Lastly, Chapter 6 gives a summary of the work and an outlook on possible future avenues for in situ NMR for battery materials.

# Bibliography

[1] Martin Winter, Brian Barnett, and Kang Xu. Before Li ion batteries. *Chemical reviews*, 118(23):11433–11456, 2018.

[2] IEA Global EV Outlook. Entering the Decade of Electric Drive, 2020.

[3] Arumugam Manthiram. A reflection on lithium-ion battery cathode chemistry. *Nature Communications*, 11(1):1–9, 2020.

[4] Yo Kobayashi, Hajime Miyashiro, Atsuko Yamazaki, and Yuichi Mita. Unexpected capacity fade and recovery mechanism of $LiFePO_4$/graphite cells for grid operation. *Journal of Power Sources*, 449:227502, 2020.

[5] Jakob Asenbauer, Tobias Eisenmann, Matthias Kuenzel, Arefeh Kazzazi, Zhen Chen, and Dominic Bresser. The success story of graphite as a lithium-ion anode material–fundamentals, remaining challenges, and recent developments including silicon (oxide) composites. *Sustainable Energy & Fuels*, 2020.

[6] Yayuan Liu, Yangying Zhu, and Yi Cui. Challenges and opportunities towards fast-charging battery materials. *Nature Energy*, 4(7):540–550, 2019.

[7] A. Ponrouch, J. Bitenc, R. Dominko, N. Lindahl, P. Johansson, and M.R. Palacin. Multivalent rechargeable batteries. *Energy Storage Materials*, 20: 253–262, 2019.

[8] Xin-Bing Cheng, Rui Zhang, Chen-Zi Zhao, and Qiang Zhang. Toward safe lithium metal anode in rechargeable batteries: a review. *Chemical reviews*, 117(15):10403–10473, 2017.

[9] Claus Daniel, Debasish Mohanty, Jianlin Li, and David L Wood. Cathode materials review. In *AIP Conference Proceedings*, volume 1597, pages 26–43. American Institute of Physics, 2014.

[10] Yemeserach Mekonnen, Aditya Sundararajan, and Arif I Sarwat. A review of cathode and anode materials for lithium-ion batteries. In *SoutheastCon 2016*, pages 1–6. IEEE, 2016.

[11] Zhangxian Chen, Weixin Zhang, and Zeheng Yang. A review on cathode materials for advanced lithium ion batteries: microstructure designs and performance regulations. *Nanotechnology*, 31(1):012001, 2019.

[12] Kinson C. Kam and Marca M. Doeff. Electrode materials for lithium ion batteries. *Material Matters*, 7:56–60, 2012.

[13] Seong Jin An, Jianlin Li, Claus Daniel, Debasish Mohanty, Shrikant Nagpure, and David L Wood III. The state of understanding of the lithium-ion-battery graphite solid electrolyte interphase (SEI) and its relationship to formation cycling. *Carbon*, 105:52–76, 2016.

[14] Martin Winter. The solid electrolyte interphase–the most important and the least understood solid electrolyte in rechargeable Li batteries. *Zeitschrift für physikalische Chemie*, 223(10-11):1395–1406, 2009.

[15] Tadhg Kennedy, Michael Brandon, Fathima Laffir, and Kevin M Ryan. Understanding the influence of electrolyte additives on the electrochemical performance and morphology evolution of silicon nanowire based lithium-ion battery anodes. *Journal of Power Sources*, 359:601–610, 2017.

[16] A Manuel Stephan and KS Nahm. Review on composite polymer electrolytes for lithium batteries. *Polymer*, 47(16):5952–5964, 2006.

[17] Penghui Yao, Haobin Yu, Zhiyu Ding, Yanchen Liu, Juan Lu, Marino Lavorgna, Junwei Wu, and Xingjun Liu. Review on polymer-based composite electrolytes for lithium batteries. *Frontiers in chemistry*, 7:522, 2019.

[18] Hilal Al-Salih, Allan Huang, Chae-Ho Yim, Annica I. Freytag, Gillian R. Goward, Elena Baranova, and Yaser Abu-Lebdeh. A polymer-rich quaternary composite solid electrolyte for lithium batteries. *Journal of The Electrochemical Society*, 167(7):070557, 2020.

[19] Simon Schweidler, Lea de Biasi, Alexander Schiele, Pascal Hartmann, Torsten Brezesinski, and Jürgen Janek. Volume changes of graphite anodes revisited: a combined operando X-ray diffraction and in situ pressure analysis study. *The Journal of Physical Chemistry C*, 122(16): 8829–8835, 2018.

[20] Rosamaria Fong, Ulrich Von Sacken, and Jeff R Dahn. Studies of lithium intercalation into carbons using nonaqueous electrochemical cells. *Journal of The Electrochemical Society*, 137(7):2009, 1990.

[21] Veronika Zinth, Christian von Lüders, Michael Hofmann, Johannes Hattendorff, Irmgard Buchberger, Simon Erhard, Joana Rebelo-Kornmeier, Andreas Jossen, and Ralph Gilles. Lithium plating in lithium-ion batteries at sub-ambient temperatures investigated by in situ neutron diffraction. *Journal of Power Sources*, 271:152–159, 2014.

[22] Mathias Petzl, Michael Kasper, and Michael A Danzer. Lithium plating in a commercial lithium-ion battery–A low-temperature aging study. *Journal of Power Sources*, 275:799–807, 2015.

[23] Thomas Waldmann and Margret Wohlfahrt-Mehrens. Effects of rest time after Li plating on safety behavior—ARC tests with commercial high-energy 18650 Li-ion cells. *Electrochimica Acta*, 230:454–460, 2017.

[24] JC Burns, DA Stevens, and JR Dahn. In-situ detection of lithium plating using high precision coulometry. *Journal of the Electrochemical Society*, 162(6):A959, 2015.

[25] Ilya A Shkrob, Marco-Tulio Fonseca Rodrigues, Dennis W Dees, and Daniel P Abraham. Fast Charging of Li-Ion Cells: Part II. Nonlinear Contributions to Cell and Electrode Polarization. *Journal of The Electrochemical Society*, 166(14):A3305, 2019.

[26] Thomas Waldmann, Björn-Ingo Hogg, and Margret Wohlfahrt-Mehrens. Li plating as unwanted side reaction in commercial Li-ion cells–A review. *Journal of Power Sources*, 384:107–124, 2018.

[27] Namhyung Kim, Sujong Chae, Jiyoung Ma, Minseong Ko, and Jaephil Cho. Fast-charging high-energy lithium-ion batteries via implantation of amorphous silicon nanolayer in edge-plane activated graphite anodes. *Nature communications*, 8(1):1–10, 2017.

[28] Alba Franco Gonzalez, Nai-Hsuan Yang, and Ru-Shi Liu. Silicon anode design for lithium-ion batteries: Progress and perspectives. *The Journal of Physical Chemistry C*, 121(50):27775–27787, 2017.

[29] Baris Key, Rangeet Bhattacharyya, Mathieu Morcrette, Vincent Seznec, Jean-Marie Tarascon, and Clare P Grey. Real-time NMR investigations of structural changes in silicon electrodes for lithium-ion batteries. *Journal of the American Chemical Society*, 131(26):9239–9249, 2009.

[30] Keitaro Kitada, Oliver Pecher, Pieter C. M. M. Magusin, Matthias F. Groh, Robert S. Weatherup, and Clare P. Grey. Unraveling the reaction mechanisms of SiO anodes for Li-ion batteries by combining in situ $^{7}$Li and ex situ $^{7}$Li/$^{29}$Si solid-state NMR spectroscopy. *Journal of the American Chemical Society*, 141(17):7014–7027, 2019.

[31] Matthew T McDowell, Seok Woo Lee, William D Nix, and Yi Cui. 25th Anniversary Article: Understanding the Lithiation of Silicon and Other Alloying Anodes for Lithium-Ion Batteries. *Advanced Materials*, 25(36): 4966–4985, 2013.

[32] N Dupré, P Moreau, E De Vito, L Quazuguel, M Boniface, A Bordes, C Rudisch, Pascale Bayle-Guillemaud, and D Guyomard. Multiprobe study of the solid electrolyte interphase on silicon-based electrodes in full-cell configuration. *Chemistry of Materials*, 28(8):2557–2572, 2016.

[33] Michael Holzapfel, Hilmi Buqa, Laurence J Hardwick, Matthias Hahn, Andreas Würsig, Werner Scheifele, Petr Novák, Rüdiger Kötz, Claudia Veit, and Frank-Martin Petrat. Nano silicon for lithium-ion batteries. *Electrochimica acta*, 52(3):973–978, 2006.

[34] Hong Li, Xuejie Huang, Liquan Chen, Zhengang Wu, and Yong Liang. A high capacity nano Si composite anode material for lithium rechargeable batteries. *Electrochemical and Solid State Letters*, 2(11):547, 1999.

[35] Candace K Chan, Hailin Peng, Gao Liu, Kevin McIlwrath, Xiao Feng Zhang, Robert A Huggins, and Yi Cui. High-performance lithium battery anodes using silicon nanowires. *Nature nanotechnology*, 3(1):31–35, 2008.

[36] NS Hochgatterer, MR Schweiger, S Koller, PR Raimann, T Wöhrle, C Wurm, and Martin Winter. Silicon/graphite composite electrodes for high-capacity anodes: influence of binder chemistry on cycling stability. *Electrochemical and Solid-State Letters*, 11(5):A76–A80, 2008.

[37] Jing Li, L Christensen, MN Obrovac, KC Hewitt, and JR Dahn. Effect of heat treatment on Si electrodes using polyvinylidene fluoride binder. *Journal of the electrochemical Society*, 155(3):A234, 2008.

[38] Yanting Jin, Nis-Julian H Kneusels, Lauren E Marbella, Elizabeth Castillo-Martínez, Pieter CMM Magusin, Robert S Weatherup, Erlendur Jónsson, Tao Liu, Subhradip Paul, and Clare P Grey. Understanding fluoroethylene carbonate and vinylene carbonate based electrolytes for Si anodes in lithium ion batteries with NMR spectroscopy. *Journal of the American Chemical Society*, 140(31):9854–9867, 2018.

[39] Bo Liang, Yanping Liu, and Yunhua Xu. Silicon-based materials as high capacity anodes for next generation lithium ion batteries. *Journal of Power sources*, 267:469–490, 2014.

[40] Xiuxia Zuo, Jin Zhu, Peter Müller-Buschbaum, and Ya-Jun Cheng. Silicon based lithium-ion battery anodes: A chronicle perspective review. *Nano Energy*, 31:113–143, 2017.

[41] MN Obrovac and LJ Krause. Reversible cycling of crystalline silicon powder. *Journal of the Electrochemical Society*, 154(2):A103, 2006.

[42] Jae-Hun Kim, Hun-Joon Sohn, Hansu Kim, Goojin Jeong, and Wanuk Choi. Enhanced cycle performance of SiO-C composite anode for lithium-ion batteries. *Journal of power sources*, 170(2):456–459, 2007.

[43] PPRML Harks, FM Mulder, and PHL Notten. In situ methods for Li-ion battery research: A review of recent developments. *Journal of power sources*, 288:92–105, 2015.

[44] Chih-Wei Hu, Tsan-Yao Chen, Kai-Sheng Shih, Pin-Jiun Wu, Hui-Chia Su, Ching-Yu Chiang, An-Feng Huang, Han-Wei Hsieh, Chia-Chin Chang, Bor-Yuan Shew, et al. Real-time investigation on the influences of vanadium additives to the structural and chemical state evolutions of $LiFePO_4$ for enhancing the electrochemical performance of lithium-ion battery. *Journal of Power Sources*, 270:449–456, 2014.

[45] Debasish Mohanty, Sergiy Kalnaus, Roberta A Meisner, Kevin J Rhodes, Jianlin Li, E Andrew Payzant, David L Wood III, and Claus Daniel. Structural transformation of a lithium-rich $Li_{1.\ 2}Co_{0.\ 1}Mn_{0.\ 55}Ni_{0.\ 15}O_2$ cathode during high voltage cycling resolved by in situ X-ray diffraction. *Journal of Power Sources*, 229:239–248, 2013.

[46] Masaaki Hirayama, Hedekazu Ido, KyungSu Kim, Woosuk Cho, Kazuhisa Tamura, Jun'ichiro Mizuki, and Ryoji Kanno. Dynamic structural changes at $LiMn_2O_4$/electrolyte interface during lithium battery reaction. *Journal of the American Chemical Society*, 132(43):15268–15276, 2010.

[47] Sumohan Misra, Nian Liu, Johanna Nelson, Seung Sae Hong, Yi Cui, and Michael F Toney. In situ X-ray diffraction studies of (de) lithiation mechanism in silicon nanowire anodes. *Acs Nano*, 6(6):5465–5473, 2012.

[48] Steven T Boles, Andreas Sedlmayr, Oliver Kraft, and Reiner Mönig. In situ cycling and mechanical testing of silicon nanowire anodes for lithium-ion battery applications. *Applied Physics Letters*, 100(24):243901, 2012.

[49] Dean J Miller, Christian Proff, JG Wen, Daniel P Abraham, and Javier Bareno. Observation of microstructural evolution in Li battery cathode oxide particles by in situ electron microscopy. *Advanced Energy Materials*, 3(8):1098–1103, 2013.

[50] Di Chen, Sylvio Indris, Michael Schulz, Benedikt Gamer, and Reiner Mönig. In situ scanning electron microscopy on lithium-ion battery electrodes using an ionic liquid. *Journal of Power Sources*, 196(15):6382–6387, 2011.

[51] Fumihiro Sagane, Ryosuke Shimokawa, Hikaru Sano, Hikari Sakaebe, and Yasutoshi Iriyama. In-situ scanning electron microscopy observations of Li plating and stripping reactions at the lithium phosphorus oxynitride glass electrolyte/Cu interface. *Journal of Power Sources*, 225:245–250, 2013.

[52] Annica I. Freytag, Allen D. Pauric, Meng Jiang, and Gillian R. Goward. $^{7}$Li and $^{29}$Si NMR Enabled by High-Density Cellulose-Based Electrodes in the Lithiation Process in Silicon and Silicon Monoxide Anodes. *The Journal of Physical Chemistry C*, 123(18):11362–11368, 2019.

[53] Annica I Freytag, Allen D Pauric, Sergey A Krachkovskiy, and Gillian R Goward. In Situ Magic-Angle Spinning $^{7}$Li NMR Analysis of a Full Electrochemical Lithium-Ion Battery Using a Jelly Roll Cell Design. *Journal of the American Chemical Society*, 141(35):13758–13761, 2019.

## Chapter 2

# Nuclear Magnetic Resonance

This body of work deals with the application and development of in situ NMR methods for battery materials. In the following an overview of the necessary principles needed to realize the experiments performed in later chapters is given. Before diving into the more complex NMR methods, an introduction to the fundamentals of NMR is provided.

## 2.1 Nuclear Spin and the Zeeman Effect

NMR is a spectroscopic technique which is based on the interaction of the magnetic moment of a nucleus with a magnetic field. In a classical sense, the nucleus can be described as a small charged particle spinning around its axis. Because the spinning particle is charged, it creates an electric current making it behave like a small electromagnet. When put into an external magnetic field, the net magnetic moment aligns with the field. However, the *spin* is not actually due to the particle rotation but is rather an intrinsic physical property of the atomic nucleus itself and can only purely be described by quantum mechanics (although the classical model helps in grasping the idea of spin). The spin, or spin quantum number $I$, is related to the spin angular momentum $\hat{\boldsymbol{S}}$ as[1]

$$\hat{\boldsymbol{S}} = \hbar \cdot \sqrt{I(I+1)} \tag{2.1}$$

with $\hbar$ being the reduced Planck constant. The net spin quantum number of protons and neutrons is 1/2. Therefore, when an atom is comprised of an odd number of either or both protons and neutrons, the spin quantum number $I$ is non-zero making it observable by NMR. For instance, two isotopes of carbon ($^{12}$C and $^{13}$C) have different spin quantum numbers: $^{12}$C has a net spin of zero (consisting of 6 protons and 6 neutrons) and $^{13}$C a net spin of 1/2 (consisting of 6 protons and 7 neutrons). As a result, out of the two only $^{13}$C is a so-called NMR-active nucleus.

The spin angular momentum $\hat{\boldsymbol{S}}$ is related to the magnetic moment $\hat{\boldsymbol{\mu}}$ by a proportionality constant known as the gyromagnetic ratio $\gamma$.

$$\hat{\boldsymbol{\mu}} = \gamma \cdot \hat{\boldsymbol{S}} \tag{2.2}$$

The gyromagnetic ratio $\gamma$ is an important parameter in NMR and gives information about the sensitivity of the magnetic moment to an external magnetic field with higher gyromagnetic ratios giving a greater sensitivity. In the case of a spin 1/2 nucleus, the magnetic moment splits into two energy levels inside an external magnetic field also known as the Zeeman splitting. The energy levels $E_m$ are described as

$$\begin{aligned} E_m &= -\hat{\mu}_z \vec{B}_0 \\ &= -m\hbar\gamma\vec{B}_0 \end{aligned} \tag{2.3}$$

where $m$ is the magnetic quantum number (which takes on values of $+I$ and

$-I$) and $\vec{B}_0$ is the magnetic field strength of the applied field aligned along the z-axis. For a spin 1/2 nucleus the magnetic quantum numbers are $m = \pm\frac{1}{2}$ and the energy levels are commonly expressed in terms of $\alpha$ and $\beta$ for $m = +\frac{1}{2}$ and $m = -\frac{1}{2}$, respectively. The separation of the energy levels $\Delta E$ is then given as

$$\begin{aligned}\Delta E &= E_\beta - E_\alpha \\ &= \frac{1}{2}\hbar\gamma\vec{B}_0 - \left(-\frac{1}{2}\hbar\gamma\vec{B}_0\right) \\ &= \hbar\gamma\vec{B}_0\end{aligned} \tag{2.4}$$

$\Delta E$ is regularly expressed in frequency units, known as the Larmor frequency $\omega_0$ (in $\mathrm{rad\,s^{-1}}$) and is obtained by dividing $\Delta E$ by $\hbar$.

$$\omega_0 = \gamma\vec{B}_0 \tag{2.5}$$

Figure 2.1 shows a visual representation of the Zeeman splitting of two spin-1/2 nuclei with different values for $\gamma$. It is evident, that the energy level separation is largely dependent on both the gyromagnetic ratio $\gamma$ and the applied field $\vec{B}_0$. As mentioned above, nuclei with a greater gyromagnetic ratio show a larger $\Delta E$ and are therefore more sensitive to the nuclear magnetic resonance response. Similarly, it is beneficial to work at higher fields of $\vec{B}_0$ in order to maximize the energy level separation. It is important to mention here that the splitting of the energy levels is small in NMR (compared to other spectroscopic methods) and can be described by the Boltzmann distribution.

$$\frac{N_\beta}{N_\alpha} = e^{-\Delta E/k_B T} \tag{2.6}$$

Here, $N_\alpha$ and $N_\beta$ are the spin state populations for spin $\alpha$ and $\beta$, $k_B$ is the

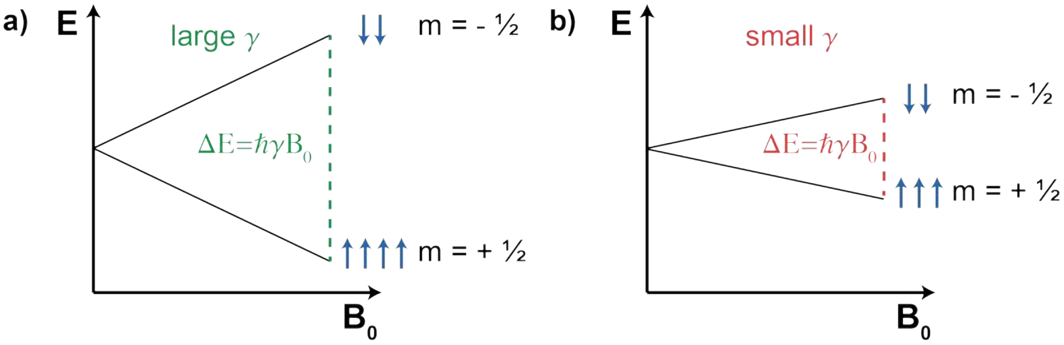

Figure 2.1: Schematic of the Zeeman splitting for a spin-1/2 nucleus with (a) a large gyromagnetic ratio (e.g., $^1$H) and (b) a small gyromagnetic ratio (e.g., $^{29}$Si).

Boltzmann constant and T the temperature. As a result of the small $\Delta E$, the difference in spins in the excited state versus the ground state is minimal, rendering NMR an insensitive spectroscopic technique. However, because NMR is occuring in the low-frequency range, it also makes it a non-invasive method, which is beneficial for the study of a variety of solution- and solid-state materials.

Up to this point, the theory of spin and the interaction of the magnetic moment of a nucleus with a magnetic field has been established. However, in order to exploit the resonance effect of a nuclear spin ensemble, the system has to be disrupted by a second magnetic field. This can be achieved by applying a strong radio-frequency (RF) pulse at the Larmor frequency of the nucleus of interest. In the following, the vector model of a spin-1/2 nucleus will be discussed.

## 2.2 The Vector Model

The vector model is a convenient way of understanding the fundamental principles of an NMR experiment. It allows one to visualize the steps required to obtain an NMR signal without diving into the more complex quantum mechanical approach. Consider an NMR-active sample containing uncoupled spin-1/2 nuclei. Without an applied magnetic field the net magnetization of the nuclear spins is randomized and averages out to zero as shown in Figure 2.2a. Once exposed to a magnetic field (typically on the order of 4 T to 20 T), the net spin magnetization builds up until it reaches equilibrium. This build-up of magnetization does not occur instantaneously and is highly dependent on the sample. The time it takes for the magnetization to reach equilibrium is defined by the so-called spin-lattice relaxation time constant $T_1$ and can be on the order of milliseconds to seconds (with some exceptions). At equilibrium (Figure 2.2b), the net magnetization is aligned with the applied magnetic field $\vec{B}_0$ (defined along the z-axis) and, importantly, does not have any contributions from the magnetization in the transverse plane (x-y plane). In order to generate an NMR signal, the magnetization vector has to be disturbed from its equilibrium state. This is achieved by applying a strong oscillating RF pulse at the Larmor frequency $\omega_0$ in the transverse plane (e.g., along the x-axis), commonly known as the $\vec{B}_1$ field, which is related to the RF nutation frequency $\omega_1$ as

$$\omega_1 = |\gamma|\vec{B}_1 \tag{2.7}$$

where the absolute value of $\gamma$ is used in order for $\omega_1$ to always be positive. As a result of the RF pulse, the magnetization vector precesses around the $\vec{B}_0$ field at a flip angle $\beta$ (Figure 2.2c). The RF pulse has a set duration $t_p$ and is

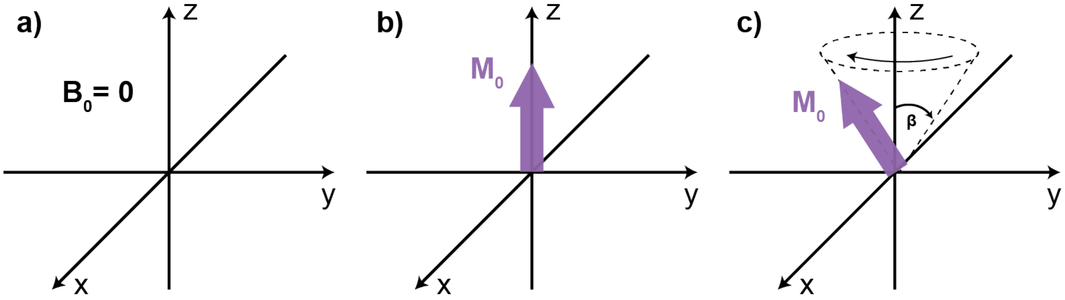

Figure 2.2: Visualization of the build-up of magnetization in a magnetic field. In (a) no field is applied and the net magnetization vector is zero, (b) a field $\vec{B}_0$ is applied along the z-axis and the magnetization $M_0$ is aligned with the field after time $T_1$, (c) an RF pulse is applied, which moves $M_0$ away from equilibrium allowing it to precess around the z-axis at the Larmor frequency at a flip angle $\beta$.

related to the flip angle as[2]

$$\beta = \omega_1 t_p \tag{2.8}$$

By manipulating the duration or strength of the RF pulse, different flip angles can be achieved. Consider an RF pulse applied along the x-axis with a flip angle of 90°. The magnetization vector $M_0$ is rotated onto the -y-axis following the right-hand rule. When the pulse is turned off, the magnetization vector $M_0$ starts to precess around the $\vec{B}_0$ field. The precession in the transverse plane decays over time and is described as

$$\begin{aligned} M_x &= M_{eq} \sin(\omega_0 t)\, e^{\frac{-t}{T_2}} \\ M_y &= -M_{eq} \cos(\omega_0 t)\, e^{\frac{-t}{T_2}} \end{aligned} \tag{2.9}$$

where the oscillating magnetization vector can be broken up into its x- and y-components $M_x$ and $M_y$, respectively. $M_{eq}$ is the magnetization at equilibrium along the z-axis. The constant $T_2$ is known as the spin-spin relaxation and greatly affects the time it takes for the system to lose coherence. The resulting decay in magnetization, or free induction decay (FID), can be detected by placing a wire coil in the x-y plane as the oscillation magnetization vector induces a current in the coil. The FID is then processed by a Fourier transform function to produce a spectrum in the frequency domain.

Up to this point the spins have been treated as one ensemble resonating at the same Larmor frequency. However, in reality, many interactions between the nuclei in the sample and its surroundings can have major effects on the line shape, position, intensity and number of peaks in an NMR spectrum. This complicates things but is also the foundation of why NMR is known to be a powerful and versatile technique in various scientific fields.

## 2.3 Nuclear Spin Interactions

So far, the description of the nuclear spin energy ($E_{NMR}$) included only external interactions, namely the Zeeman energy $E_z$ and the interaction with the RF field $E_{RF}$. In addition, internal interactions are present, which can influence the NMR spectrum immensely. They can be summarized as[3]

$$E_{NMR} = \underbrace{E_Z + E_{RF}}_{\text{external}} + \underbrace{E_S + E_J + E_D + E_Q + E_P + E_K}_{\text{internal}} \tag{2.10}$$

with $E_S$, $E_J$, and $E_D$ as the shielding, spin-spin (or J) coupling and dipolar coupling energy, respectively. In addition, quadrupolar ($E_Q$), paramagnetic ($E_P$) and Knight shift ($E_K$) contributions can be present for certain samples. In the following, these interactions are defined in more detail.

### 2.3.1 Shielding

The concept of shielding is one of the most prominent characteristics in NMR and is commonly known as the chemical shift interaction. The electrons surrounding the nucleus produce a small induced field which can alter (or shift) the resonance frequency of the nucleus inside the magnetic field. The chemical shift is dependent on the orientation of the molecule with regard to the applied magnetic field because the distribution of electrons around the nucleus is non-spherical. This directional dependence is commonly described by the term *anisotropy.* In solution, this interaction is averaged out to its isotropic component due to molecular tumbling. However, in solids the molecular structure is far more rigid resulting in a distribution of chemical shifts in the NMR spectrum of polycrystalline samples.

The contribution from the electrons affect the strength of the local $\vec{B}_0$ field resulting in an effective field $\vec{B}_{\text{eff}}$ that is dependent on the nuclear shielding tensor $\boldsymbol{\sigma}$

$$\vec{B}_{\text{eff}} = \vec{B}_0(\mathbf{1} - \boldsymbol{\sigma}) \tag{2.11}$$

The shielding tensor is commonly fixed in a principal axis system (PAS) in reference to the molecule, where XX, YY and ZZ are the principal values of the shielding tensor.

$$\boldsymbol{\sigma}^{PAS} = \begin{pmatrix} \sigma_{XX} & 0 & 0 \\ 0 & \sigma_{YY} & 0 \\ 0 & 0 & \sigma_{ZZ} \end{pmatrix} \tag{2.12}$$

The parameters, which describe the chemical shift using the Haeberlen convention are commonly written as

$$\begin{aligned}
\sigma_{iso} &= \frac{1}{3}\left(\sigma_{XX} + \sigma_{YY} + \sigma_{ZZ}\right) \\
\Delta &= \sigma_{ZZ} - \sigma_{iso} \\
\eta &= \frac{(\sigma_{XX} - \sigma_{YY})}{\sigma_{ZZ}}
\end{aligned} \tag{2.13}$$

where $\sigma_{iso}$, $\Delta$ and $\eta$ are the isotropic value, the anisotropy and asymmetry, respectively. As a result of shielding, the Larmor frequency is dependent on the orientation of the nuclei in the field and its symmetry. The Larmor frequency with shielding contributions $\omega_S$ is

$$\omega_S(\theta, \phi) = -\omega_0\sigma_{iso} - \frac{1}{2}\omega_0\Delta\left(3\cos^2\theta - 1 + \eta\sin^2\theta\cos 2\phi\right) \tag{2.14}$$

where the angles $\theta$ and $\phi$ relate the orientation of the molecule to the applied $\vec{B}_0$ field along the z-axis. This directional dependence manifests itself in a rather complicated NMR spectrum for solids with powder-pattern type distributions as illustrated in Figure 2.3. In order to increase the resolution in solid-state NMR (ssNMR), this orientation-dependence can be exploited using a technique called magic-angle spinning, which will be discussed in Section 2.4.

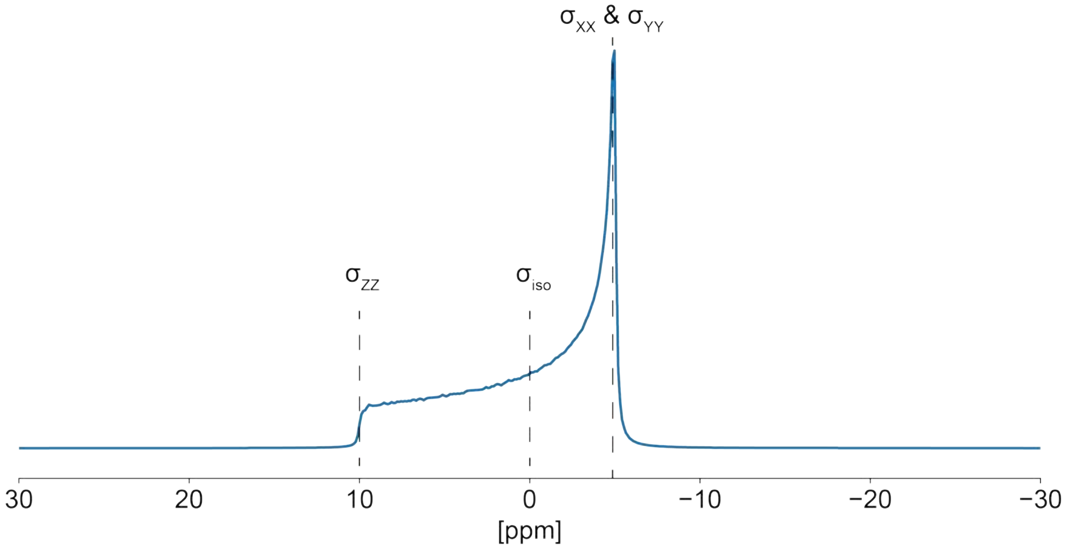

Figure 2.3: Simulated NMR spectrum illustrating a typical powder pattern distribution due to CSA.

### 2.3.2 Spin-spin Coupling

Spin-spin coupling, or more commonly known as J-coupling, refers to the interaction of the electrons surrounding the nuclear spins with each other. This interaction is of great importance in solution-state NMR and can give a vast amount of information about the bonding environment inside the molecule. However, it is a relatively weak interaction (in the $10^1$ Hz range) compared to the other interactions which affect the NMR spectrum. Because the interaction is small relative to other interactions for the experiments described in this thesis, J-coupling will not be discussed further.

### 2.3.3 Dipolar Coupling

Dipolar coupling is the interaction between the nuclear spins through space. Nuclear spins exhibit a magnetic moment and can *feel* each other if in close proximity. In a classical sense, the interaction energy $U$ between two magnetic dipole moments $\vec{\mu}_1$ and $\vec{\mu}_2$ and $\vec{r}$ the vector between the two dipoles separated by a distance $r$ can be expressed as[4]

$$U = \left( \frac{\vec{\mu}_1 \vec{\mu}_2}{r^3} - 3 \frac{(\vec{\mu}_1 \vec{r})\,(\vec{\mu}_2 \vec{r})}{r^5} \right) \frac{\mu_0}{4\pi} \tag{2.15}$$

where $\mu_0$ is the vacuum permeability constant.

Recall from Equation 2.2 the relation between the magnetic moment $\hat{\boldsymbol{\mu}}$ and the spin angular momentum $\hat{\boldsymbol{S}}$. The interaction Hamiltonian $\hat{H}_D$ for two spins, $\boldsymbol{I}$ and $\boldsymbol{S}$, can then be written as

$$\hat{H}_D = -\frac{\mu_0}{4\pi} \gamma_I \gamma_S \hbar \left( \frac{\boldsymbol{I} \cdot \boldsymbol{S}}{r^3} - 3 \frac{(\boldsymbol{I} \cdot \vec{r})\,(\boldsymbol{S} \cdot \vec{r})}{r^5} \right) \tag{2.16}$$

with $\gamma_I$ and $\gamma_S$ as the gyromagnetic constants for spin $\boldsymbol{I}$ and $\boldsymbol{S}$, respectively. The Hamiltonian is regularly expressed in spherical polar coordinates $\theta$ and $\phi$ (definition shown in Figure 2.4), which results in the following expression

$$\hat{H}_D = -\left( \frac{\mu_0}{4\pi} \right) \frac{\gamma_I \gamma_S \hbar}{r^3} \left[ A + B + C + D + E + F \right] \tag{2.17}$$

with

$$\begin{aligned}
A &= \hat{I}_z \hat{S}_z \left( 3\cos^2\theta - 1 \right) \\
B &= -\frac{1}{4} \left[ \hat{I}_+ \hat{S}_- + \hat{I}_- \hat{S}_+ \right] \left( 3\cos^2\theta - 1 \right) \\
C &= -\frac{3}{2} \left[ \hat{I}_z \hat{S}_+ + \hat{I}_+ \hat{S}_z \right] \sin\theta \cos\theta e^{-i\phi} \\
D &= -\frac{3}{2} \left[ \hat{I}_z \hat{S}_- + \hat{I}_- \hat{S}_z \right] \sin\theta \cos\theta e^{+i\phi} \\
E &= -\frac{3}{4} \left[ \hat{I}_+ \hat{S}_+ \right] \sin^2\theta e^{-2i\phi} \\
F &= -\frac{3}{4} \left[ \hat{I}_- \hat{S}_- \right] \sin^2\theta e^{+2i\phi}
\end{aligned} \tag{2.18}$$

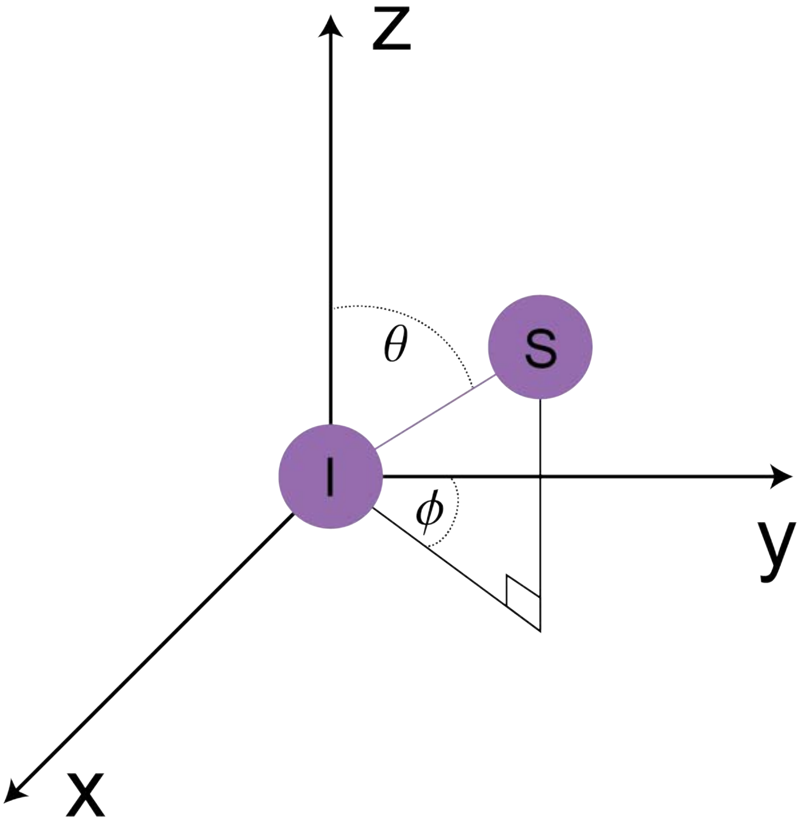

Figure 2.4: Definition of the polar angles for an I-S spin system. The magnetic field $\vec{B}_0$ is applied along the z-axis.[4]

where $\hat{I}_+$, $\hat{I}_-$, $\hat{S}_+$ and $\hat{S}_-$ are the raising (+) and lowering (-) operator for spin I and S. $\hat{I}_z$, $\hat{S}_z$ are nuclear spin angular momentum operators for spin I and S along the z-axis, respectively. This rather complex description of the dipole-dipole interaction reduces to terms A and B as terms C to F do not commute with the Zeeman Hamiltonian. As a result of dipolar coupling, lineshapes are broadened in the NMR spectrum. The degree of broadening highly depends on the gyromagnetic ratios of the observed nuclei and their relative number and distances. Again, similarly to the shielding interaction, this effect is orientation-dependent and MAS can be applied to increase the resolution of the spectrum.

### 2.3.4 Quadrupolar Interaction

Up to this point, only spin-1/2 nuclei were discussed. However, a large portion of the periodic table includes nuclei with spins greater than 1/2. Such spins have additional interactions that contribute to the NMR spectrum. This is known as the quadrupolar interaction and arises from the fact that the spins have an electric quadrupole moment which interacts with the electric field gradients (EFG) at the nucleus. The most important parameters which describe the quadrupolar interaction are the quadrupolar coupling constant $C_Q$ and the asymmetry parameter $\eta_Q$[4]

$$\begin{aligned} C_Q &= \frac{e^2 Q V_{ZZ}}{h} \\ \eta_Q &= \frac{V_{YY} - V_{XX}}{V_{ZZ}} \end{aligned} \tag{2.19}$$

where $V_{XX}$, $V_{YY}$ and $V_{ZZ}$ are the tensor elements of the EFG and $e$ and $Q$ are the charge of the electron and the electric quadrupolar moment, respectively. Similarly to the shielding interaction, the quadrupolar interaction has an orientation-dependence. The first-order quadrupolar Hamiltonian $\hat{H}_Q$ is written as[4]

$$\hat{H}_Q = \frac{3C_Q}{8I\left(2I-1\right)} \left(3\cos^2\theta - 1 + \frac{1}{2}\eta_Q \sin^2\theta \cos 2\phi\right)\left(3\hat{I}_z^2 - \hat{I}^2\right) \tag{2.20}$$

where $\theta$ and $\phi$ are the angles defining the orientation of the EFG tensor to the applied field $\vec{B}_0$. In this work, $^7$Li NMR is used for various studies ranging from in situ and ex situ MAS to PFG NMR. $^7$Li has a moderate quadrupolar interaction, which manifests itself mostly in line broadening.[5] A detailed description on quadrupolar NMR is therefore omitted here.

### 2.3.5 Paramagnetic Interaction

Materials containing a paramagnetic center show an additional interaction in the NMR spectrum. This is due to the existence of unpaired electrons which couple with nuclear spins, known as hyperfine coupling. A detailed description of the NMR theory of paramagnetic materials is beyond the scope of this thesis. However, a few characteristics of paramagnetic NMR are worth mentioning.

The hyperfine interaction in paramagnetic materials has quite a significant effect on the NMR spectrum and is much larger in magnitude than other interactions introduced previously due to the fact that the electron spin gyromagnetic ratio is around $10^3$ times larger than nuclear magnetic ratios. The effect of these interactions result in broad lineshapes, a large shift range and fast relaxation behaviour. A vast amount of battery cathode materials have paramagnetic centers, which influence the NMR spectrum significantly. Under static conditions these lineshapes tend to disappear in the baseline due to large broadening. MAS is basically inevitable to resolve paramagnetic species. This creates issues when trying to observe cathode materials through in situ NMR, which will be picked up in Chapter 4, where a new technique that allows for the monitoring of an LCO/graphite full cell will be introduced, which lays the foundation for MAS in situ NMR of cathode materials.

### 2.3.6 Knight Shift

The Knight shift arises from the interaction of conduction electrons in metals with the nuclear spins.[6] One common example in in situ NMR of lithium-ion battery materials is the $^7$Li Knight shift of lithium metal. Lithium metal is commonly used as a counter electrode and is therefore prominent in most in situ spectra. It is conveniently shifted to 260 ppm to 270 ppm (far away from the diamagnetic region), which makes it easy to distinguish from other species in the spectrum.

In addition, Knight shift contributions are typically found in metallic-type materials such as Li-Sn or Li-Si alloys.[7,8] The polarized electron spins in these materials can induce an additional electric field at the nuclear site if an Li s orbital contributes to the density of states (DOS) at the Fermi level, leading to a Knight shift of the NMR signal as[7,9]

$$K = \frac{8\pi}{3} \left\langle \left| \Psi_{r=0} \right|^2 \right\rangle \chi_s^e \tag{2.21}$$

where $\langle |\Psi_{r=0}|^2 \rangle$ is the density of conduction electrons at the Li nucleus averaged over the Fermi surface and $\chi_s^e$ is the Pauli susceptibility. The Knight shift for lithium stannides has been investigated through $^7$Li MAS NMR revealing an almost linear trend between the Knight shift and the contribution of the DOS of the lithium s orbital as shown in Figure 2.5.[7] Although, the shift is not as pronounced in Li-Sn systems compared to lithium metal, important information about the metallic character of the materials can be deduced. In Chapter 3 Li-Si phases are characterized through $^7$Li and $^{29}$Si MAS NMR, which show a similar response to the Li-Sn phases.

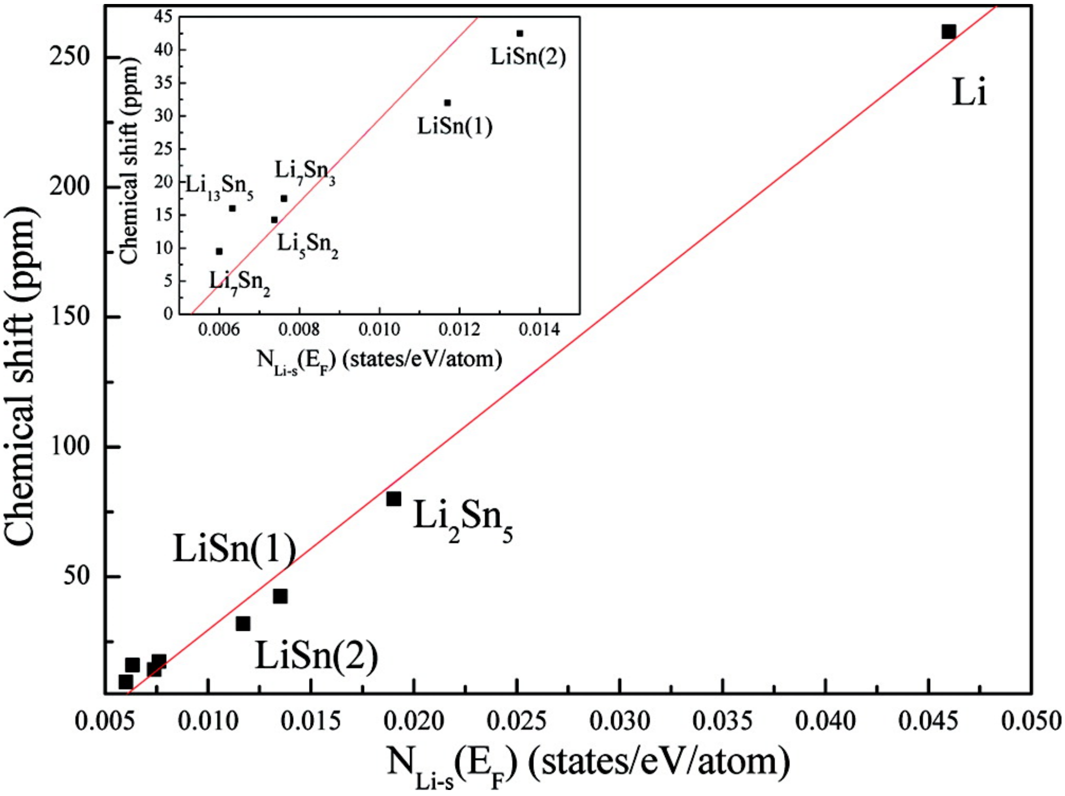

Figure 2.5: Experimental values of the $^7$Li NMR shift of Li-Sn phases as a function of the computed value of the density of Li s states at the Fermi level. Reprinted with permission from The Journal of Physical Chemistry C, 2010, 114, 14, 6749-6754[7]. Copyright © 2010, American Chemical Society.

## 2.4 Magic-Angle Spinning

The interactions introduced in the previous section are dependent on the orientation of the sample with respect to the field. This dependence can be exploited to increase the resolution of an NMR spectrum using a technique called magic-angle spinning (MAS) NMR. Specialized probes have been developed for ssNMR which allow for rapid spinning of a sample inside a ceramic rotor at a specific angle with respect to the magnetic field known as the magic angle $\theta_R$. When the angle $\theta_R$ is set to 54.74°, the term $(3\cos^2\theta - 1)$ (in Equations 2.14, 2.18 and 2.20) averages to zero under MAS. The spinning is achieved by

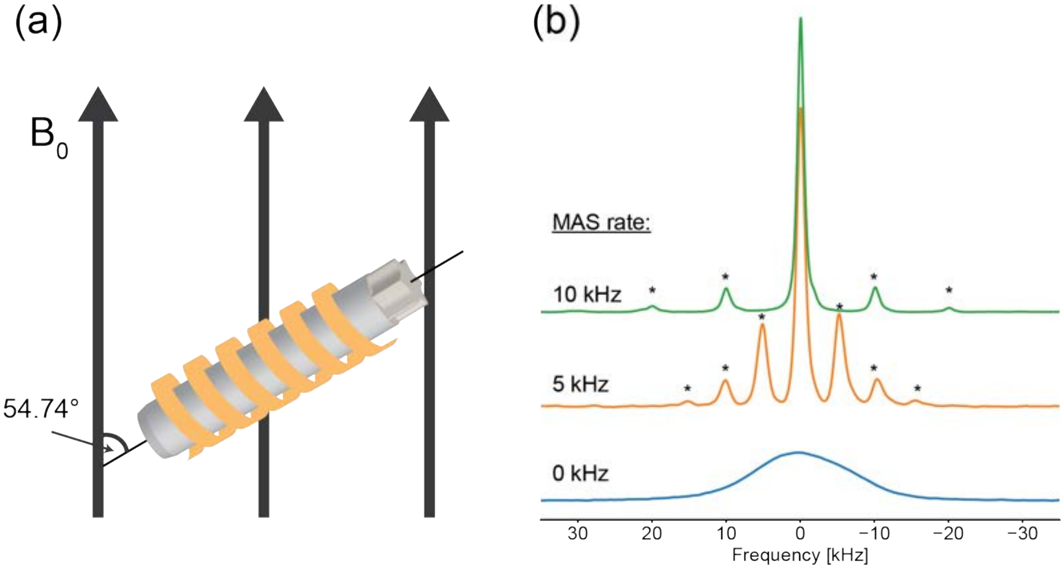

Figure 2.6: (a) Schematic of an MAS rotor aligned at the magic angle (54.74°) with respect to the $B_0$ field. A solenoid coil (in yellow) surrounds the rotor. (b) $^7$Li NMR spectra of $LiCoO_2$ under static conditions (blue), under 5 kHz MAS (orange) and under 10 kHz MAS (green) using a 4 mm MAS rotor. Asterisks denote spinning sidebands. Spectra collected at 117 MHz, 256 scans, recycle delay 2 seconds, 4 μs, π/2 pulse using a pulse-acquire sequence.

applying so-called bearing and drive gas to the rotor. The bearing gas allows the rotor to "float" inside the sample stator similar to the floating of a puck in air hockey. The drive gas is then applied to the fins on the rotor cap, allowing the rotor to spin. The rotors for MAS can be categorized into different sizes depending on their diameter. Smaller rotors can reach higher spinning speeds, e.g. a 4 mm rotor can reach up to 15 kHz spinning speed whereas a 0.6 mm rotor goes up to 126 kHz.[10] Figure 2.6a shows a schematic of an MAS rotor inside a $\vec{B}_0$ field aligned at the magic-angle.

In order to achieve a substantial increase in resolution, the spinning rate has to be faster than the magnitude of the inherent interaction of the sample of interest. In ssNMR, the most important interactions which have an effect on the resolution of the spectrum include but are not limited to dipolar coupling and quadrupolar or paramagnetic interactions. These range from anywhere between a few kHz up to MHz values. A typical response under MAS conditions is shown in Figure 2.6b, which shows spectra of $LiCoO_2$ with varying spinning speeds. The so-called spinning sidebands occur to the left and right of the isotropic peak separated by the spinning frequency. It is desired to apply high spinning speeds to avoid overlap of spinning sidebands in the spectrum when more than one chemical shift environment is present in the sample and to concentrate signal in fewer spinning sidebands. However, for samples where the interactions are much larger than the maximum achievable spinning speeds, e.g. for most paramagnetic materials, it is impossible to obtain spectra free of spinning sidebands using regular NMR pulse sequences. Some clever techniques exist, that allow for the separation of the isotropic and anisotropic contributions resulting in an uncluttered spectrum, which will be briefly discussed in the following.

### 2.4.1 MATPASS

Magic-angle turning and phase-adjusted spinning sideband separation (MATPASS) is a technique used in NMR to separate the isotropic and anisotropic contributions in a spectrum.[11] This technique has been used for materials with large paramagnetic effects, as it allows to separate the spinning sidebands from the isotropic peaks in an NMR spectrum.[12] In chapter 4 this technique is used for the MAS NMR analysis of a spinning electrochemical cell.[13] The maximum spinning speed for the experiments was limited by the type of the experiment and size of the MAS rotor (10 kHz), which required the use of MATPASS to remove residual overlapping spinning sidebands from the NMR spectrum due to the low spinning speeds.[14]

The MATPASS experiment is a combination of two types of experiments, namely magic-angle turning (MAT) and phase-adjusted spinning sideband separation (PASS).[14] The MAT experiment is similar to the magic-angle hopping (MAH) experiment, which exploits the orientation-dependence of the anisotropic contribution by rotating the sample at the magic-angle in steps of 120° allowing for the separation of the isotropic contribution from the anisotropic one.[15] The same principles apply to MAT experiments with the only difference being that MAT is performed under slow spinning speeds as opposed to discrete hopping in MAH.[16] MAH is more intuitive to understand, due to the physical step-wise rotation of the rotor, which is why it will be discussed briefly.

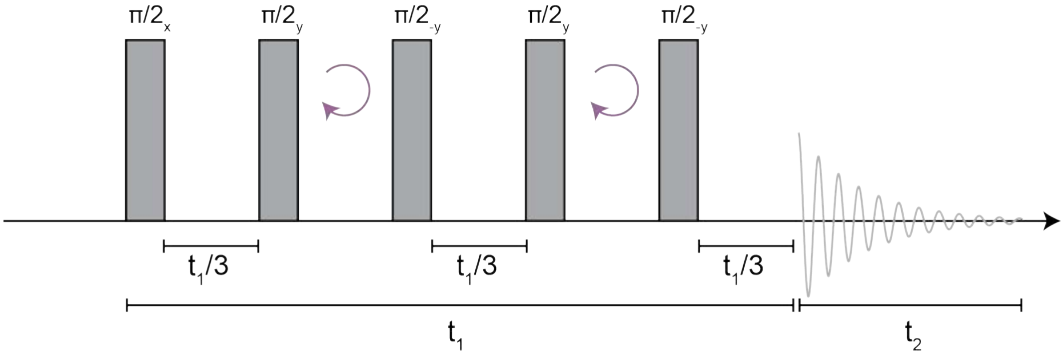

Figure 2.7: Magic-angle hopping NMR pulse sequence, where $t_1$ and $t_2$ denote the timings for the indirect and direct dimension, respectively. Purple arrows indicate rotation by 120° around the magic-angle.[15]

MAH is a two-dimensional experiment, where the so-called direct dimension is governed by $t_2$ and the indirect dimension by $t_1$.[15] Figure 2.7 shows the pulse sequence for an MAH experiment. It consists of five $\pi/2$ pulses. The initial pulse moves the magnetization into the x-y plane, where it precesses for $t_1/3$. The second pulse moves the magnetization back onto the z-axis, which

| Experiment no. | $\phi_1$ | $\phi_2$ | $\phi_3$ | $\phi_4$ | $\phi_5$ | Acquisition |
|---|---|---|---|---|---|---|
| 1 | x | y | -y | y | -y | + |
| 2 | x | -x | -y | y | x | + |
| 3 | x | y | -y | x | x | - |
| 4 | x | -x | -y | -x | -y | - |

Table 2.1: Phases of the pulses in Figure 2.7 and the receiver for an MAH experiment.[15]

is also known as z-storage and is particularly useful for samples with short $T_2$ relaxation as it decrease signal loss by storing the magnetization on the z-axis. After the second pulse, the sample is rotated by 120° and the same procedure as for pulse one and two is repeated. A second rotation occurs after the fourth pulse, leading to a total of three different orientations. In order to remove the anisotropic contribution from the indirect dimension the experiment has to be repeated with a minimum of four different $t_1$ increments, which results in purely isotropic contributions in the indirect dimension and both isotropic and anisotropic contributions in the direct dimension. The phases for the 4-step phase cycle are summarized in Table 2.1.

The MAH (and MAT) experiment can be performed using $\pi$ or $\pi/2$ pulses, where the $\pi/2$ pulse version allows for an inherently larger pulse bandwidth and is therefore more suited for paramagnetic species as they typically span over a large range of frequencies. However, the $\pi$ pulse version is less prone to signal loss as the magnetization is kept in the x-y plane and is preferably used when $T_2$ relaxation is long compared to the pulse length.

The PASS experiment is similar to the MAT experiment as such that it achieves a separation of the anisotropic and isotropic portions through a two-dimensional experiment. However, PASS introduces non-linear pulse timings resulting in a modulation of the anisotropic contribution in the indirect dimension as opposed to the MAT experiment where the indirect dimension showed the isotropic contribution.[17] The MAT and PASS experiments can be related by clever manipulation of the pulse and acquisition timings resulting in the MATPASS experiment, which incrementally separates the spinning sidebands in the indirect dimension as shown in Figure 2.8.[12,14] It shows a direct comparison of a stimulated echo spectrum of $Li_2MnO_3$ (a) to a MATPASS spectrum, where (b) is showing the summated spectra from (c) after a shearing transformation. It is evident, that the projected sum in (b) shows a much clearer distinction of the isotropic shifts than the stimulated echo sequence in Figure 2.8a. These experiments were performed using a projection-MATPASS pulse sequence, which utilizes solely $\pi/2$ pulses resulting in a larger bandwidth.[18]

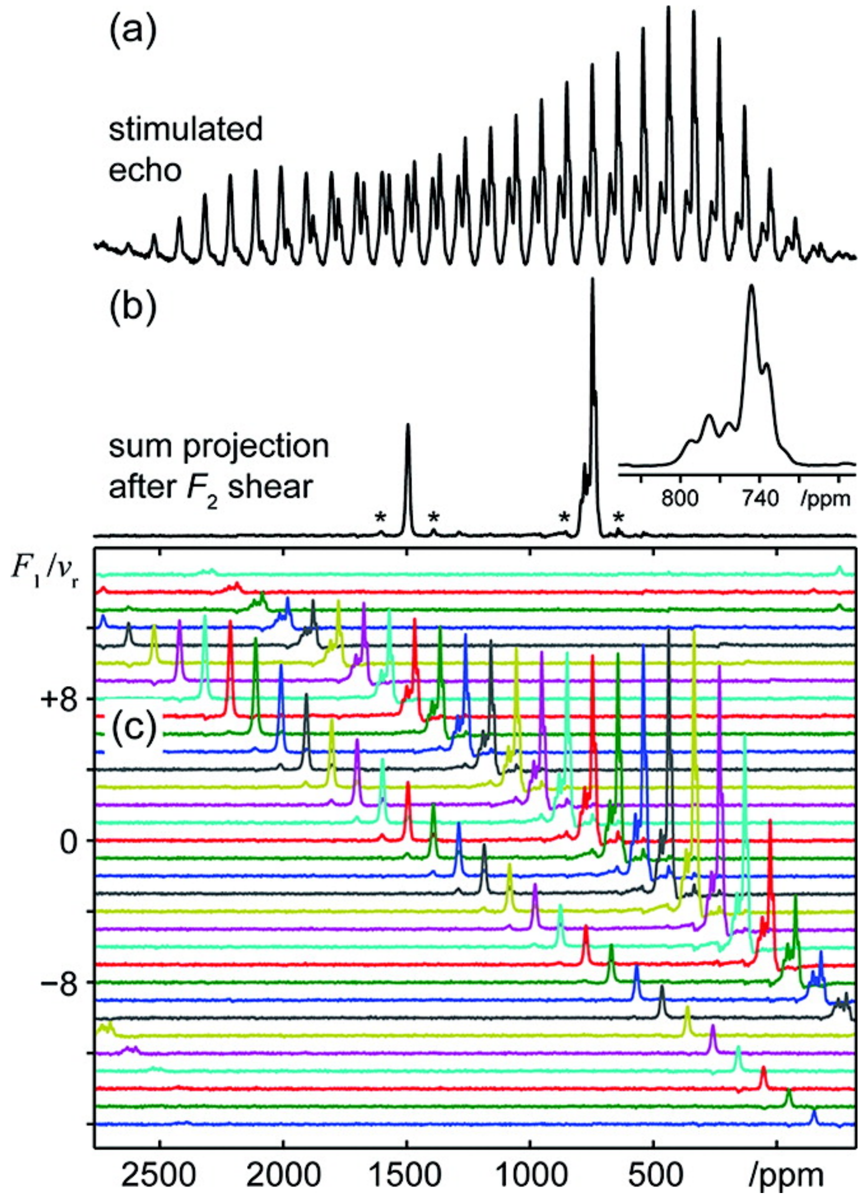

Figure 2.8: (a) $^7$Li MAS spectrum of $Li_2MnO_3$ (b) Isotropic spectrum obtained from summation of spinning sidebands of (c) 2D MATPASS spectrum. Asterisks denote residual spinning sidebands. Reprinted with permission from The Journal of the American Chemical Society, 2012, 134, 4, 1898–1901[12]. Copyright © 2012, American Chemical Society.

## 2.5 Magnetic Field Gradient NMR

During an NMR experiment, it is crucial for the static $\vec{B}_0$ field to be homogeneous in order to obtain high-resolution spectra. However, for a variety of techniques, it is desired to alter the magnetic field strength in order to get spatial information about the sample. This can be achieved by so-called field gradients, which are specialized coils surrounding the sample which introduce a linear variation to the magnetic field. The resonance condition under the influence of magnetic field gradients $\vec{G}$ can be written as[19]

$$\omega(r) = \gamma \vec{B}(r) = \gamma \left( \vec{B}_0 + \vec{r}\vec{G} \right) \tag{2.22}$$

where $\vec{G}$ can be applied along either the x, y or z-axis. The resonance frequency is then dependent on the position $r$. Magnetic field gradients are typically used in pulsed field gradient NMR and magnetic resonance imaging, which will be discussed in the following.

### 2.5.1 Pulsed Field Gradient NMR

In Appendix A diffusion coefficients of a novel polymer electrolyte are determined using pulsed-field gradient (PFG) NMR. PFG NMR is commonly used to study diffusion and transport properties in a variety of materials. The PFG pulse sequence combines two linear gradients with a stimulated echo sequence (Figure 2.9a) as introduced by Stejskal and Tanner.[20]

Figure 2.9b illustrates the changes of the spin phase for three different positions in the sample during a PFG experiment when no diffusion is occurring. After the inital $\pi/2$ pulse the magnetization is in the x-y plane and the

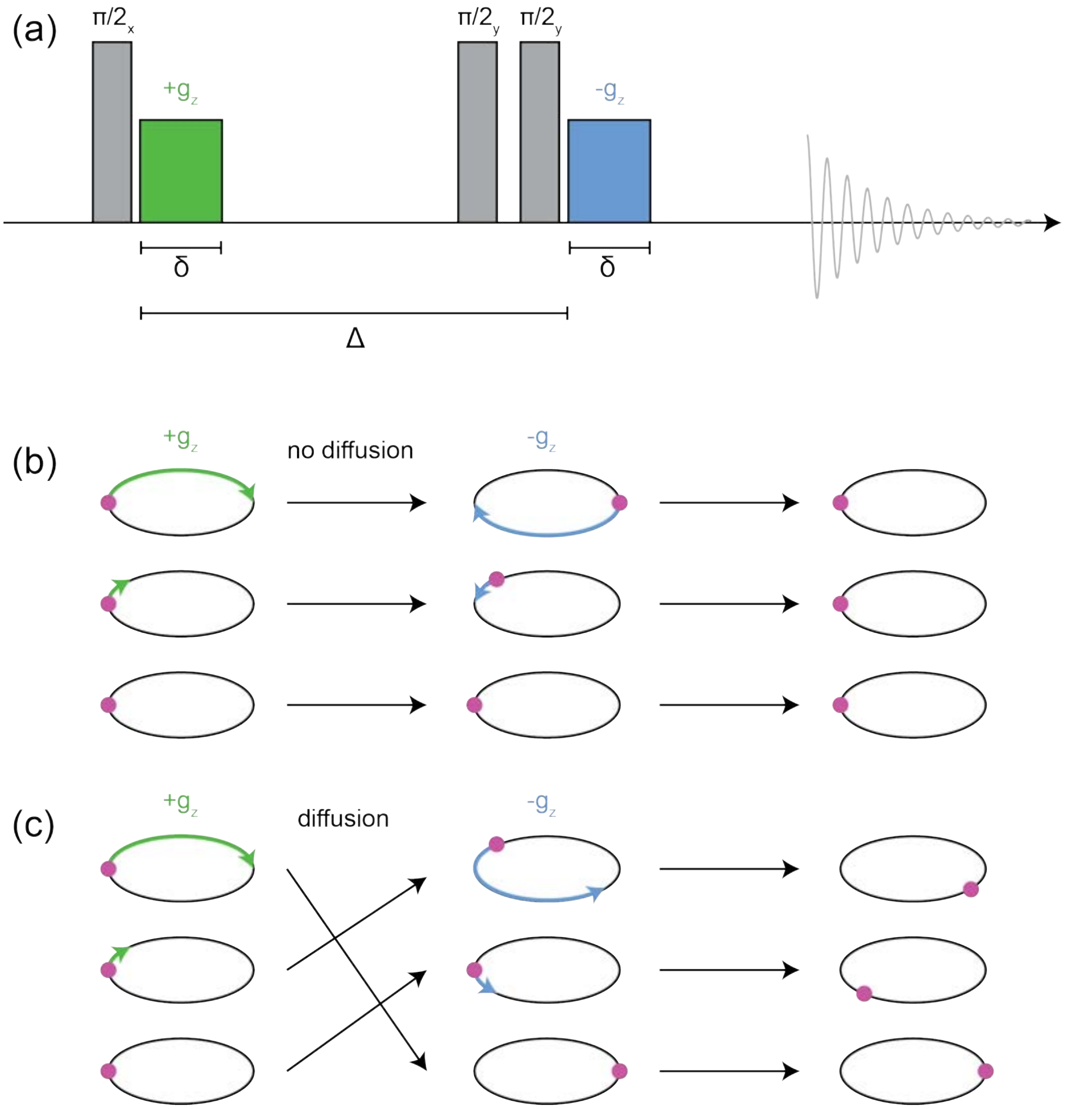

Figure 2.9: (a) pulse sequence for a stimulated echo PFG experiment.(b) Schematic of the phase of spins during a PFG experiment for a sample without diffusion (c) a sample with diffusion.[21].

subsequent field gradient (+g) then dephases the spins. When no diffusion is apparent, the phases are getting refocused by the second gradient (-g). If, however, there is diffusion throughout the sample, the scenario in Figure 2.9c takes place, where the spins change their position. The refocusing gradient then does not reverse the initial gradient, which results in an attenuation of

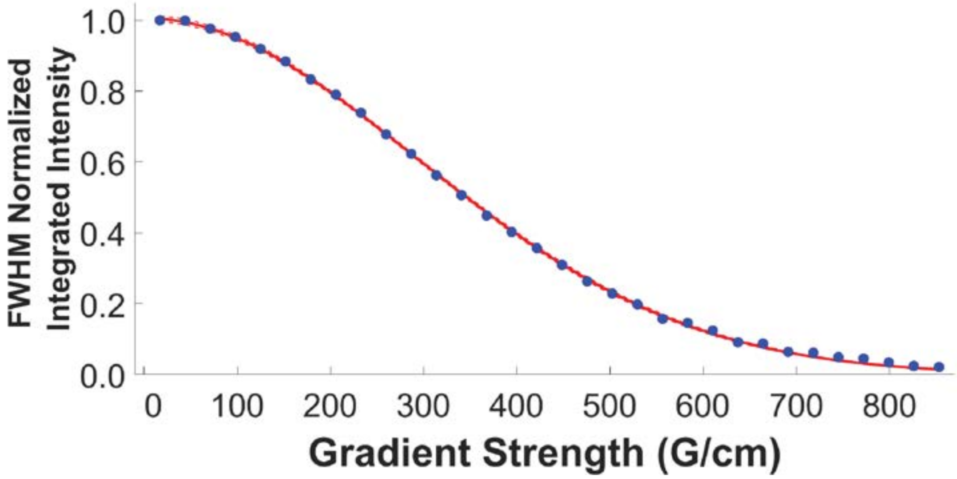

Figure 2.10: Example diffusion curve for a $^{7}$Li PFG NMR experiment for a lithium-containing polymer electrolyte.

the NMR signal. The signal attenuation can be correlated to the diffusion coefficient of the sample as

$$I = I_0 e^{-D\gamma^2 g^2 \delta^2 \left(\Delta - \frac{\delta}{3}\right)} \tag{2.23}$$

where $I$ and $I_0$ are the intensities of the signal with and without attenuation, respectively. $D$, $\gamma$, $g$, $\delta$ and $\Delta$ are the diffusion coefficient, gyromagnetic ratio, gradient strength, gradient pulse length and diffusion time, respectively.

In order to extract diffusion coefficients, a series of experiments with varying gradient strength is usually conducted. The attenuation of the signal can then be fit to an exponential decay curve where $\delta$ and $\Delta$ are kept constant. A typical diffusion curve can be seen in Figure 2.10.

### 2.5.2 Chemical Shift Imaging

In Chapter 5, chemical shift imaging (CSI) is applied in order to spatially resolve different species (electrolyte, lithium metal) in a parallel-plate resonator in situ cell. CSI is a type of imaging technique that relies on field gradients to phase-encode the spins along different axes with respect to the external $\vec{B}_0$ field.[19,22] This technique can be used in a two-dimensional fashion up to four dimensions, where the dimensions are the x, y and z-axis with respect to $\vec{B}_0$ and the chemical shift dimension. It provides not only spatial information but also gives a spectral dimension, which allows for the distinction between different species inside the active volume. This is different from a frequency-encoding technique, where the spectral dimension is lost during acquisition of the signal. Figure 2.11 shows the CSI pulse sequence used in Chapter 5, which was used to image the distribution of electrolyte and lithium metal inside

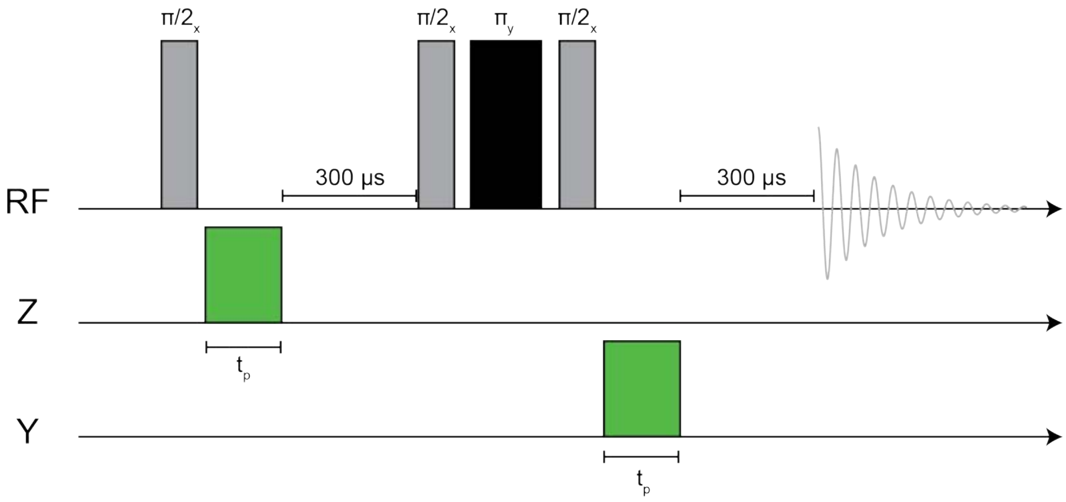

Figure 2.11: Chemical shift imaging pulse sequence. The Z and Y gradient strength is incremented with each experiment. $t_p$ is the phase encoding time. The 300 µs delay after the gradient is necessary avoid distortion of the image. The corresponding pulse program sequence is shown in Appendix B.

an electrochemical cell. The images were acquired in three dimension: the Y dimension, Z dimension and spectral dimension. Here the green boxes in the Z and Y dimension are the gradients with respect to $\vec{B}_0$. After the initial 90° pulse, the spin phase is encoded in the Z dimension similar to the gradient applied in the PFG pulse sequence (Figure 2.9a). However, in CSI no refocusing gradient is applied which results in a phase-encoded signal, which contains spatial information along said axis. After the composite step, a gradient along the Y axis is applied in order to encode the spin phases along that dimension. This leads to a resulting signal that has spatial information about the Z and Y axis in addition to a spectral dimension. In magnetic resonance imaging, the spatial information is collected in k-space, where

$$\boldsymbol{k} = \gamma \boldsymbol{G} t \tag{2.24}$$

with $\boldsymbol{k}$ as the reciprocal space vector. In order to obtain a three-dimensional image, the gradient strength for Y and Z has to incremented in a step-wise way in order to "map out" all points in k-space. Figure 2.12 shows an example for an experiment where the Y dimension is sampled over 16 steps, and the Z dimension over 32 steps. The CSI experiment uses 16 x 32 experiments to collect an image, which is obtained by applying a Fourier transform to the collected k-space signal along the Y, Z and spectral domain. This is one major disadvantage of CSI, as it dramatically increases the experiment time compared to other imaging experiments that utilize frequency-encoding. Frequency-encoding allows for a much faster acquisition as the spatial information is encoded during the signal acquisition. However, in order to obtain spectral information CSI is the imaging technique of choice. It is also important to note, that CSI is limited to materials

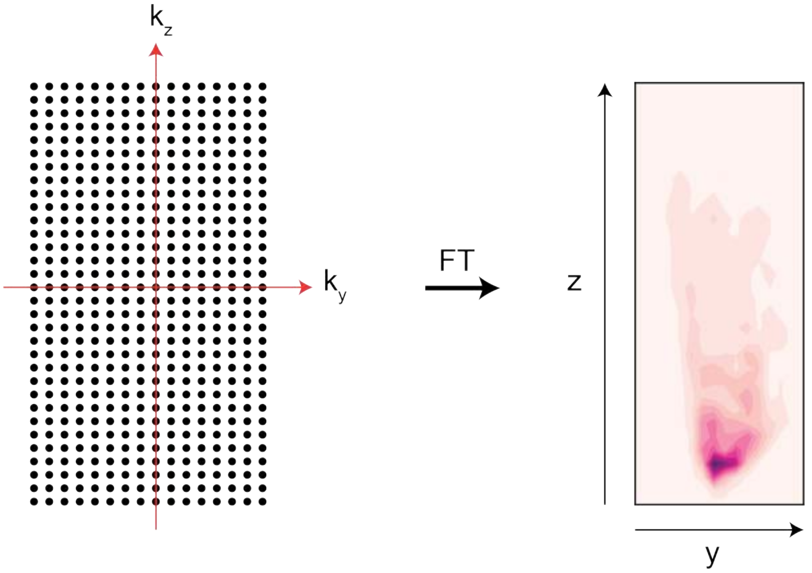

Figure 2.12: k-space map with 16 steps in the Y dimension and 32 steps in the Z dimension. Fourier transform (FT) leads to an image along the z and y-axis.

with slow relaxation due to the long gradient stabilization time (300 µs), which makes it difficult to obtain information about paramagnetic materials (most cathode materials) with fast relaxation parameters. However, techniques exist, which allow for the magnetic resonance imaging (MRI) analysis of cathode materials. Tang et al., for example, introduced a technique called scanning image-selected in situ spectroscopy (S-ISIS) which allowed them to image a $LiCoO_2/Li_4Ti_5O_{12}$ battery in operando.[23] This technique is less prone to suffer from signal loss due to $T_2$ relaxation and provides a good basis for in situ MRI of such materials.

## 2.6 In Situ NMR Methods

Over the last two decades in situ NMR has become an indispensable tool to study battery materials. Not only does it allow for the simultaneous monitoring of both liquid and solid components (electrolyte, cathode, anode, separator) but it also provides timely data acquisition making it a great method to extract real-time information about structural changes, degradation products and failure mechanisms in batteries.

The general setup usually consists of an in situ battery cell, which is carefully positioned inside an NMR magnet and connected to a battery cycler. Here, an introduction to the most common designs, challenges and applications is given.

### 2.6.1 Design

The design of an in situ NMR electrochemical cell is of utmost importance in order to achieve reliable and reproducible results. The most common geometries include adaptations of coin, pouch and Swagelok cells as illustrated in Figure 2.13. Gerald et al. first introduced a coin cell design to investigate the intercalation of lithium into graphitic carbon.[24] However, the NMR detector of choice, a toroid, produces an inhomogeneous $\vec{B}_1$ field, which increases the

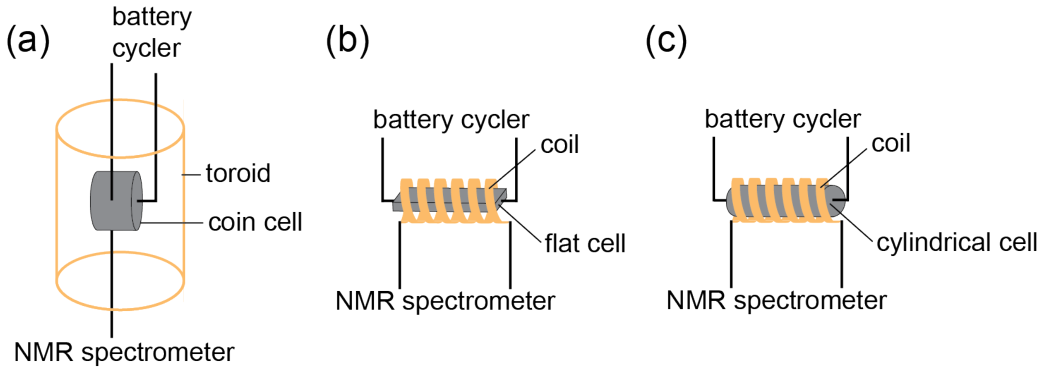

Figure 2.13: Common in situ NMR designs for battery monitoring (a) toroid NMR detector with a coin-cell type battery (b) regular NMR coil detector with a flat pouch cell type design (c) regular NMR coil design with a cylindrical stacked electrochemical cell.

acquisition time immensely. In addition, composite pulses had to be used in order to overcome the field inhomogeneities issues. A flat bag or pouch cell design was later introduced by Letellier et al.[25] The electrodes (carbon cloth and lithium metal) were sandwiched between mesh current collectors and sealed inside an aluminum bag before being placed inside a 10 mm NMR coil. This setup allowed for a much faster acquisition time (11 hours for the toroid vs. 8 minutes for the flat bag design), which made it possible to run these experiments in operando (the battery cycling was not stopped during NMR data acquisition). A cylindrical design, where the electrodes, separator and current collectors are stacked was implemented by Poli et al.[26] This design is less prone to solvent leakage compared to the above mentioned cells, which is a major challenge in in situ battery assembly.

In addition, the filling factor, which is defined by the ratio of the sample volume observed by the resonator to the volume of the resonator, is an important parameter to consider when designing cells for in situ NMR. It is desired to increase the filling factor by matching either the in situ cell shape to the resonator or vice versa. The solenoid coil design coupled with a cylindrical in situ cell design is preferred to other resonator designs as it provides great field homogeneity and the in situ cell components can be either stacked or rolled in a cylindrical fashion. The toroid resonator design suffers from large field inhomogeneities in addition to a fair amount of “dead space” resulting in long experiment times even at high sample loadings. Imaging studies are usually conducted using saddle coil designs, which are necessary to ensure RF penetration from the surrounding gradient coils. MRI utilizing saddle coils and cylindrical battery designs has provided insights into the spatial distribution of liquid electrolytes and electrodes through this in situ technique.[23,27] Recently, a parallel-plate resonator design was introduced for spectroscopic studies of flat cell batteries.[28] This design allows for an improved filling factor compared to coupling flat cells with solenoid coils as well as great field homogeneity throughout the active volume of the resonator.

It is important to note, that in situ measurements to date are performed under static conditions, which limits the resolution of the acquired NMR spectra. Most studies investigate the intercalation of lithium on the anode side in a half-cell setup, where the counter electrode is lithium metal. Cathode materials usually require the use of magic-angle spinning (MAS) to obtain well-resolved spectra. Chapter 3 introduces a cylindrical jelly-roll type in situ cell utilizing cellulose-based electrodes to increase the filling factor of active material inside these cells. In Chapter 4 this design is further optimized to allow for MAS to be applied to a full-cell format. In addition, a flat cell design is revisited in Chapter 5 which is coupled with a parallel-plate NMR detector. This type of setup enables new studies including MRI and monitoring of fast-charging of full-cells.

### 2.6.2 Challenges

When it comes to performing in situ NMR experiments on electrochemical cells certain factors have to be considered. Not only spectroscopic considerations have to be taken into account but also the materials used for manufacturing the cells have to be carefully chosen.

It is important to consider the orientation of the electrochemical cell inside the magnet, because the cell components can cause variations of the local magnetic fields which is known as the bulk magnetic susceptibility (BMS)

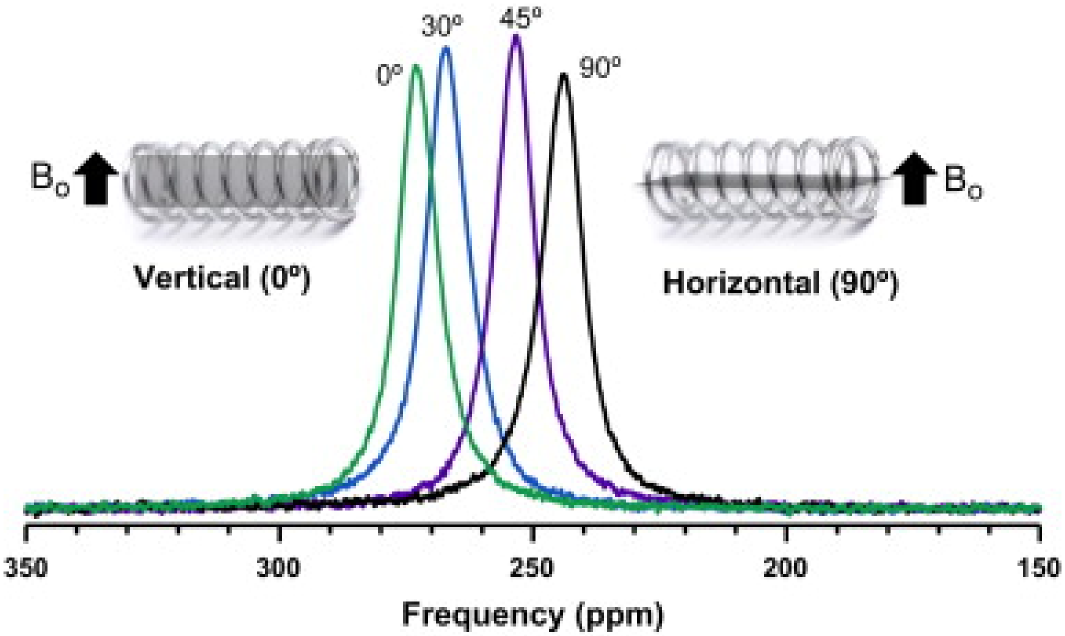

Figure 2.14: Bulk magnetic susceptibility effect on the $^7$Li NMR shift of lithium metal. The different alignment angles of the lithium metal strip with respect to $\vec{B}_0$ gives different shift values. Reprinted with permission from the Journal of Solid State Nuclear Magnetic Resonance, 2012, 42, 62-70.[29] Copyright © 2012, with permission from Elsevier.

effect. One example is the orientation dependence of a lithium metal strip when rotated with respect to the $\vec{B}_0$ field.[29] The frequency shift can span over a wide range where the highest shifts are obtained at a vertical orientation of lithium metal with respect to $\vec{B}_0$ and the lowest for a horizontal orientation as shown in Figure 2.14. Therefore, careful placement and alignment is crucial to obtain reproducible results. Interestingly, the BMS effect can be exploited when observing lithium deposition in electrochemical cells, where so-called dendrites may form on the surface of the electrode. These fine structures are usually growing like perpendicular "roots" with respect to the electrode and can therefore be easily distinguished by the shift difference to lithium metal that is plated flat onto the surface.

In addition, solvent leakage and pressure differences inside the electrochemical cells are difficult to prevent in in situ cells. Typically, the cell is encased in either a polymeric bag or capsule. Because these cells are manufactured by hand, even small misalignments can cause a large variability in performance. This leads to a finite life-time of these cells, which is on the order of a few hours to days.[29] As a result, the in situ NMR experiments have to be carefully planned in order to obtain data in a reasonable time frame. One way to circumvent solvent leakage is by using aluminum-coated bags to seal the cell. Although this allows for a longer life time of these cells, it introduces new challenges in terms of signal loss due to the decreased skin depth of the RF pulse through the aluminum. To obtain a good signal-to-noise ratio, it is desired to minimize the metallic components in the in situ cell. This is why mesh-like current collectors and polymeric bag cells are most commonly used for in situ NMR of battery materials.

Now, with a limited time frame, the user has to make sure that the data collection does not exceed the life time of the in situ battery. This is hindered by the vast difference in $T_1$ relaxation for the different components. The liquid electrolyte usually has much longer $T_1$ values than the lithiated species in the electrodes. This makes it exceedingly difficult to obtain quantitative data of all components simultaneously. In addition, most in situ experiments on battery materials are performed under static conditions, which limits the achievable spectral resolution. Most cathodes span over a large range of frequencies due to their paramagnetic nature and without the use of MAS NMR, it becomes increasingly difficult to resolve these peaks due to their inherent spin interactions, which are described in more detail in Section 2.6.3.3.

Nevertheless, in situ NMR is a powerful tool to investigate the changes inside a LIB under working conditions, which can give a vast amount of information about structural changes of the electrodes, the formation of the SEI and electrolyte degradation. Some successful applications of in situ NMR for battery materials are introduced in the following.

### 2.6.3 Applications

Since the first in situ NMR studies were conducted on battery materials in 2001[24], major advances in the field have taken place leading to some insightful studies on LIB materials over the past two decades. A few of these studies are highlighted in the following.

#### 2.6.3.1 In Situ $^7$Li NMR on Graphitic and Disordered Carbon

The initial in situ NMR studies focussed on elucidating the lithiation mechanism in hard carbon and graphite.[25,30–34] These studies laid the groundwork for real-time monitoring of batteries using NMR. Although plagued by a low signal-to-noise and long-term stability issues, some remarkable insights into the intercalation chemistry of hard carbon and graphite were provided through this technique. Gerald et al. were able to resolve lithium environments in the graphene layers in graphitic carbon (dilute and concentrated stages), lithium in the electrolyte, and inorganic lithium species in the SEI along the first electrochemical cycle.[24] Similarly, the lithiation mechanism in hard carbon has been investigated.[25,31,32] Some key differences were found for these types of materials due to their inherent disordered structure. A gradual shift of the lithiated carbon in the $^7$Li NMR spectra as a function of charge is apparent rather than going through distinct stages as it is in the case of graphite. These differences

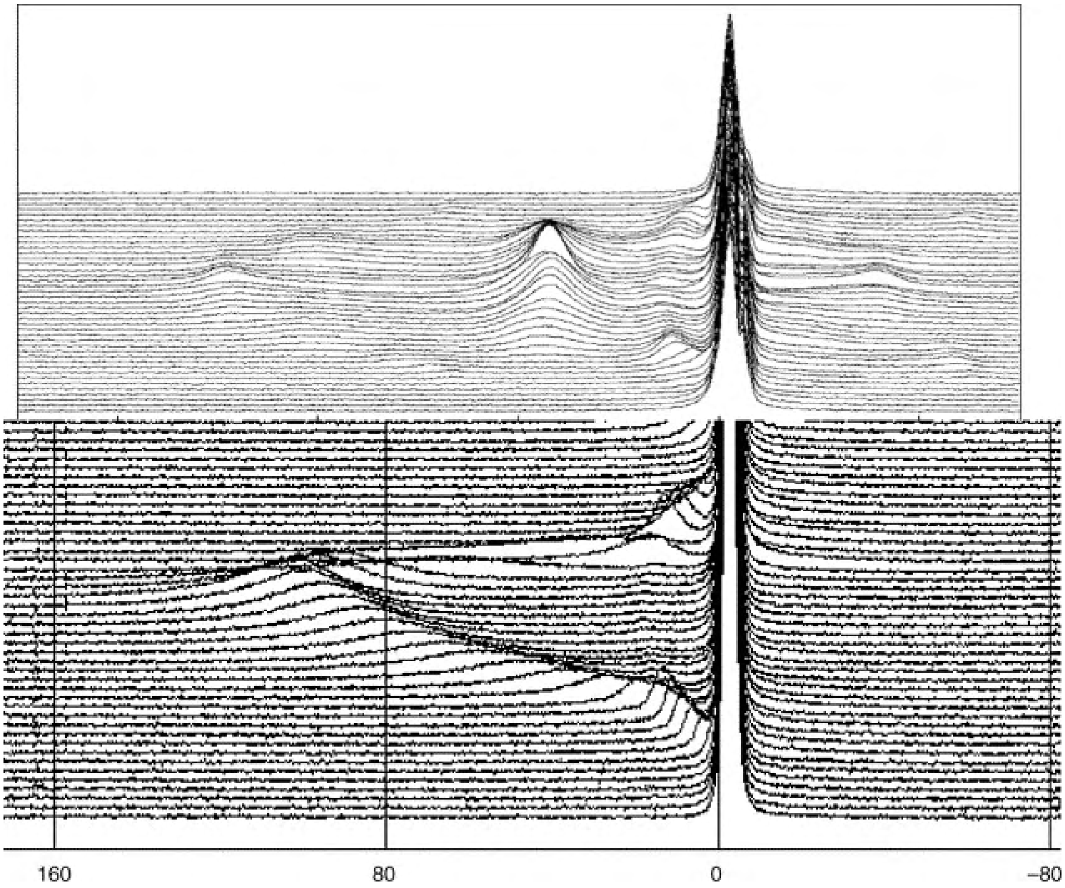

Figure 2.15: In situ $^7$Li NMR during the first electrochemical cycle; (top) lithium intercalation into graphite from bottom to top (bottom) lithium intercalation into a carbon/carbon composite Reprinted with permission from the Journal of Physics and Chemistry of Solids, 2006, 67, 1228-1232.[32] Copyright © 2006, with permission from Elsevier.

are illustrated in Figure 2.15. The top spectra show the intercalation of lithium into graphite, where the intercalation goes through the distinct dilute stages $LiC_{36}$, $LiC_{27}$ and $LiC_{18}$ at low levels of lithiation, corresponding to shift values between 2 ppm to 12 ppm followed by the concentrated stages $LiC_{12}$ (45 ppm) and $LiC_6$ (43 ppm) at high levels of lithiation. However, disordered carbon (Figure 2.15) follows a more gradual shift profile, where only two different sites can be distinguished, one site is found in the shift range of −2 ppm to 18 ppm corresponding to the intercalation of lithium into graphitic-like coating, and a second site that continuously moves to higher shift values until it reaches 104 ppm at the end of lithiation, corresponding to a lithium insertion into the carbon core structure.

A vast amount of in situ studies are performed in a half-cell format, meaning that lithium metal is used as a counter electrode to the electrode of interest. This enables better resolution of the lithiated phases of interest. Though to properly represent the workings of a LIB under operating conditions, it is favoured to use a full-cell format. Gotoh et al. investigated the cycling behaviour of positive (LCO, NCA, and LMO) and negative electrodes (graphite and hard carbon) under different charging conditions using in situ $^7$Li NMR.[35] They found that different cathode materials had varying effects on the $^7$Li NMR shifts of the intercalation stages in graphite. Static in situ NMR does not provide great resolution of the phase changes in most cathode materials due to their paramagnetic nature, which limited this study to the effects on the anode material. However, they further investigated the effects of overcharging of the in situ cells which lead to an appearance of a lithium metal resonance at 260 ppm after overcharging to 170%, which partially disappeared during delithiation. This showed that in situ $^7$Li NMR can be used to quantify the amount of lithium plated in LIBs under overcharging conditions. Several studies on the dynamics of lithium intercalation and diffusion properties in graphite anodes have been published giving further insights into the complex mechanisms behind this process.[27,28,34,36–39]

#### 2.6.3.2 In Situ $^{7}$Li NMR on Silicon Anodes

Silicon anodes were first investigated through in situ NMR by Key et al. in 2009.[8,40] The electrochemical lithiation mechanism of silicon proved to be problematic to elucidate with other spectroscopic methods like X-ray diffraction due to the amorphous nature of the silicon network. In situ $^{7}$Li NMR, however, allowed for the characterization of different Li-Si alloy phases during lithiation. They grouped the lithium silicides into three groups with different type of domains, which they denoted as phase 1, 2 and 3. Figure 2.16 summarizes the $^{7}$Li NMR shifts of all lithium silicide phase during lithiation. Phase 1 corresponds to polymeric silicon clusters with isolated lithium distributed in the network at chemical shift values of 0 ppm to 10 ppm. At higher states of lithiation, these clusters are broken down into star-, and dumbbell-shaped Si

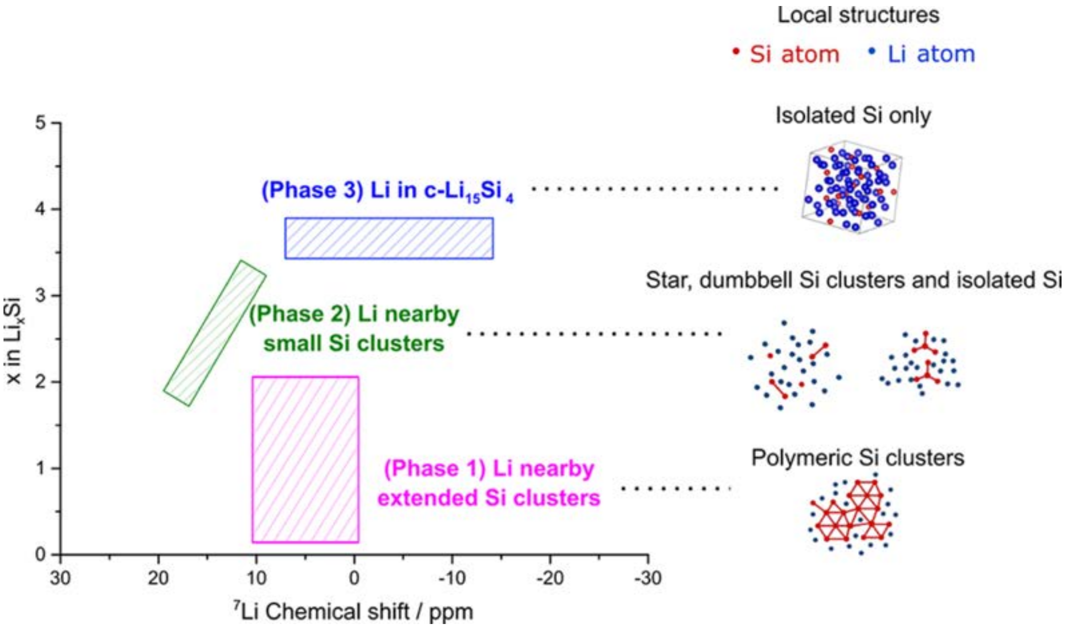

Figure 2.16: $^{7}$Li chemical shifts and structures of $Li_xSi$ phases as a function of state of charge. Reprinted with permission from The Journal of the American Chemical Society, 2019, 141, 17, 7014–7027[41]. Copyright © 2019, American Chemical Society.

clusters with some isolated silicon, with shift values in the range of 10 ppm to 20 ppm. Interestingly, they identified a phase at the end of discharge, which was not visible during ex situ $^7$Li NMR between 5 ppm to −15 ppm. Further analysis of that particular phase revealed, that it corresponds to a metastable overlithiated $Li_{15}Si_4$ phase (phase 3), which is of crystalline nature. Such findings were only made possible through in situ NMR, as the short life-time of such phases are difficult to observe during ex situ experiments, which require the disassembly of cycled coin cells before NMR analysis. Further studies of the lithiation of nanowire silicon and silicon monoxide have also been conducted revealing differences in the lithiation behaviour of these types of materials depending on their particle size and shape.[41–43].

In situ NMR studies on silicon anodes are sparse. In this work two new studies are introduced, which focus on the use of silicon monoxide as an alternative anode material for LIBs and the fast-charging behaviour of silicon anodes in a full-cell format. These studies aim to advance the understanding of the real-time operation of silicon anodes.

#### 2.6.3.3 In Situ $^7$Li NMR on Cathode Materials

In situ NMR analysis of cathode materials is hindered due to the fact that to date these studies have only been performed under static conditions. Most cathode materials are of paramagnetic nature, which leads to broad signals in the NMR spectrum. Ex situ studies are more commonly used, as they allow for magic-angle spinning (MAS), which increases the resolution in the NMR spectrum immensely. However, some in situ studies on $LiCoO_2$, $Li_2MnO_3$, $Li_{1.2}Ni_{0.2}Mn_{0.6}O_2$, $Li_{1.2}Ni_{0.13}Mn_{0.54}Co_{0.13}O_2$, $Li_{1.08}Mn_{1.92}O_4$, and $LiNi_{0.8}Mn_{0.1}Co_{0.1}O_2$ exist.[44–47]

Shimoda et al. investigated the lithium extraction and insertion in $LiCoO_2$ (LCO) through in situ $^7$Li NMR. Although the static line shapes were poorly resolved, they were able to monitor the change in peak width and position by cross-referencing the data obtained from the static spectra to findings from a separate ex situ NMR study.[44] They found, that the peak shift was highly dependent on the orientation of the cell with respect to the $\vec{B}_0$ field due to the BMS effect. However, they were able to monitor the shift of the delithiated $Li_xCoO_2$ phase, which moved to around 100 ppm up to $x = 0.5$ before decreasing in shift values for $x < 0.5$. They attributed this effect to the change of the interlayer spacing in the LCO structure, which is related to the amount of lithium in the structure.

A study on $Li_{1.08}Mn_{1.92}O_4$ was performed using in situ $^7$Li NMR. A much broader signal was observed making it difficult to extract information from these data sets. Instead the authors performed relaxation studies to monitor the lithium mobility as a state of charge at different temperatures.

The general trend in in situ NMR studies of cathode materials is to combine these studies with ex situ MAS NMR to verify peak assignment. Chapter 4 introduces a novel technique, which allows for in situ MAS NMR analysis of a battery. This revolutionary technique makes it possible to perform in situ studies with increased resolution due to MAS, which forms the basis for new avenues in the field of in situ NMR analysis of battery materials.

# Bibliography

[1] Malcolm H. Levitt. *Spin Dynamics.* John Wiley & Sons, 2008.

[2] James Keeler. *Understanding NMR Spectroscopy.* John Wiley & Sons, 2010.

[3] David Apperley, Robin Harris, and Paul Hodgkinson. *Solid-State NMR: Basic Principles & Practice.* Momentum Press, 2012.

[4] Melinda J Duer. *Solid state NMR Spectroscopy: Principles and Applications.* John Wiley & Sons, 2008.

[5] Timothy P Hanusa. *The Lightest Metals: Science and Technology from Lithium to Calcium.* John Wiley & Sons, 2015.

[6] W. D. Knight. Nuclear Magnetic Resonance Shift in Metals. *Physical Review*, 76(8):1259–1260, 1949.

[7] Emilie Bekaert, Florent Robert, Pierre Emmanuel Lippens, and Michel Ménétrier. $^7$Li NMR Knight Shifts in Li– Sn Compounds: MAS NMR Measurements and Correlation with DFT Calculations. *The Journal of Physical Chemistry C*, 114(14):6749–6754, 2010.

[8] Baris Key, Rangeet Bhattacharyya, Mathieu Morcrette, Vincent Seznec, Jean-Marie Tarascon, and Clare P Grey. Real-time NMR investigations of structural changes in silicon electrodes for lithium-ion batteries. *Journal of the American Chemical Society*, 131(26):9239–9249, 2009.

[9] Zhiyun Wu, Hellmut Eckert, Jürgen Senker, Dirk Johrendt, Gunter Kotzyba, Bernd D Mosel, Henning Trill, Rolf-Dieter Hoffmann, and Rainer

Pöttgen. Ternary Stannides Li$T$Sn$_4$ ($T$= Ru, Rh, Ir) —Chemical Bonding and Physical Properties. *The Journal of Physical Chemistry B*, 107(9): 1943–1948, 2003.

[10] Susanne Penzel, Andres Oss, Mai-Liis Org, Ago Samoson, Anja Böckmann, Matthias Ernst, and Beat H Meier. Spinning faster: protein NMR at MAS frequencies up to 126 kHz. *Journal of Biomolecular NMR*, 73(1-2): 19–29, 2019.

[11] Yusuke Nishiyama, Steven P Brown, Zhehong Gan, Laurent Delevoye, Luke O'Dell, Detlef Reichert, Michael Vogel, Denis Arcon, Jonathan Stebbins, Henrike Heise, et al. *Modern Methods in Solid-state NMR: A Practitioner's Guide*. Royal Society of Chemistry, 2018.

[12] Ivan Hung, Lina Zhou, Frederique Pourpoint, Clare P Grey, and Zhehong Gan. Isotropic high field NMR spectra of Li-ion battery materials with anisotropy >1 MHz. *Journal of the American Chemical Society*, 134(4): 1898–1901, 2012.

[13] Annica I Freytag, Allen D Pauric, Sergey A Krachkovskiy, and Gillian R Goward. In Situ Magic-Angle Spinning $^7$Li NMR Analysis of a Full Electrochemical Lithium-Ion Battery Using a Jelly Roll Cell Design. *Journal of the American Chemical Society*, 141(35):13758–13761, 2019.

[14] Ivan Hung and Zhehong Gan. On the magic-angle turning and phase-adjusted spinning sidebands experiments. *Journal of Magnetic Resonance*, 204(1):150–154, 2010.

[15] AD Bax, Nikolaus M Szeverenyi, and Gary E Maciel. Correlation of isotropic shifts and chemical shift anisotropies by two-dimensional Fourier-

transform magic-angle hopping NMR spectroscopy. *Journal of Magnetic Resonance (1969)*, 52(1):147–152, 1983.

[16] Zhehong Gan. High-resolution chemical shift and chemical shift anisotropy correlation in solids using slow magic angle spinning. *Journal of the American Chemical Society*, 114(21):8307–8309, 1992.

[17] Oleg N Antzutkin, SC Shekar, and Malcolm H Levitt. Two-dimensional sideband separation in magic-angle-spinning NMR. *Journal of Magnetic Resonance, Series A*, 115(1):7–19, 1995.

[18] Brennan J Walder, Krishna K Dey, Derrick C Kaseman, Jay H Baltisberger, and Philip J Grandinetti. Sideband separation experiments in NMR with phase incremented echo train acquisition. *The Journal of Chemical Physics*, 138(17):174203, 2013.

[19] Robin A De Graaf. *In vivo NMR spectroscopy: principles and techniques.* John Wiley & Sons, 2019.

[20] E. O. Stejskal and J. E. Tanner. Spin diffusion measurements: Spin echoes in the presence of a time-dependent field gradient. *The Journal of Chemical Physics*, 42(1):288–292, 1965.

[21] William S. Price. Pulsed-field gradient nuclear magnetic resonance as a tool for studying translational diffusion: Part 1. Basic theory. *Concepts in Magnetic Resonance*, 9(5):299–336, 1997.

[22] Paul T Callaghan. *Principles of nuclear magnetic resonance microscopy.* Oxford University Press on Demand, 1993.

[23] Mingxue Tang, Vincent Sarou-Kanian, Philippe Melin, Jean-Bernard Leriche, Michel Ménétrier, Jean-Marie Tarascon, Michaël Deschamps, and Elodie Salager. Following lithiation fronts in paramagnetic electrodes with in situ magnetic resonance spectroscopic imaging. *Nature communications*, 7(1):1–8, 2016.

[24] RE Gerald II, J Sanchez, CS Johnson, RJ Klingler, and JW Rathke. In situ nuclear magnetic resonance investigations of lithium ions in carbon electrode materials using a novel detector. *Journal of Physics: Condensed Matter*, 13(36):8269, 2001.

[25] Michel Letellier, Frédéric Chevallier, Christian Clinard, Elzbieta Frackowiak, Jean-Noël Rouzaud, Francois Beguin, Mathieu Morcrette, and Jean-Marie Tarascon. The first in situ $^7$Li nuclear magnetic resonance study of lithium insertion in hard-carbon anode materials for Li-ion batteries. *The Journal of Chemical Physics*, 118(13):6038–6045, 2003.

[26] Fabrizia Poli, Jugeshwar S Kshetrimayum, Laure Monconduit, and Michel Letellier. New cell design for in-situ NMR studies of lithium-ion batteries. *Electrochemistry Communications*, 13(12):1293–1295, 2011.

[27] Sergey A. Krachkovskiy, Jamie M. Foster, J. David Bazak, Bruce J. Balcom, and Gillian R. Goward. Operando Mapping of Li Concentration Profiles and Phase Transformations in Graphite Electrodes by Magnetic Resonance Imaging and Nuclear Magnetic Resonance Spectroscopy. *The Journal of Physical Chemistry C*, 122(38):21784–21791, 2018.

[28] Sergey A. Krachkovskiy, Mohammad Reza, Andres Ramirez Aguilera, Ion C. Halalay, Bruce J. Balcom, and Gillian R. Goward. Real-time

quantitative detection of lithium plating by in situ NMR using a parallel-plate resonator. *Journal of The Electrochemical Society*, 167(13):130514, 2020.

[29] Nicole M Trease, Lina Zhou, Hee Jung Chang, Ben Yunxu Zhu, and Clare P Grey. In situ NMR of lithium ion batteries: Bulk susceptibility effects and practical considerations. *Solid state nuclear magnetic resonance*, 42: 62–70, 2012.

[30] Fea Chevallier, M Letellier, M Morcrette, J-M Tarascon, E Frackowiak, J-N Rouzaud, and F Béguin. In situ $^7$Li-nuclear magnetic resonance observation of reversible lithium insertion into disordered carbons. *Electrochemical and solid-state letters*, 6(11):A225–A228, 2003.

[31] Michel Letellier, Frédéric Chevallier, François Béguin, Elzbieta Frackowiak, and Jean-Noël Rouzaud. The first in situ $^7$Li NMR study of the reversible lithium insertion mechanism in disorganised carbons. *Journal of Physics and Chemistry of Solids*, 65(2-3):245–251, 2004.

[32] Michel Letellier, Frédéric Chevallier, and François Beguin. In situ $^7$Li NMR during lithium electrochemical insertion into graphite and a carbon/carbon composite. *Journal of Physics and Chemistry of Solids*, 67(5):1228–1232, 2006.

[33] Michel Letellier, Frédéric Chevallier, and Mathieu Morcrette. In situ $^7$Li nuclear magnetic resonance observation of the electrochemical intercalation of lithium in graphite; 1st cycle. *Carbon*, 45(5):1025–1034, 2007.

[34] Frédéric Chevallier, Fabrizia Poli, Bénédicte Montigny, and Michel Letellier. In situ $^7$Li nuclear magnetic resonance observation of the electrochemical

intercalation of lithium in graphite: second cycle analysis. *Carbon*, 61: 140–153, 2013.

[35] Kazuma Gotoh, Misato Izuka, Juichi Arai, Yumika Okada, Teruyasu Sugiyama, Kazuyuki Takeda, and Hiroyuki Ishida. In situ $^7$Li nuclear magnetic resonance study of the relaxation effect in practical lithium ion batteries. *Carbon*, 79:380–387, 2014.

[36] Steffen A Kayser, Achim Mester, Andreas Mertens, Peter Jakes, Rüdiger-A Eichel, and Josef Granwehr. Long-run in operando NMR to investigate the evolution and degradation of battery cells. *Physical Chemistry Chemical Physics*, 20(20):13765–13776, 2018.

[37] Jose L Lorie Lopez, Philip J Grandinetti, et al. Enhancing the real-time detection of phase changes in lithium–graphite intercalated compounds through derivative operando (dOp) NMR cyclic voltammetry. *Journal of Materials Chemistry A*, 6(1):231–243, 2018.

[38] Frederic Blanc, Michal Leskes, and Clare P Grey. In situ solid-state NMR spectroscopy of electrochemical cells: batteries, supercapacitors, and fuel cells. *Accounts of chemical research*, 46(9):1952–1963, 2013.

[39] J Arai, Y Okada, T Sugiyama, M Izuka, K Gotoh, and K Takeda. In situ solid state $^7$Li NMR observations of lithium metal deposition during overcharge in lithium ion batteries. *Journal of The Electrochemical Society*, 162(6):A952–A958, 2015.

[40] Baris Key, Mathieu Morcrette, Jean-Marie Tarascon, and Clare P Grey. Pair distribution function analysis and solid state NMR studies of silicon electrodes for lithium ion batteries: understanding the (de)lithiation

mechanisms. *Journal of the American Chemical Society*, 133(3):503–512, 2010.

[41] Keitaro Kitada, Oliver Pecher, Pieter C. M. M. Magusin, Matthias F. Groh, Robert S. Weatherup, and Clare P. Grey. Unraveling the reaction mechanisms of SiO anodes for Li-ion batteries by combining in situ $^{7}$Li and ex situ $^{7}$Li/$^{29}$Si solid-state NMR spectroscopy. *Journal of the American Chemical Society*, 141(17):7014–7027, 2019.

[42] Ken Ogata, E Salager, CJ Kerr, AE Fraser, Caterina Ducati, Andrew James Morris, Stephan Hofmann, and Clare Philomena Grey. Revealing lithium–silicide phase transformations in nano-structured silicon-based lithium ion batteries via in situ NMR spectroscopy. *Nature communications*, 5(1): 1–11, 2014.

[43] Takakazu Hirose, Masanori Morishita, Hideya Yoshitake, and Tetsuo Sakai. Study of structural changes that occurred during charge/discharge of carbon-coated SiO anode by nuclear magnetic resonance. *Solid State Ionics*, 303:154–160, 2017.

[44] Keiji Shimoda, Miwa Murakami, Daiko Takamatsu, Hajime Arai, Yoshiharu Uchimoto, and Zempachi Ogumi. In situ NMR observation of the lithium extraction/insertion from $LiCoO_2$ cathode. *Electrochimica Acta*, 108:343–349, 2013.

[45] Lina Zhou, Michal Leskes, Tao Liu, and Clare P Grey. Probing Dynamic Processes in Lithium-Ion Batteries by In Situ NMR Spectroscopy: Application to $Li_{1.08}Mn_{1.92}O_4$ Electrodes. *Angewandte Chemie*, 127(49): 14995–14999, 2015.

[46] Xiang Li, Mingxue Tang, Xuyong Feng, Ivan Hung, Alyssa Rose, Po-Hsiu Chien, Zhehong Gan, and Yan-Yan Hu. Lithiation and Delithiation Dynamics of Different Li Sites in Li-Rich Battery Cathodes Studied by Operando Nuclear Magnetic Resonance. *Chemistry of Materials*, 29(19): 8282–8291, 2017.

[47] Katharina Märker, Chao Xu, and Clare P. Grey. Operando NMR of NMC811/graphite lithium-ion batteries: Structure, dynamics, and lithium metal deposition. *Journal of the American Chemical Society*, 2020.

# Chapter 3

# $^{7}$Li and $^{29}$Si NMR Enabled by High-Density Cellulose-Based Electrodes in the Lithiation Process in Silicon and Silicon Monoxide Anodes

*The following chapter is adapted from the publication in the Journal of Physical Chemistry C (J. Phys. Chem. C 2019, 123, 11362-11368). The data collection was performed by Allen D. Pauric (in situ $^{7}$Li NMR of Si and a-SiO, ex situ $^{29}$Si NMR of a-SiO, electrochemical cycling) and Annica I. Freytag (ex situ $^{29}$Si NMR of Si, electrochemical cycling) at McMaster University. Data analysis and manuscript preparation were done by both ADP and AIF. Gillian R. Goward and Meng Jiang contributed to manuscript edits and data analysis.*

To meet the energy density requirement for our next-generation electric vehicle applications, new electrode materials with higher capacity are required. Silicon monoxide (a-SiO), a nano-scale mixture of Si and $SiO_2$, is one of the most promising anode materials because it can provide $1500\,\mathrm{mA\,h\,g^{-1}}$ specific capacity compared to $372\,\mathrm{mA\,h\,g^{-1}}$ for graphite and nevertheless overcome some of the inherent structural disadvantages of its parent material, silicon itself. The present work discusses the electrochemical reaction mechanisms of lithium insertion into a-SiO using multinuclear ssNMR. An in situ $^{7}$Li NMR study on both Si and a-SiO using a jelly-roll type battery design shows the intrinsic difference between the lithiation of those two materials. In addition, $^{29}$Si MAS NMR data obtained at 20 T provide sufficient sensitivity to acquire these spectra on electrode active materials, in spite of the low natural abundance of $^{29}$Si. Additionally, the electrochemical method developed here using porous cellulosic substrates provides a means to substantially enhance the amount of active material available for the NMR study of the cycled anode materials as a function of charge state. We demonstrate that this unorthodox cell design achieves reasonable capacity retention for the a-SiO anodes, and we suggest that this approach could be applied to a wide range of electrode materials.

## 3.1 Introduction

Extensive research effort has been dedicated to the investigation of silicon anode materials as a possible replacement to graphite.[1] The primary benefit to silicon based anode materials is the expanded gravimetric capacity, ranging as high as 3578 $\mathrm{mA\,h\,g^{-1}}$.[2] When compared to graphite at 372 $\mathrm{mA\,h\,g^{-1}}$ the increase in energy density associated with silicon is particularly attractive. However, the primary drawback of silicon anode materials is associated with the dramatic volume expansion (ca. 280 %) upon lithiation.[3] After multiple cycles the repeated volume expansion and contraction has been shown to pulverize the active material and result in separation of the silicon particles from the electrically conductive carbon matrix. Additionally, this physical instability disrupts the solid-electrolyte interphase (SEI) which forms at the surface of the silicon particles. In doing so, continued breakdown and loss of the electrolyte is promoted, thickening the SEI layer and resulting in an associated increase in electrical resistance along with depletion of the electrolyte components and loss of electrochemically-active lithium.[4]

The primary materials optimization approach towards enabling the use of silicon anodes is the mitigation and/or accommodation of the associated volume expansion using nanostructures, and mixed inert phases.[5] Many highly cited articles on silicon metal explain such approaches in greater detail.[6–8] Simultaneously, there has been substantial research into a detailed fundamental understanding of the electrochemical lithiation of silicon. Towards this end, in situ $^7$Li NMR has proven a valuable tool. For instance, a seminal publication by Key et al. revealed the formation of a metastable crystalline lithium silicide phase detected at the end of lithiation which dissipates upon discharge.[9] Such repeated transitions between amorphous and crystalline phases have been linked to excessive capacity fade.[10,11] Importantly, the crystalline phase, which is attributed to be the major cause of electrode breakdown, was unobserved in ex situ measurements, helping to underline the importance of in situ NMR in the observation of metastable states.

An alternative option for the anode is the use of a-SiO instead of pure silicon.[12] a-SiO is known to be a nano-scale mixture of Si and $SiO_2$, based on previous ssNMR studies of the pristine phase.[13] The primary advantage of a-SiO is the in situ electrochemical formation of a stable phase consisting of the irreversibly formed lithiation species including $Li_2O$ and $Li_4SiO_4$ which serve as a buffer to the volume expansion.[14] Moreover, the nano-sized electrochemically active Si particles are thought to absorb lithium without the pulverizing effect of the associated volume changes. The presence of $Li_2O$ and $Li_4SiO_4$ reduces the volume expansion upon lithiation by 50% in comparison to silicon.[12] Unfortunately, the enhanced cyclability necessarily incorporates additional irreversible capacity upon lithiation of the buffer species. Practical reversible anode capacities are about $1500\,\mathrm{mA\,h\,g^{-1}}$. Nevertheless, the potential for increased cycling stability coupled with a reversible capacity that is sufficient for current state-of-the-art transition metal cathodes makes them a promising anode candidate.

ssNMR studies of a-SiO electrode materials are sparse with only a handful having been reported to date.[15–17] While ex situ $^{7}$Li NMR of cycled active material have been published, no in situ experiments have been conducted thus far. Moreover, $^{29}$Si spectra of the charge/discharge process are known to be difficult to obtain due to the long relaxation times coupled with the low natural abundance, low gyromagnetic ratio, and small sample volumes associated with ex situ analysis of a-SiO anodes. Hirose et al. have studied structural changes of carbon-coated a-SiO anodes during lithiation and delithiation by using ex situ $^{29}$Si NMR.[17] However, they were not able to characterize the different lithium silicide species formed during cycling. This work addresses the shortcomings in current literature on a-SiO through the application of in situ $^{7}$Li NMR and ex situ $^{29}$Si MAS NMR at high magnetic field (20 T). We introduce a $^{7}$Li in situ methodology utilizing cellulose-based electrodes, which we use to compare the lithium insertion process in Si and a-SiO. In addition, detailed ex situ $^{29}$Si NMR of cycled anodes reveal specific features of the electrochemical process of a-SiO including the evolution of the $Li_4SiO_4$ buffer phase and provide insight on the nature of the lithium silicides formed upon lithiation, as compared to those reported in pure Si anodes.

To enable these experiments, we propose an unorthodox yet effective electrochemical strategy whereby the copper current collector is replaced with a porous cellulosic substrate. Cellulose-based materials have been investigated previously for their potential applications to lithium ion batteries,[18] such as binder[19,20] and separator.[21,22] Irrespective of the long-term implications, cellulosic substrates incorporate notable advantages towards NMR spectral acquisition of electrode materials. For ex situ experiments it can significantly increase active material loading per unit area of electrode. Typical active material loadings are in the range of $3\,\mathrm{mAh/cm^2}$ to $4\,\mathrm{mAh/cm^2}$,[23,24] whereas the a-SiO anodes used in this study maintained active material loadings of $7\,\mathrm{mAh/cm^2}$ to $10\,\mathrm{mAh/cm^2}$. This is achieved through the improved adhesion of electrode slurries using water-based binders onto the porous substrate. Similar loadings on traditional metallic substrates are more difficult to achieve without compromising structural integrity. The porous structure also enables the stacking of multiple electrodes in a single coin cell, where electrolyte can flow through the pores in the cellulosic substrates. While this reduces the effective cycling rate attainable by increasing ionic resistance, it dramatically increases the amount of active material per coin cell. For low sensitivity nuclei including $^{29}$Si the resultant signal boost can be particularly advantageous.

Increasing the sample size in this manner also has key benefits for the implementation of in situ $^{7}$Li NMR. Specifically, in situ NMR studies suffer from sensitivity issues related to both the broad resonances and the RF interference associated with the metallic current collectors. To minimize RF permeability effects, a horizontal geometry is typically employed. These cells are encased in a plastic, sealable bag inside of which the battery components are assembled and isolated from the outside environment. Copper and aluminum mesh current collectors are employed to allow RF penetration. The entire assembly is then surrounded by a solenoid coil which possesses enhanced sensitivity in comparison to the saddle coil used in vertical geometries.[25]

Various in situ studies conducted to date have utilized adaptations of the aforementioned design, from some of the very first studies of hard carbon anodes[26] to recent multinuclear studies on $LiFePO_4$ and $NaFePO_4$.[27] Both these and other in situ experiments have been highly successful in characterizing lithium ion batteries during operation, though RF permeability and active material loading remain common concerns. To this end a cylindrical geometry as enabled by the use of a cellulosic substrate is thus considered. This configuration provides an improved filling factor for the active material and retains use of the more efficient solenoid coil geometry. As mentioned with the ex situ experiments, the permeability of the cellulose electrodes allows multiple layers to be cycled simultaneously, albeit at the cost of a reduced cycling rate. Furthermore, the lack of a metallic current collector improves RF permeability.

The following results demonstrate that the use of cellulosic substrates as an anode material enables the acquisition of $^{7}$Li in situ and ex situ $^{29}$Si data while retaining significant cyclability at high active material loadings.

## 3.2 Experimental

The negative electrodes were prepared by mixing a-SiO powder (>99 %, 325 mesh, Sigma Aldrich) or Si powder (99.999 %, 325 mesh, Alfa Aesar) with Super-P C65 carbon black and sodium alginate binder (Sigma Aldrich, dissolved in deionized water) with 70/20/10 wt%. The prepared slurry was cast onto both sides of a 10 cm × 10 cm section of KimWipe®. The prepared electrode was then dried in air at 80 °C overnight and transferred into an argon filled

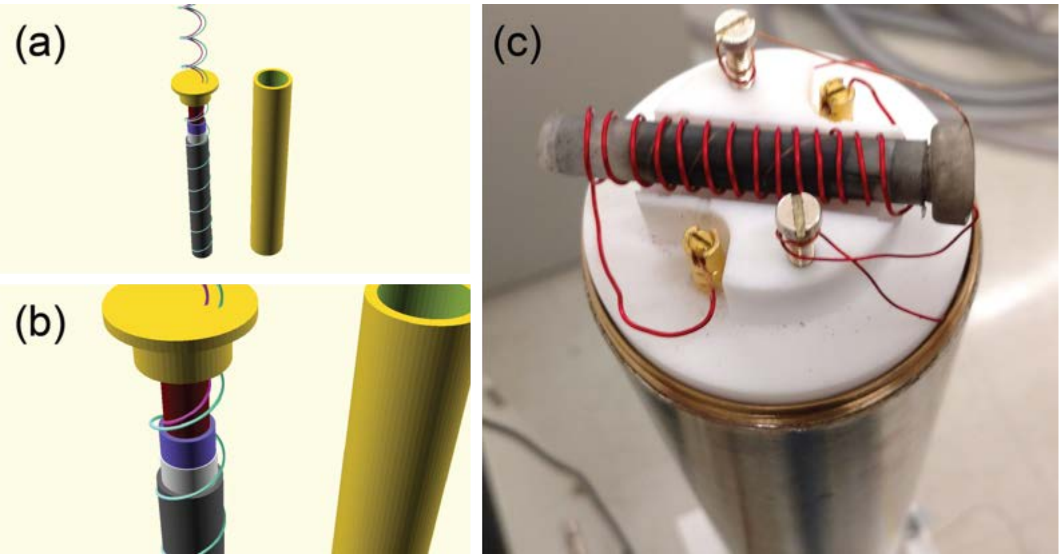

Figure 3.1: Schematic of in situ cell configuration showing (a) and (b) a close-up of the cell design. Current collector wires (magenta and cyan spirals), plastic core (red cylinder) and the lithium metal, separator, and cellulosic substrate anode (purple, white and grey cylinders, respectively) are enclosed in a plastic tube with a silicone rubber septum serving to isolate the battery chemistry from the environment while allowing electrical connection. (c) Top view of in situ cell sample mounting configuration on probe head including electrical connections, strain relieving metallic posts, and connections to probe base.

glovebox. The electrode loadings for the cellulose-based cells were 5-7 mg/cm$^2$ or 7-10 mAh/cm$^2$.

The in situ battery mimicked a jelly-roll type design as shown in Figure 3.1. For the assembly, a 3 ml syringe housing was modified by sealing the bottom by melting it together and removing approximately 1 cm of the syringe top. A silicone septum, acting as both holder for the current collector wires and top seal for the battery, was cut to 0.5 cm in length and pierced with two 16 cm lengths of copper wire, one of these being bare and the other being epoxy coated copper magnet wire. The epoxy coating of the magnet wire was removed both on the outside end and at a 6 cm section meant to go in the interior of the cell. The use of the coated wire was to prevent accidental short circuits as the assembly was placed in the modified syringe. As a support for the electrodes and wires, a 1 ml syringe plunger was cut to approximately 5 cm in length (the total length of the syringe housing was about 6 cm). The wide end was trimmed such that it fit inside the modified syringe thus centering the plastic core. The prepared magnet wire was then wrapped around the plastic core. The cell was transferred to the glove box and a rectangular section of flattened lithium foil (2.5 cm × 1.0 cm) and a section of separator with slightly larger dimensions were rolled around the plastic core and wrapped around the magnet wire. With the lithium and separator prepared, a 4 cm × 2 cm section of a-SiO or Si anode was wrapped around the prepared core and held in place with the bare copper wire. In an attempt to promote better contact with the separator, some sections of the anode were further wrapped with Teflon® tape. The entire assembly was placed loosely in the modified syringe, filled with 0.5 M lithium bis(fluorosulfonyl) imide (LiFSI) in EC/DEC, and sealed from the environment via the friction of the septum against the body of the syringe as shown in Figure 3.1.

Acquisition of the $^7$Li in situ NMR measurements necessitated additional considerations. The fully constructed cell was first attached to metal screws that were pre-drilled into the probe body. Their purpose was to relieve strain on the cell as the connections to the outside of the probe were being made. These connections were linked to the outside via two thin strands of magnet wire that fit in-between the probe body and the metallic sheath surrounding it. The circuit was completed through two 50 kHz RF filters on each channel. Furthermore, residual electronic noise was substantially reduced by grounding the BNC (Bayonet Neill-Concelman) cables to the body of the magnet.

NMR parameters involved a 13 $\mu$s $\pi/2$ pulse on a 200 MHz magnet with a recycle delay of 2 s. 1 M $LiCl_{(aq.)}$ was used as a reference. A cycling rate of C/50 was applied during in situ NMR measurements.

Coin cell construction involved the use of a Celgard® 2325 separator coupled with 100 µL of 1 M lithium hexafluorophosphate ($LiPF_6$) in EC/DEC (1:1 v/v) battery grade electrolyte solution (Sigma-Aldrich) and a lithium metal counter electrode (Chemetall Foote Corporation, High Purity Lithium Foil, ca. 1 mm thickness). Only a single punched a-SiO anode was used for the cycling stability studies, whereas two electrodes were used when preparing samples for ex situ $^{29}$Si NMR. Cycling rates were C/10 and C/50 for cycling stability and ex situ analysis, respectively.

NMR measurements of the ex situ cells were performed at several points in the charge/discharge process and involved $^{29}$Si magic-angle spinning (MAS) NMR experiments (23 kHz MAS rate, 850 MHz Bruker HD spectrometer, 3.2 mm double-resonance probe). Tris(trimethylsilyl)silane (TTMSS) was used as reference (-8.1 ppm relative to tetramethylsilane). A simple Hahn echo[28] pulse sequence was implemented (6 µs, $\pi/2$ pulse) with a recycle delay of 10 s for every sample. Each direct $^{29}$Si spectrum required approximately 1 day of acquisition on a fully filled rotor.

## 3.3 Results and Discussion

### 3.3.1 Electrochemical Performance of Cellulosic Electrodes

Due to the unconventional electrode preparation using a cellulosic material rather than a metallic foil as a substrate, the cyclability and capacity in a standard coin cell context was characterized. It is expected that the performance is inferior to conventional electrodes due to the decreased electrical conductivity of the cellulosic substrate compared to metallic current collectors. In addition, the a-SiO material used in this study is not designed for electrode application, therefore both the capacity and initial coulombic efficiency are presumed to be relatively low compared to battery grade materials, typically 1500 mAh/g and 70% respectively.[29] Along this vein, Figure 3.2 depicts the coulombic efficiency performance (a) and capacity (b) of the prepared a-SiO anodes. The first charge/discharge cycle reaches a reversible capacity of about 1250 mAh/g and a coulombic efficiency of 50%. The low first cycle efficiency is due to both initial SEI layer formation and the creation of irreversible lithium silicates and oxides.[30] However, the efficiency rapidly approaches 100% on subsequent cycles suggesting a stabilization of the irreversible reactions.

Given the rate of capacity decay it is likely that the sodium alginate binder is sufficient to keep the active material particles in initial contact with the carbon matrix. If there were a failure at this point the capacity would collapse to a fraction of its initial value within the first few cycles. It is probable that the observed capacity fade is a consequence of the continually thickening SEI layer often mentioned in literature where volume expansion has been tied to the generation of unexposed active material which further reacts with the electrolyte.[31,32] This process can serve to electrically isolate particles from the conductive carbon matrix. While the binder can provide adhesion to the conductive matrix, it cannot prevent the accumulation of SEI products over numerous cycles.

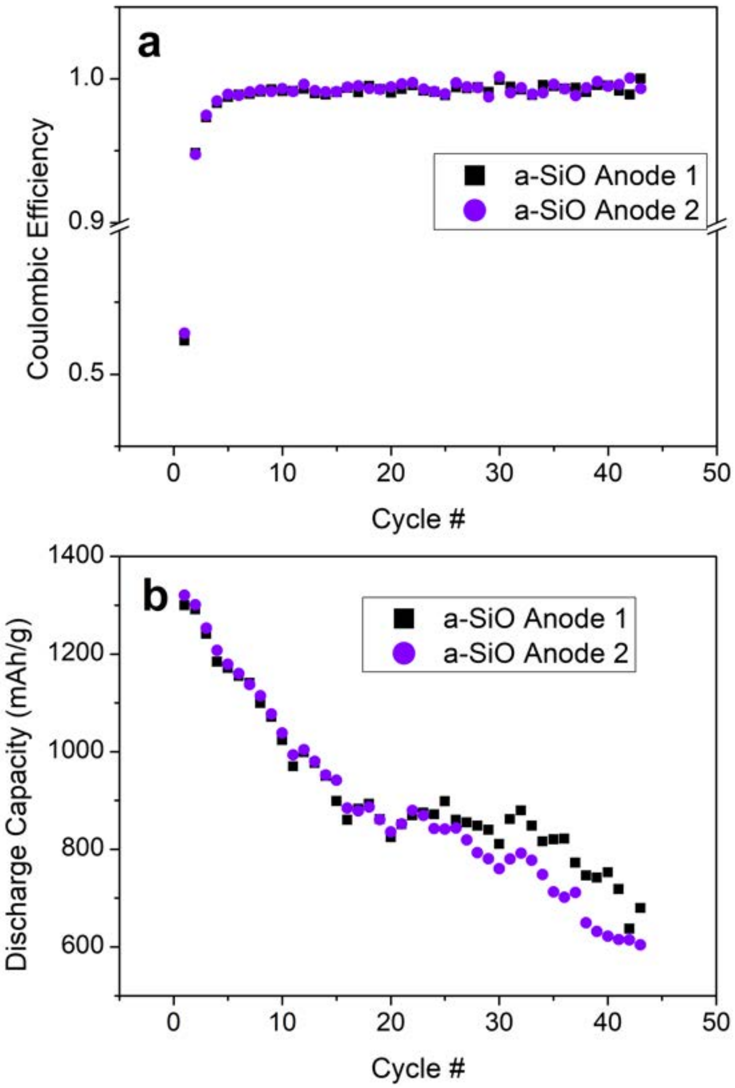

Figure 3.2: (a) Coulombic efficiency and (b) a-SiO capacity data over multiple cycles showing an associated variation in performance. An additional replicate is included to further verify the observed trend.

### 3.3.2 In Situ $^7$Li NMR Results

Figure 3.3 shows the in situ $^7$Li NMR results for the overall change in chemical shift across one full cycle for both silicon metal and a-SiO anodes. This overall picture shows an apparent similarity in initial cycling behavior as the lithium chemical shift increases upon lithiation. However, upon nearing

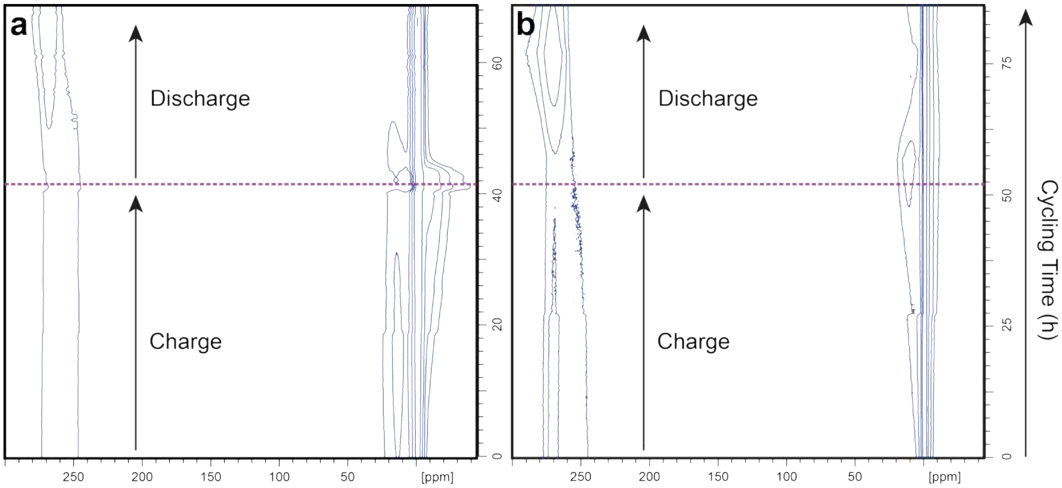

Figure 3.3: Comparison of $^{7}$Li in situ spectra detailing the change in the lithium chemical shift across a full discharge/charge cycle for (a) cellulose-based silicon metal anodes and (b) a-SiO. Purple line indicates end of charge and beginning of discharge.

the end of lithiation their behavior begins to deviate from each other. The silicon metal spectrum shows the development of a second peak at negative chemical shift values which corresponds to previous in situ studies suggesting the formation of phase 3 silicides.[9,33] In contrast, the formation of this same peak is not observed for the a-SiO anode. The amorphous to crystalline transition towards the end of lithiation is thought to be the major culprit for capacity fade in silicon anodes.[7] Fortunately, the absence of this signal during the in situ measurements suggests no such large scale transition and bodes well for the use of a-SiO as an anode material.

Figure 3.4 provides a more detailed description of the lithiation in both systems by showing snapshots of the beginning, middle and end of discharge and charge, respectively. Besides the absence of the resonance at -10 ppm for a-SiO, the chemical shift behavior of the initial lithiation peak differs. For silicon metal the average lithium silicide chemical shift appears at approximately 16

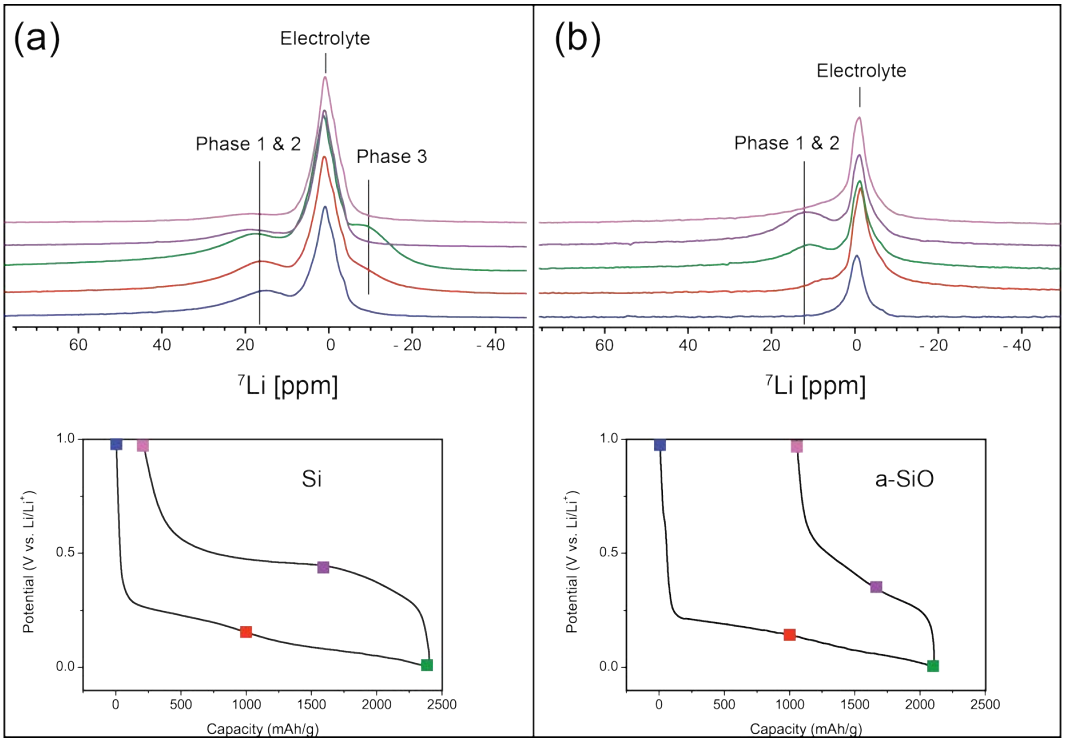

Figure 3.4: Comparison of $^7$Li in situ snapshots detailing a change in the lithium chemical shift during discharge (blue, orange, green), and charge (purple, pink) for cellulose-based silicon metal anodes (a) and a-SiO (b).

ppm and remains within ± 1 ppm until the appearance of the crystalline phase 3 at -10 ppm. a-SiO by contrast shows a chemical shift trend ranging from 4 to 11 ppm with increasing lithium content. Additionally, the appearance of a peak at -10 ppm is not observed. This behavior is consistent with previously performed ex situ $^7$Li NMR of these materials.[15,16] It is immediately clear that the electronic environments of lithium in the associated lithium silicide phases are not equivalent between the two anode materials. This might indicate that the expected metallic silicon domains are interspersed finely enough to result in a different lithium chemical shift trend.

### 3.3.3 Ex Situ $^{29}$Si MAS NMR Results

To support the findings from the in situ $^{7}$Li NMR experiments, ex situ $^{29}$Si MAS NMR spectra were collected along points on the first cycle charge/discharge curve of a-SiO as shown in Figure 3.5.

Figure 3.6 shows the high-field $^{29}$Si MAS NMR spectra collected for the lithiation of a-SiO anodes. Due to the amorphous nature of the a-SiO anode material, the chemical shift resolution is not impressive. Nevertheless, the sensitivity of these natural abundance $^{29}$Si spectra would be insufficient for data acquisition at more intermediate field strengths. For the pristine material, there exist two domains; one of which is associated with $SiO_2$ centered around -107 ppm and a second metallic silicon domain centered at -63 ppm.[16] Upon lithiation, the $SiO_2$ domain disappears immediately, and the Si domain is

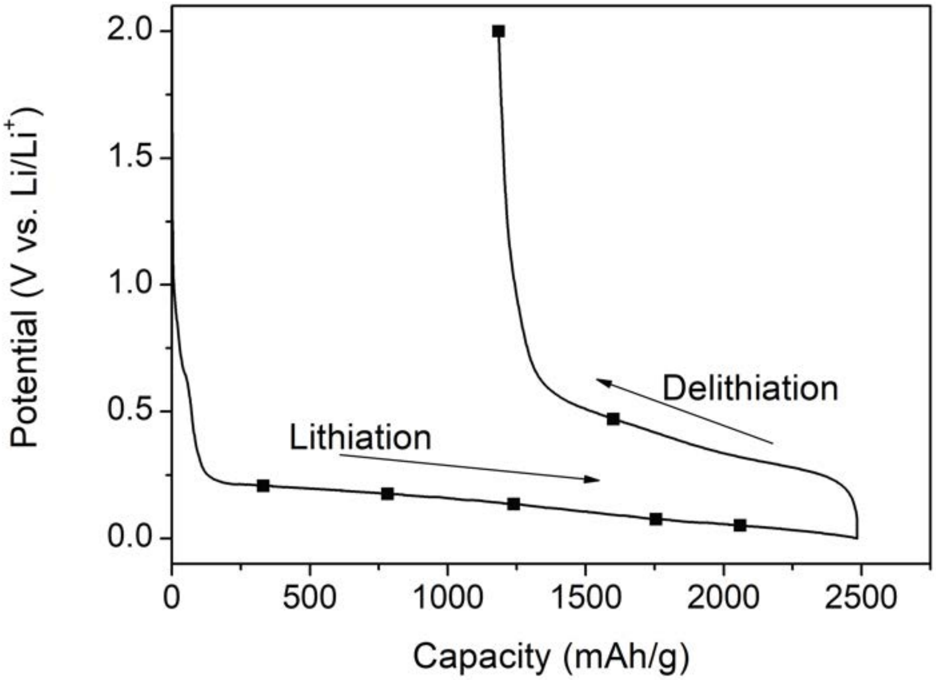

Figure 3.5: (a) Lithiation of a-SiO. The scattered points indicate the points on the curve used for $^{29}$Si NMR experiments.

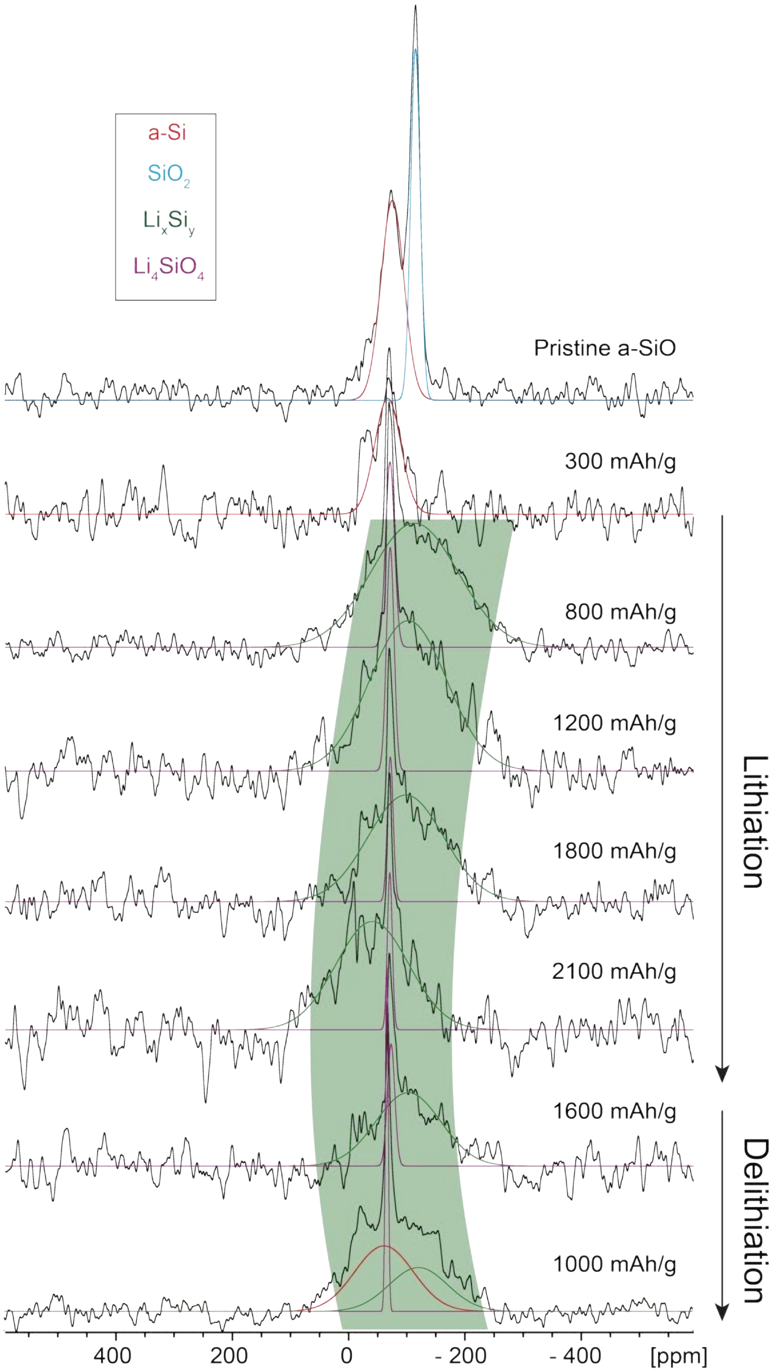

Figure 3.6: Ex situ $^{29}$Si MAS NMR spectra of pristine a-SiO and lithiated and delithiated states ranging from 300 to 2100 mAh/g and back to 1000 mAh/g. The MAS rate is 23 kHz, and the pulse delay is 10 s. Experiments were conducted at 20 T.

significantly reduced in intensity (300 mA h g$^{-1}$); subsequently, at 800 mA h g$^{-1}$, a new narrower peak is detected centered at -70 ppm. Additionally, a new much broader signal is detected, which is centered at -117 ppm at this degree of lithiation. This large broad peak grows in relative intensity as a function of increasing lithiation and shifts from -117 ppm initially, up to approximately -30 ppm by the end of lithiation, at which point this species dominates the spectrum. This trend is shown in Figure 3.7. Upon delithiation, the chemical shift of the broad resonance is reversed, moving to lower chemical shift values and decreasing in relative intensity. The non-Lorentzian line shape at 1000 mA h g$^{-1}$ (delithiation) indicates the existence of at least two different species. An amorphous silicon domain can be inferred, centered at -63 ppm and appearing upon delithiation consistent with the formation of amorphous silicon next to residual $Li_xSi_y$.

To put the chemical shift values in context it is relevant to consider the lithiation chemistry for both metallic silicon and a-SiO. In silicon itself, lithiation proceeds through several phases beginning with $Li_7Si_3$ corresponding to phase 1 and 2 silicides, ending with $Li_{15}Si_4$ (phase 3) and including several additional lithium silicide phases, $Li_xSi_y$, in between.[34,35] a-SiO is suspected to lithiate similarly within its metallic silicon domains. However, prior to the formation of silicides, initial lithium insertion will break the Si-O network to form a combination of $Li_4SiO_4$ and $Li_2O$ within the silicon dioxide domains. $^{29}$Si chemical shift data for lithium silicide in the bulk phases is available through a study on the enriched phases reported by Dupke et. al.[13] With the aid of isotopic enrichment, high quality $^{29}$Si MAS NMR data of both $Li_7Si_3$ and $Li_{13}Si_4$ were obtained. It is important to note that these pristine phases were prepared using a synthetic methodology as opposed to electrochemical

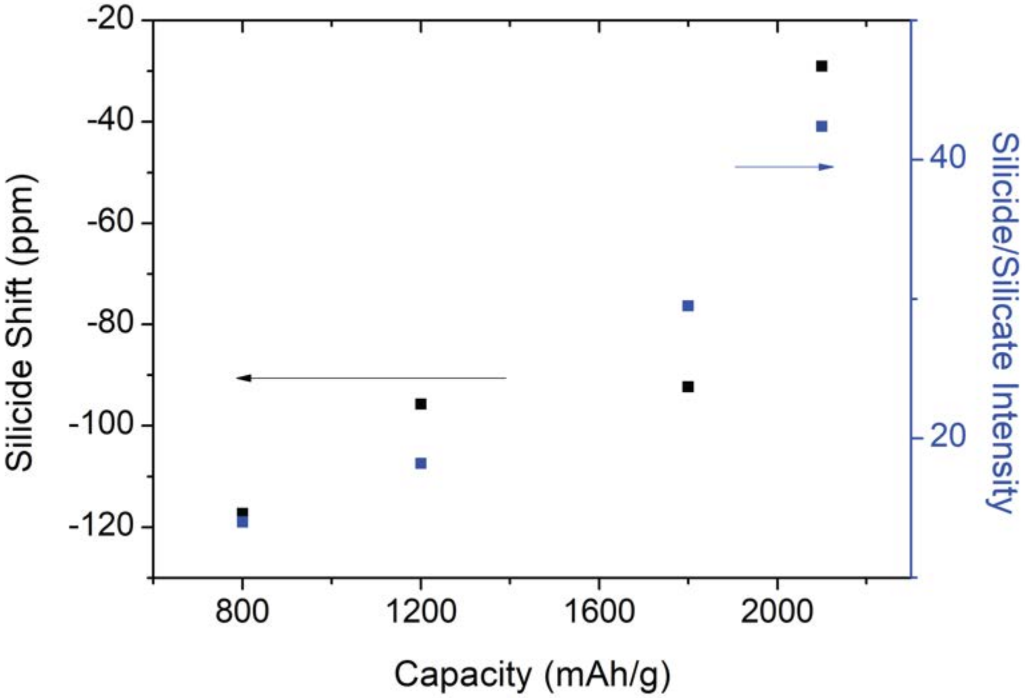

Figure 3.7: $^{29}$Si chemical shift of the broad lithium silicide resonance and silicide/silicate intensity changes as a function of lithiation capacity.

lithiation. Chemical shift values of these phases are 327 ppm for enriched $Li_7Si_3$ and 266 and 225 ppm for the two sites in enriched $Li_{13}Si_4$. Key et al. have shown that upon chemical lithiation of silicon, broad resonances centered at 72 ppm and 235 ppm appear, corresponding to lithium silicides.[9]

The result obtained by Dupke et al. and Key et al. contrast significantly with those obtained for a-SiO in this study. Some features can be readily explained such as the narrow resonance at -70 ppm which is consistent with a $Q_0$ silicon bonding environment expected for the $Li_4SiO_4$ irreversible lithiation product.[16] However, the broad resonance, which is believed to be attributed to reversible lithium silicide species, does not behave similarly to bulk metallic lithium silicides. The main silicon signal intensity is contained within the broad resonance with a linewidth in excess of 200 ppm. However, there is clear lack

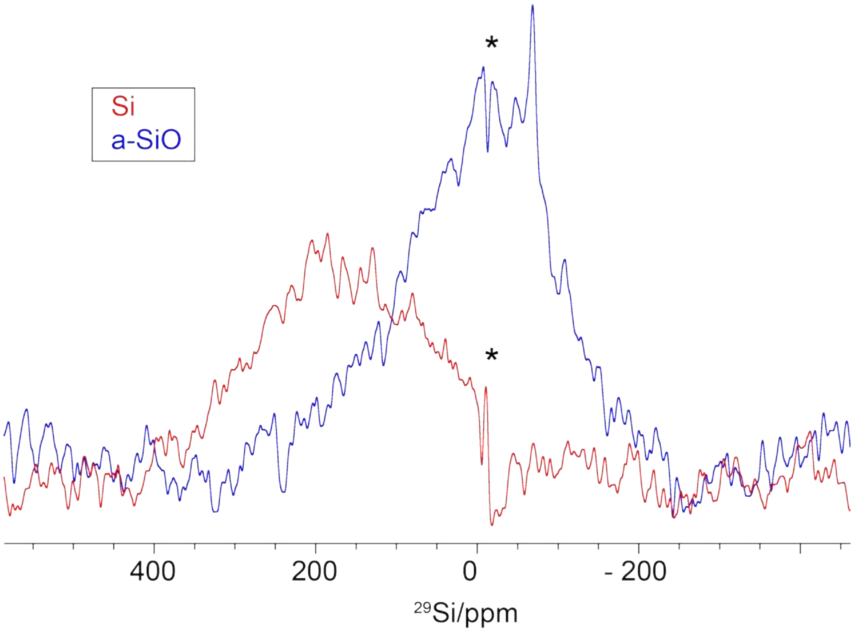

Figure 3.8: $^{29}$Si MAS NMR comparison of a fully lithiated Si (red) and a-SiO (blue) electrode. The asterisk denotes the probe background. Green deconvolution corresponds to lithium silicides, and purple deconvolution to $Li_4SiO_4$.

of an extensive Knight shift (which is typically observed in metallic material) where at no point throughout lithiation is this observed, although a moderate positive chemical shift trend is observed during this process (Figure 3.7). Our results suggest that the lithiated silicon domains within a-SiO have less metallic character than direct lithiation of pure silicon metal. In comparison, a fully lithiated cellulose-based Si electrode shows a broad resonance at 138 ppm in contrast with a fully lithiated a-SiO sample which shows a resonance centered at much lower frequency, at -29 ppm (see Figure 3.8). Width and chemical shift trend for the broad resonance in a-SiO are consistent with an interpretation as a collection of amorphous lithium silicides. This broad shifting resonance is therefore assigned to the $Li_xSi_y$ lithium silicides, and we conclude that individual silicide phases cannot be resolved even at this high field strength and spinning speed. This behaviour is consistent with the formation of nano-sized amorphous domains.

## 3.4 Conclusion

In summary, the lithiation of a-SiO shows some significant differences to the lithiation of pure Si. Clearly, as shown through in situ $^7$Li NMR, no crystalline phase 3 is apparent at the end of lithiation, which contrasts with the lithiation of Si, where phase 3 disrupts the structure in the high lithiation regime leading to long-term capacity loss. The $SiO_2$ domains in a-SiO break down initially to form irreversible lithium silicates and reversible lithium silicides as shown through $^{29}$Si MAS NMR. The Knight shift for the silicides formed from a-SiO is much less apparent than in bulk lithium silicides, supporting the hypothesis of the formation of less metallic nano-sized amorphous domains of $Li_xSi_y$ during lithiation. Upon delithiation the silicides revert back to an amorphous silicon structure.

In addition, this work demonstrates the utility of using porous cellulosic substrates in the context of lithium ion battery characterization via NMR. The large quantity of active material is important in enabling $^{29}$Si MAS NMR of the cycled anode materials as a function of charge state. Finally, the research presented here has proven the utility of a novel prototype design for the in situ NMR characterization of lithium ion batteries. Having confirmed the suitability of cellulosic substrates in at least the anode context, the increased filling factor and RF permeability of the design lend themselves well to future experiments. In Chapter 4 an adaptation of the herein described in situ cell is introduced, which allows for in situ MAS NMR studies.

# Bibliography

[1] Cheol-Min Park, Jae-Hun Kim, Hansu Kim, and Hun-Joon Sohn. Li-alloy based anode materials for Li secondary batteries. *Chemical Society Reviews*, 39(8):3115–3141, 2010.

[2] Wei-Jun Zhang. A review of the electrochemical performance of alloy anodes for lithium-ion batteries. *Journal of Power Sources*, 196(1):13–24, 2011.

[3] Shane D Beattie, Dominique Larcher, Mathieu Morcrette, Bernard Simon, and J-M Tarascon. Si electrodes for Li-ion batteries—a new way to look at an old problem. *Journal of The Electrochemical Society*, 155(2): A158–A163, 2008.

[4] Vinodkumar Etacheri, Ortal Haik, Yossi Goffer, Gregory A. Roberts, Ionel C. Stefan, Rainier Fasching, and Doron Aurbach. Effect of fluoroethylene carbonate (FEC) on the performance and surface chemistry of Si-nanowire Li-ion battery anodes. *Langmuir*, 28(1):965–976, 2011.

[5] Nian Liu, Hui Wu, Matthew T. McDowell, Yan Yao, Chongmin Wang, and Yi Cui. A yolk-shell design for stabilized and scalable Li-ion battery alloy anodes. *Nano Letters*, 12(6):3315–3321, 2012.

[6] Uday Kasavajjula, Chunsheng Wang, and A. John Appleby. Nano- and bulk-silicon-based insertion anodes for lithium-ion secondary cells. *Journal of Power Sources*, 163(2):1003–1039, 2007.

[7] Jeannine R Szczech and Song Jin. Nanostructured silicon for high capacity

lithium battery anodes. *Energy & Environmental Science*, 4(1):56–72, 2011.

[8] Hui Wu and Yi Cui. Designing nanostructured Si anodes for high energy lithium ion batteries. *Nano Today*, 7(5):414–429, 2012.

[9] Baris Key, Rangeet Bhattacharyya, Mathieu Morcrette, Vincent Seznec, Jean-Marie Tarascon, and Clare P Grey. Real-time NMR investigations of structural changes in silicon electrodes for lithium-ion batteries. *Journal of the American Chemical Society*, 131(26):9239–9249, 2009.

[10] MN Obrovac and Leif Christensen. Structural changes in silicon anodes during lithium insertion/extraction. *Electrochemical and Solid-State Letters*, 7(5):A93–A96, 2004.

[11] TD Hatchard and JR Dahn. In situ XRD and electrochemical study of the reaction of lithium with amorphous silicon. *Journal of The Electrochemical Society*, 151(6):A838–A842, 2004.

[12] Mariko Miyachi, Hironori Yamamoto, Hidemasa Kawai, Tomoyuki Ohta, and Masato Shirakata. Analysis of SiO anodes for lithium-ion batteries. *Journal of the Electrochemical Society*, 152(10):A2089–A2091, 2005.

[13] Sven Dupke, Thorsten Langer, Rainer Pöttgen, Martin Winter, Stefano Passerini, and Hellmut Eckert. Structural characterization of the lithium silicides $Li_{15}Si_4$, $Li_{13}Si_4$, and $Li_7Si_3$ using solid state NMR. *Physical Chemistry Chemical Physics*, 14(18):6496–6508, 2012.

[14] Yoon Hwa, Cheol-Min Park, and Hun-Joon Sohn. Modified SiO as a high

performance anode for Li-ion batteries. *Journal of Power Sources*, 222: 129–134, 2013.

[15] Jae-Hun Kim, Cheol-Min Park, Hansu Kim, Young-Jun Kim, and Hun-Joon Sohn. Electrochemical behavior of SiO anode for Li secondary batteries. *Journal of Electroanalytical Chemistry*, 661(1):245–249, 2011.

[16] Taeahn Kim, Sangjin Park, and Seung M Oh. Solid-state NMR and electrochemical dilatometry study on $Li^+$ uptake/extraction mechanism in SiO electrode. *Journal of The Electrochemical Society*, 154(12):A1112–A1117, 2007.

[17] Takakazu Hirose, Masanori Morishita, Hideya Yoshitake, and Tetsuo Sakai. Study of structural changes that occurred during charge/discharge of carbon-coated SiO anode by nuclear magnetic resonance. *Solid State Ionics*, 303:154–160, 2017.

[18] Thu H Nguyen, Arwa Fraiwan, and Seokheun Choi. Paper-based batteries: A review. *Biosensors and Bioelectronics*, 54:640–649, 2014.

[19] Lara Jabbour, Roberta Bongiovanni, Didier Chaussy, Claudio Gerbaldi, and Davide Beneventi. Cellulose-based Li-ion batteries: a review. *Cellulose*, 20(4):1523–1545, 2013.

[20] Jing Li, RB Lewis, and JR Dahn. Sodium carboxymethyl cellulose a potential binder for Si negative electrodes for Li-ion batteries. *Electrochemical and Solid-State Letters*, 10(2):A17–A20, 2007.

[21] Jianjun Zhang, Liping Yue, Qingshan Kong, Zhihong Liu, Xinhong Zhou, Chuanjian Zhang, Quan Xu, Bo Zhang, Guoliang Ding, Bingsheng Qin,

Yulong Duan, Qingfu Wang, Jianhua Yao, Guanglei Cui, and Liquan Chen. Sustainable, heat-resistant and flame-retardant cellulose-based composite separator for high-performance lithium ion battery. *Scientific Reports*, 4 (1), 2014.

[22] Zeming Song, Teng Ma, Rui Tang, Qian Cheng, Xu Wang, Deepakshyam Krishnaraju, Rahul Panat, Candace K Chan, Hongyu Yu, and Hanqing Jiang. Origami lithium-ion batteries. *Nature Communications*, 5(1):1–6, 2014.

[23] Li-Feng Cui, Yuan Yang, Ching-Mei Hsu, and Yi Cui. Carbon- silicon core- shell nanowires as high capacity electrode for lithium ion batteries. *Nano Letters*, 9(9):3370–3374, 2009.

[24] Hui Zhao, Yanbao Fu, Min Ling, Zhe Jia, Xiangyun Song, Zonghai Chen, Jun Lu, Khalil Amine, and Gao Liu. Conductive Polymer Binder-Enabled SiO–$Sn_xCo_yC_z$ Anode for High-Energy Lithium-Ion Batteries. *ACS Applied Materials & Interfaces*, 8(21):13373–13377, 2016.

[25] D.I Hoult and R.E Richards. The signal-to-noise ratio of the nuclear magnetic resonance experiment. *Journal of Magnetic Resonance (1969)*, 24(1):71–85, 1976.

[26] Michel Letellier, Frédéric Chevallier, Christian Clinard, Elzbieta Frackowiak, Jean-Noël Rouzaud, Francois Beguin, Mathieu Morcrette, and Jean-Marie Tarascon. The first in situ $^7$Li nuclear magnetic resonance study of lithium insertion in hard-carbon anode materials for Li-ion batteries. *The Journal of Chemical Physics*, 118(13):6038–6045, 2003.

[27] Oliver Pecher, Paul M Bayley, Hao Liu, Zigeng Liu, Nicole M Trease, and Clare P Grey. Automatic Tuning Matching Cycler (ATMC) in situ NMR spectroscopy as a novel approach for real-time investigations of Li-and Na-ion batteries. *Journal of Magnetic Resonance*, 265:200–209, 2016.

[28] E. L. Hahn. Spin Echoes. *Physical Review*, 80(4):580–594, 1950.

[29] Zhenda Lu, Nian Liu, Hyun-Wook Lee, Jie Zhao, Weiyang Li, Yuzhang Li, and Yi Cui. Nonfilling Carbon Coating of Porous Silicon Micrometer-Sized Particles for High-Performance Lithium Battery Anodes. *ACS Nano*, 9 (3):2540–2547, 2015.

[30] Sung Chul Jung, Hyung-Jin Kim, Jae-Hun Kim, and Young-Kyu Han. Atomic-Level Understanding toward a High-Capacity and High-Power Silicon Oxide (SiO) Material. *The Journal of Physical Chemistry C*, 120 (2):886–892, 2015.

[31] Qinglin Zhang, Xingcheng Xiao, Weidong Zhou, Yang-Tse Cheng, and Mark W Verbrugge. Toward high cycle efficiency of silicon-based negative electrodes by designing the solid electrolyte interphase. *Advanced Energy Materials*, 5(5), 2015.

[32] Juchuan Li, Nancy J Dudney, Jagjit Nanda, and Chengdu Liang. Artificial solid electrolyte interphase to address the electrochemical degradation of silicon electrodes. *ACS Applied Materials & Interfaces*, 6(13):10083–10088, 2014.

[33] Meng Gu, Zhiguo Wang, Justin G Connell, Daniel E Perea, Lincoln J Lauhon, Fei Gao, and Chongmin Wang. Electronic Origin for the Phase

Transition from Amorphous $Li_xSi$ to Crystalline $Li_{15}Si_4$. *ACS Nano*, 7(7): 6303–6309, 2013.

[34] H Okamoto. The Li-Si (lithium-silicon) system. *Journal of Phase Equilibria*, 11(3):306–312, 1990.

[35] Baris Key, Mathieu Morcrette, Jean-Marie Tarascon, and Clare P Grey. Pair distribution function analysis and solid state NMR studies of silicon electrodes for lithium ion batteries: understanding the (de)lithiation mechanisms. *Journal of the American Chemical Society*, 133(3):503–512, 2010.

## Chapter 4

# In Situ Magic-Angle Spinning $^{7}$Li NMR Analysis of a Full Electrochemical Lithium-Ion Battery Using a Jelly-Roll Cell Design

*The following chapter is adapted from a publication in the Journal of the American Chemical Society (J. Am. Chem. Soc. 2019, 141, 13758-13761). The technique development, data collection, data analysis and manuscript preparation was performed by Annica I. Freytag. Allen D. Pauric contributed to initial technique development. Gillian R. Goward and Sergey A. Krachkovskiy contributed to manuscript edits and final analysis. The study was performed at McMaster University.*

A new in situ magic-angle spinning (MAS) $^{7}$Li NMR strategy allowing for the observation of a full lithium-ion cell is introduced. Increased spectral resolution is achieved through a novel jelly-roll cell design, which allowed these studies to be performed for the first time under MAS conditions (MAS rate 10 kHz). The state of charge, metallic lithium plating and solid-electrolyte interphase (SEI) formation was captured for the first charge/discharge cycle of a full electrochemical cell ($LiCoO_2$/graphite). This strategy can be used to monitor both anode and cathode electrodes concurrently, which is valuable for tracking the lithium distribution in a full cell in real time and may also enable identification of causes of capacity loss that are not readily available from bulk electrochemical analyses, or other post-mortem strategies.

## 4.1 Introduction

Monitoring the state-of-health (SOH) of a lithium-ion battery is critical in improving its performance and understanding battery failure. In situ $^7$Li NMR has been demonstrated as an important strategy for elucidating the charge and discharge mechanisms of lithium-ion cells as it provides crucial information about phase changes, tracks electrolyte degradation and allows for the monitoring of lithium plating and dendrite formation in an electrochemical cell.[1–6] Primarily, these studies have focused on the investigation of only a single component of the battery at a time, e.g., anode, cathode or electrolyte. Letellier et al. implemented a static in situ NMR experiment using a plastic bag cell capable for the identification of electrochemical products in hard carbon and graphite.[3,7] They were able to clearly distinguish the different stages during lithiation and delithiation in carbonaceous materials. Similarly, Key et al. detected the metastable crystalline $Li_{15}Si_4$ phase (which plays a great role in electrode instability in silicon anodes) at the end of discharge in a silicon anode through an adaptation of a similar static pouch cell in situ NMR experiment. The metastable phase detected in this study is absent in ex situ experiments, highlighting the importance of performing in situ experiments.[4] In situ NMR studies of cathodes are particularly sparse as such materials produce much broader line shapes because of their paramagnetic nature and are therefore more difficult to probe.[5,8] However, the broadening associated with paramagnetic sites can be reduced through MAS. Shimoda et al. implemented an in situ cell capable of showing the charge/discharge behaviour of a $LiCoO_2$ cathode under static conditions, by cross-referencing the poorly resolved static line shapes (due to paramagnetic interactions) to datasets acquired using ex situ $^7Li$ MAS NMR.[9] Similarly, Salager et al. investigated the even more challenging paramagnetic $Li_2Ru_{1-y}Sn_yO_3$ cathode phase through a combination of ex situ and in situ NMR.[10] These studies demonstrate indirectly that it would be desirable to combine the strengths of MAS and in situ techniques in order to obtain a more accurate picture of the cycling behaviour of a full lithium-ion battery. The unique cell designed here is able to both cycle electrochemically, and subsequently acquire $^7Li$ NMR spectra under MAS conditions within a 4 mm rotor. This provides ample NMR resolution to track structural changes of all components of a graphite/$LiCoO_2$ full cell simultaneously.

However, designing such a cell comes with challenges. The most common geometries used for in situ NMR measurements to date are prismatic, pouch and coin cells as introduced in Chapter 2.6. All of these designs are limited to static measurements. In order to perform in situ methods under MAS conditions a variety of factors have to be optimized. The challenges for assembling an in situ battery like minimizing the amount of metallic components by using mesh-like current collectors to increase the penetration depth of the $\vec{B}_1$ field or optimization of the cell geometry become even more critical when it comes to designing a cell, which enables MAS. Not only do metallic components in the cell block RF pulses from penetrating through the cell, which leads to a substantial attenuation of the NMR signal, it also becomes increasingly difficult to spin a conductive metal inside a strong magnetic field as they can produce eddy currents, which in turn can cause spinning stability issues.[11] When it comes to designing an in situ MAS cell, it is therefore desired to minimize the amount of metallic components. In this study, this is achieved by utilizing charging wires made out of titanium as they are less conductive than the regularly used copper or aluminum current collectors. In addition, the active materials are cast on a cellulosic substrate as introduced in an earlier study.[12]

In terms of assembly of these types of cells, it is critical to follow a reproducible procedure, which was achieved by designing an assembly tool that allows for winding up the electrodes similar to how a cylindrical jelly-roll battery is assembled in an industrial setting. By winding the electrodes and separator around a support, the space inside the rotor can be used efficiently and increased contact between the active material and the separator was ensured. This geometry fits snug into a conventional MAS rotor. For the first prototype, a commercial 4 mm MAS rotor was chosen as the "battery casing" due to its filling factor and spinning speed limits. It is important to ensure that the amount of active material of both anode and cathode are sufficient to be detectable in a reasonable amount of time through static $^7$Li NMR. In addition, the applied spinning speed has to be fast enough to have a substantial effect on the resolution of the NMR spectrum.

## 4.2 Experimental

For the assembly of the in situ MAS cell, electrodes without a current collector support had to be prepared. This was achieved by preparing aqueous electrode slurries, which were then cast onto a cellulosic substrate (KimWipe™)

as introduced previously.[12] The $LiCoO_2$ (LCO) cathode was prepared with 80 wt% $LiCoO_2$ powder (LICO Technology Corp. L056), 10 wt% carbon black (Timcal, Super C 65) and 10 wt% carboxy(methyl) cellulose (CMC) binder (Sigma Aldrich, average Mw $\sim$ 90,000). 100 mg CMC binder was dissolved in 3 mL deionized (DI) water and sonicated for 30 min. 800 mg LCO and 100 mg carbon black were milled for 10 min and then added to the CMC/water mixture. The resulting slurry was then sonicated for an additional 30 min and cast onto the cellulosic substrate and dried in an oven at at 80 °C overnight. The graphite anode was prepared in a similar fashion using 100 mg CMC binder, 3 mL DI water, 100 mg carbon black and 800 mg graphite powder (Sigma Aldrich, powder, <20 µm). The other materials used for the assembly were Celgard® (2325) separator and titanium wire (Unkamen Supplies, 1/4 Hard, 32 gauge) current collectors.

The assembly of the cell was enabled by a custom-designed tool which consists of a dumbbell and a crank. These tools were designed using a computer-aided design (CAD) software (Autodesk Inventor). Figure 4.1 shows drawings of the designs.

In Figure 4.1 the crank tool is shown in yellow and purple. The yellow part acts as a support, which can be mounted onto a surface. The purple crank can be rotated along its axis, which in turn also rotates the grey dumbbell. The dumbbell is removable and Figure 4.1b shows a zoomed-in version of the design. The top square part fits snug into the purple crank, whereas the bottom cylindrical part is allowing for it to rotate when the crank is rotated. In addition, there are four integrated holes, which are used for inserting the current collector wires. Note, that there are two holes on each end, where one opposing pair is for the anode and the other one for the cathode connection.

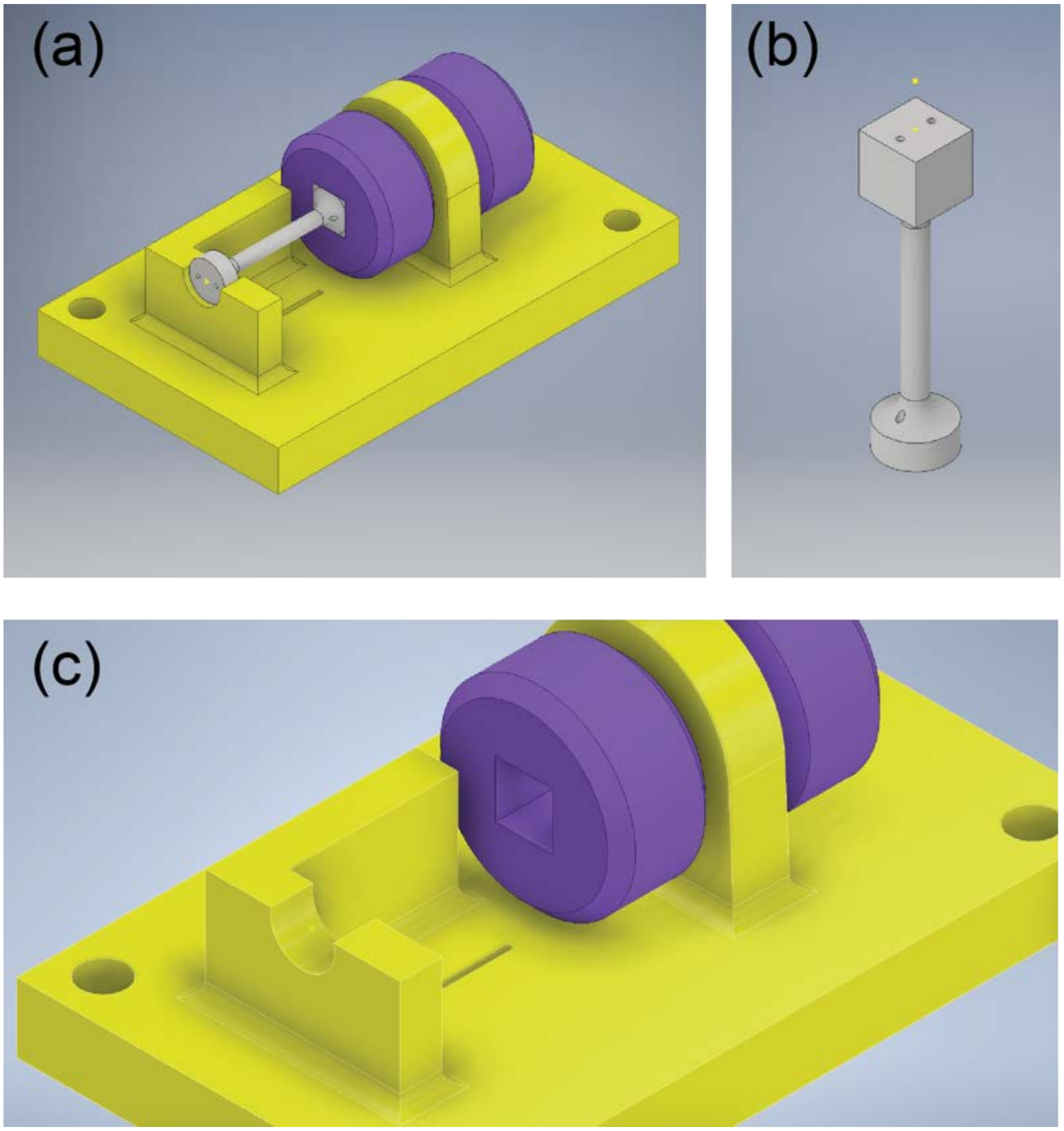

Figure 4.1: (a) Rotatable crank (purple) with a square notch to connect with the dumbbell shown in grey (b) 3D-printed dumbbell used in the assembly of the in situ MAS battery with current collector holes (c) Zoom on the rotatable crank without the dumbbell inserted into the square extrusion.

For the assembly of the in situ battery, the dumbbell is inserted into the square extrusion in the crank support (Figure 4.2a). The titanium wires are then thread through the holes in the dumbbell acting as the current collector for anode and cathode in addition to holding the separator and electrodes in

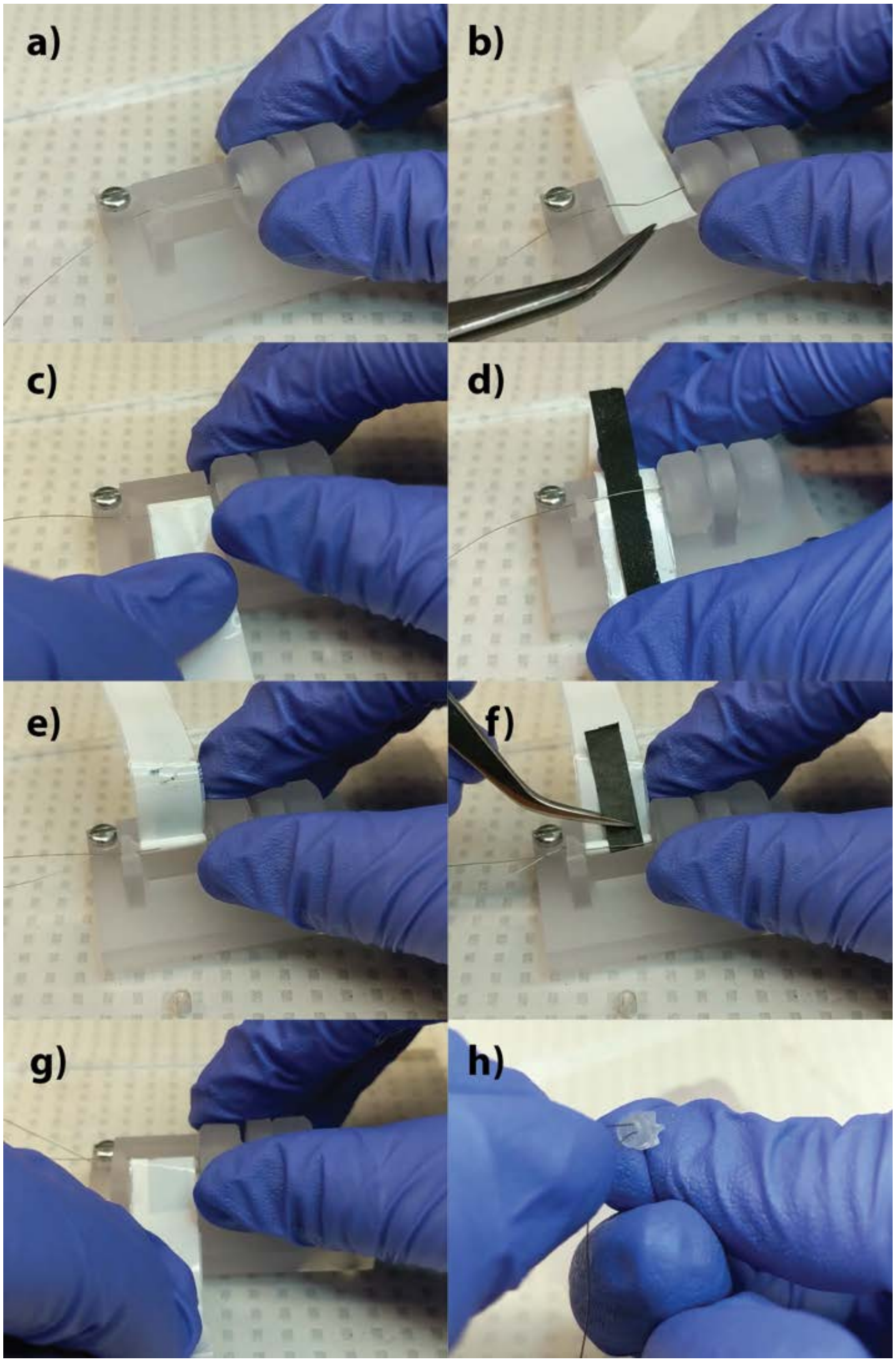

Figure 4.2: Snapshots of the assembly of an LCO/graphite in situ MAS battery.

place. The separator is inserted in between one of the titanium wires and the dumbbell in step (b) and secured by rotating it once around the dumbbell in (c). The LCO cellulose-based cathode (black rectangular sheet, 40 x 6 mm, active material loading 5.8 mg/cm$^2$) is then inserted between the separator and the titanium wire in step (d). Note, that the separator width is slightly bigger than the electrode width to ensure the electrodes are not touching. In step (e) both separator and cathode are moved upwards and the anode (grey rectangular sheet, 21 x 6 mm, active material loading 2.2 mg/cm$^2$) is inserted between the other titanium wire and the dumbbell support in step (f). Step (g) shows the winding of the material around the dumbbell. Slight pressure is applied by holding the bottom part of the separator, which allows for sufficient contact between the separator, electrodes and current collectors. The dumbbell is then removed from the resulting jelly-roll by cutting the top square part of the dumbbell and carefully removing all polymeric parts. The assembled cell was transferred to a 4 mm MAS rotor and the current collectors were thread through two holes in the rotor cap and then clipped using a clipping tool (Figure 4.2h). The holes in the rotor cap were drilled by hand using a Dremel® tool equipped with a stainless steel wire (diameter 0.3 mm). The rotor was then transferred to an argon glove box and filled with 1 M lithium hexafluorophosphate ($LiPF_6$) in ethylene carbonate/diethyl carbonate (1:1 v/v, EC/DEC) battery grade electrolyte solution (Sigma-Aldrich) through a third hole that was also drilled into the rotor cap. Charging of the cell was achieved through pressure contact by inserting two wires from the outside into the current collector holes. This was possible because the hole diameter of each hole in the cap was around 0.3 mm and the diameter of the titanium wire was around 0.2 mm.

Figure 4.3 shows an assembled battery and the charging setup. The cycling

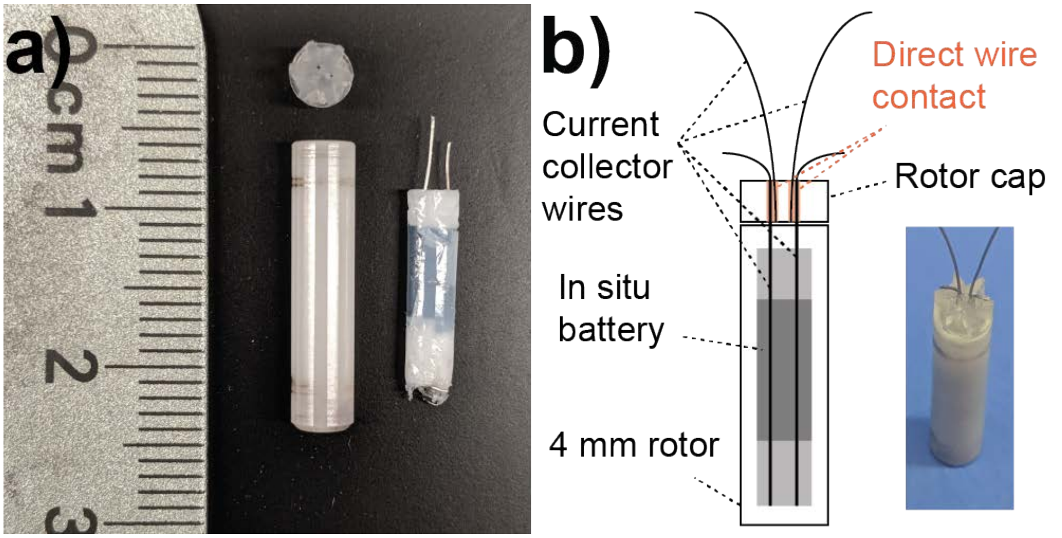

Figure 4.3: (a) commercial 4 mm rotor (left) assembled battery (right) and (b) charging setup

rate corresponds to C/100 under constant current conditions and was switched to constant voltage mode until the current reached 10% of its initial value at the desired point on the cycling curve. During charging/discharging the current collector wires form a direct contact connection with the wires inside the rotor. Once the cell was charged/discharged to the desired voltage it was disconnected from the wires and removed from the glove box. The cell was then inserted into the MAS probe and NMR experiments were carried out under a dry nitrogen gas flow. After each NMR measurement, the cell is transferred back into the glove box and refilled with approximately 10-20 µl 1 M $LiPF_6$ in EC/DEC due to solvent loss from spinning the sample before resuming charging. Transfer from the glove box to the spectrometer and vice versa took 5-10 minutes. The rotor was spun up in a spin tester to test stable spinning before being transferred into the probe and to avoid contamination of the NMR probe from solvent leakage.

NMR experiments were performed on a 7.05 T Bruker 300WB magnet using a

4 mm MAS probe. $^7$Li MAS spectra were collected using a single-pulse sequence with a $\pi/2$ pulse length of 3.5 µs. The recycle delay was set to 5 s for the single-pulse experiments and were collected at room temperature. In addition, magic-angle turning and phase-adjusted spinning sideband separation (MATPASS) experiments were performed in order to eliminate spectral interference of the spinning sidebands. MATPASS data was consulted to verify the isotropic peak assignment. The recycle delay was set to 0.1 s at a spinning speed of 10 kHz with a total accumulation of 1000 scans in the indirect dimension and 8 $t_1$ increments. The NMR data collection at each point in charge took approximately 30 min.

## 4.3 Challenges

Designing an in situ MAS battery does not come without challenges. In this section some of the failures and challenges, which had to be overcome, are discussed. This should give the reader an idea of the complexity of the successful experiments demonstrated in Section 4.4.

### 4.3.1 Electrode Balancing

Electrode balancing is a crucial step in optimizing the performance and long-term cyclability of LIBs.[13,14] In addition, it is important to understand the interplay between all components in a LIB in a full-cell format in order to minimize parasitic reactions, lithium inventory loss, and electrode degradation. Generally, for research purposes, electrode materials are assembled in a half-cell format using lithium metal as a counter electrode. This has advantages, e.g., lithium metal has a stable potential profile, which makes it a great reference electrode. Furthermore, an (almost) infinite amount of active lithium compared to a full-cell can be accessed during cycling making it more straight-forward to analyze the (de)lithiation process of the electrode of interest. However, half-cell assemblies lack in properly representing the interactions between the individual components as a whole. Careful manipulation of anode/cathode ratio, electrolyte (additives), binder chemistry, etc. is required to build a long-lasting (full-cell) battery.

In full-cells, contrary to half-cells, the source of active lithium is limited. Full-cells are assembled in the discharged state meaning that the cathode holds all the active lithium. The reversible specific capacities of both electrode materials have to balanced in order to avoid overcharge and lithium plating inside the cell. This is achieved by first cycling the electrodes in a half-cell separate from each other to determine their respective reversible capacities. The mass of active material then needs to be balanced according to

$$Q_{\text{discharge}} = q_{\text{negative}} \cdot m_{\text{negative}} = q_{\text{positive}} \cdot m_{\text{positive}} \tag{4.1}$$

where $Q_{\text{discharge}}$ is the discharge capacity (in mAh), $q$ the reversible specific capacity of either the negative (N) or positive electrode (P) with the corresponding active mass $m_{\text{negative/positive}}$.

Figure 4.4 shows examples for varying specific capacity ratios of N:P. It is evident that at ratios below one the anode potential profile reaches voltages below the safe limit and lithium plating occurs (purple line). On the other hand, if ratios are higher than one, the cathode potential profile exceeds the upper voltage limit where electrolyte and cathode degradation may take place (blue line). In theory, when N:P equals one, the potential profiles remain in

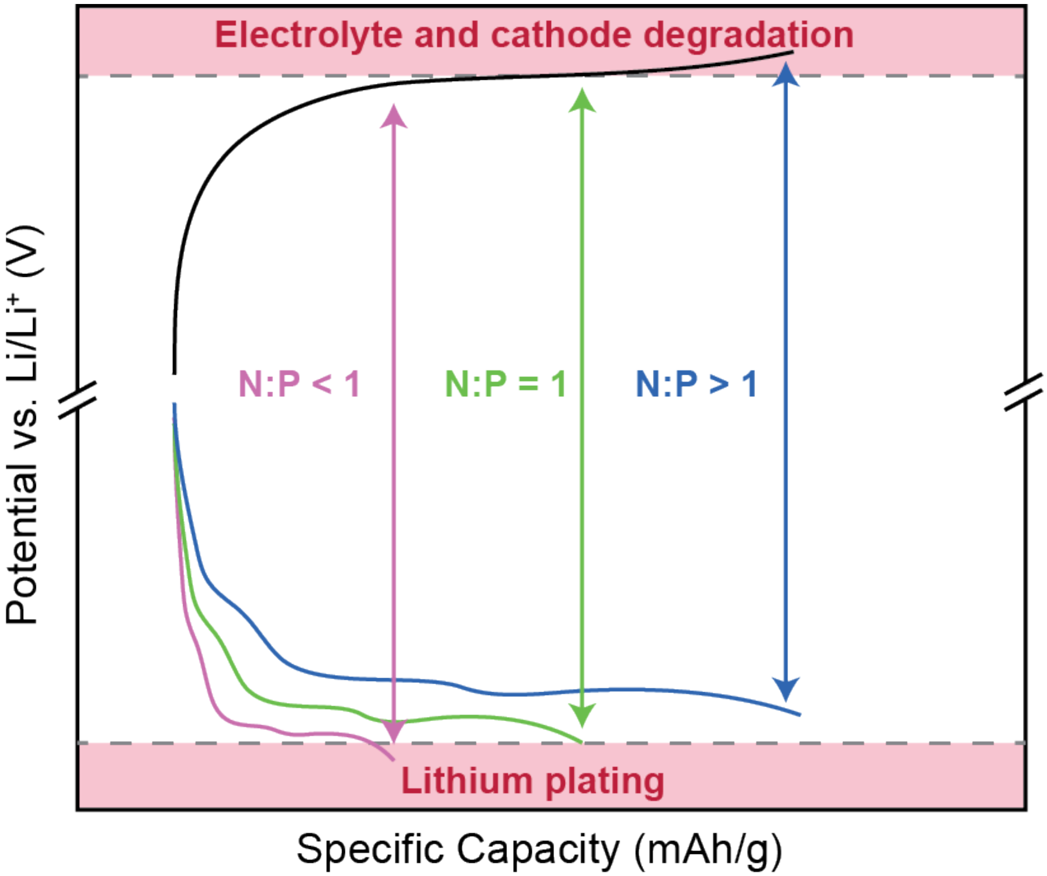

Figure 4.4: Voltage profiles of anode and cathode in a full-cell with varying N:P reversible capacity ratios, where N and P are graphite and $LiCoO_2$, respectively. Adapted from Reference[14].

the safe voltage window on both anode and cathode side (green line). However, in practice, the N:P reversible specific capacity ratio has to be slightly higher than one to ensure safe operation of the cell. This is due to the decrease of the specific capacity with each cycle (especially on the anode side) because of the formation of irreversible capacity due to electrolyte degradation, formation of the SEI and other possible side reactions. With increased cycling the amount of active material that can be accessed may decrease leading to a shift of the potential curves to lower values. For example, in silicon anodes, the SEI is of dynamic nature and may accumulate with each cycle and therefore changes the N:P reversible specific capacity ratio over time. As an extreme it could go from a safe N:P ratio of one during the first cycle to a value below one after a few cycle due to a steady increase of irreversible SEI products, which can lead to lithium plating on the anode. In order to obtain a more accurate picture of the failure mechanisms in LIBs, it is of paramount importance to understand the interplay between all components of the cell.

Charge balancing is a critical step in battery design and in particular for this type of in situ cell. Most in situ NMR experiments to date have been performed on half-cells containing metallic lithium as a counter electrode. However, in a full cell such as the one utilized here, the amount of active lithium is significantly less and the formation of the SEI on graphite removes a considerable amount of active lithium during the first cycle due to the use of cellulosic electrodes. In industry, electrode balancing is achieved through careful engineering of the cell design and fine adjustment of electrode loadings. However, in this study perfect balancing is difficult to achieve due to the non-uniform distribution of active material and pressure differences throughout the sample.

In order to obtain the correct balancing ratio according to Equation 4.1, the cellulose-based electrodes were cycled in a half-cell format against lithium metal to estimate the experimental capacity and the amount of irreversible capacity formed during the first cycle. Figure 4.5 shows the formation cycle of both graphite and LCO in a coin cell format. The graphite electrode exhibits a large irreversible capacity during the first cycle (around 30%) and low coulombic efficiency (around 0.6) which can be attributed to the free-standing electrode material used in this study. In comparison to a standard electrode, this substrate promotes a larger amount of SEI formation due to its porous structure. It is important to take this into account when balancing the electrodes. The

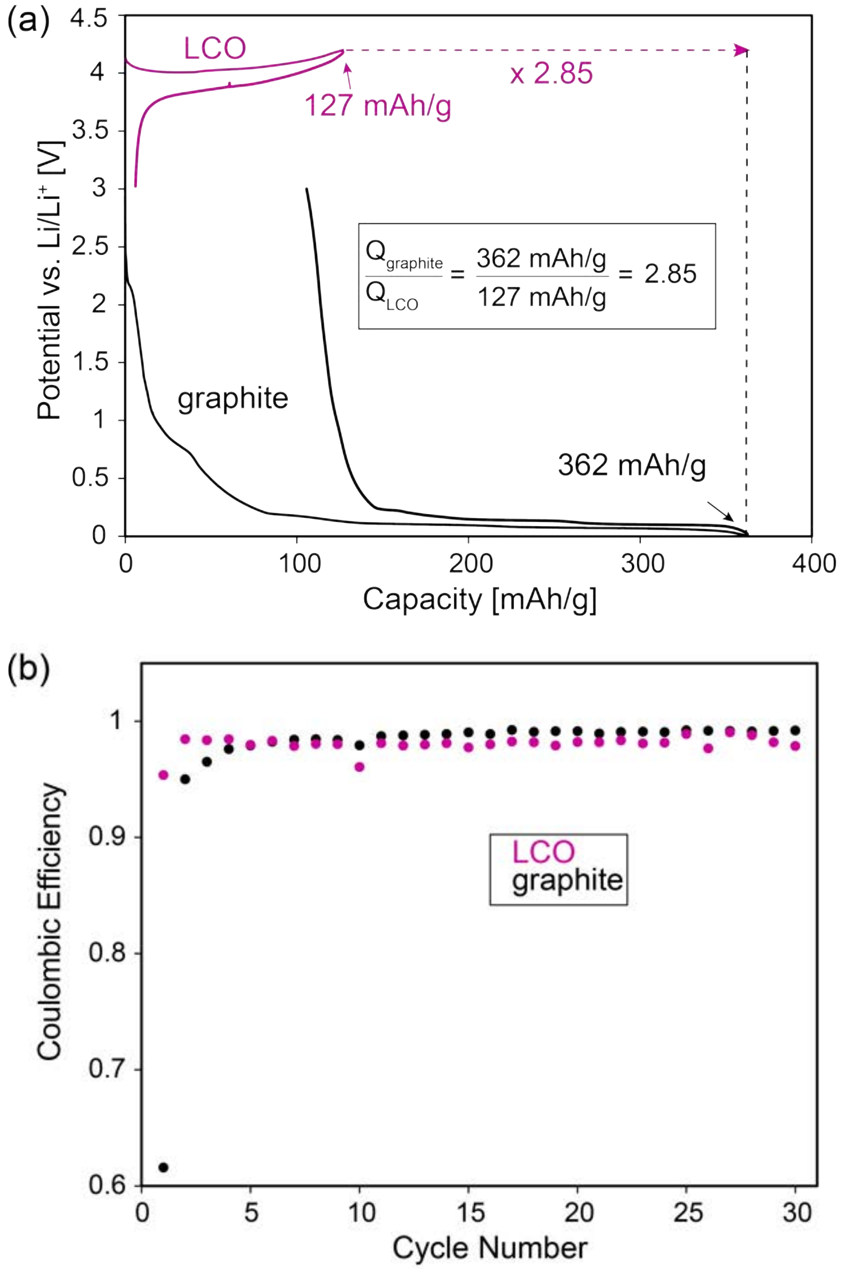

Figure 4.5: (a) Charge potential profile of cellulose-based LCO (purple) and graphite (black) electrodes measured in a half-cell format against Li metal. To balance the electrodes, the LCO specific capacity ($Q_{LCO}$) needs to be increased by a factor of 2.85. (b) Coulombic efficiency for LCO (purple) and graphite (black) for the first 30 cycles; graphite: 0.0005-3.000 V, specific current 74 mA/g; LCO: 3.0-4.2 V, specific current 27 mA/g

theoretical and experimental capacities for the graphite and LCO coin cells are summarized in Table 4.1.

| Electrode Material | Theoretical Capacity (mAh/g) | Reversible Capacity (mAh/g) | Irreversible Capacity (mAh/g) |
|---|---|---|---|
| Graphite | 372 | 257 | 105 |
| $LiCoO_2$ | 274 (137) | 121 | 6 |

Table 4.1: Theoretical and experimental capacities for the graphite and LCO coin cells shown in Figure 4.5. LCO suffers from lattice distortion when x<0.5 for $Li_xCoO_2$, which allows for only half ($137\,\mathrm{mA\,h\,g^{-1}}$) of the theoretical capacity to be accessible.

From the coin cell cycling data in Figure 4.5, it is estimated that the specific capacity of LCO has to be increased by a factor of 2.85 in order to be balanced against the graphite electrode. However, during in situ charging it is expected that due to repeated refilling and spinning of the in situ cell, a larger amount of SEI forms on the graphite electrode. This is why a large excess of LCO was used for the in situ cell assembly. The active mass ratio for the below discussed in situ cell corresponds to $m_{LCO}/m_{graphite} = 5$, which ensures full lithiation of the graphite electrode.

### 4.3.2 Solvent Leakage

One of the greatest issues with the design of this in situ MAS cell concerns solvent leakage. Initially, the dumbbell structure was not only used to help in the assembly of the cell but was meant to aid in structural stability during MAS. However, electrochemical cycling of these in situ MAS cells with the dumbbell support showed large discrepancies between cells. Figure 4.6a shows an example

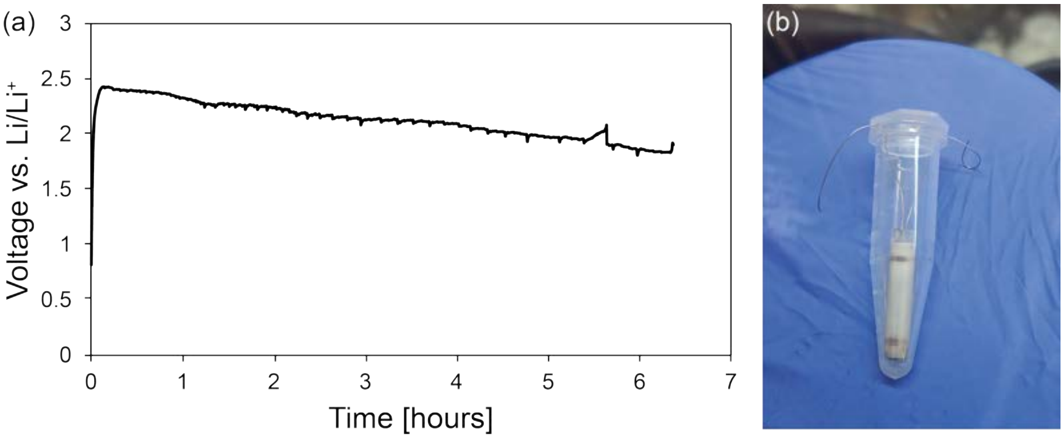

Figure 4.6: (a) Electrochemical cycling curve for an in situ MAS battery cycled with a polymeric support. The current applied corresponded to 115 µA. (b) Charging setup for successful cycling of the in situ MAS cell.

of a charging curve for an in situ cell where the battery was wrapped around the polymeric support. The cell does not reach potentials past around 2.5 V. This is due to the electrolyte solvent either evaporating during charging, or due to the polymeric support soaking up the solvent leading to a disconnected conductive network. Changes to the design helped minimize the severe solvent loss, which included (1) removal of the dumbbell before transferring the cell to the rotor (as illustrated in Figure 4.3a) (2) drilling of a third hole which made it possible to fill the rotor with electrolyte without removing the rotor cap and (3) by inserting the rotor into a small plastic vial with a flip cap during cycling (Figure 4.6b), which minimized the exposure to the surrounding argon atmosphere inside the glove box.

### 4.3.3 Spinning Stability

In order to achieve stable spinning during the MAS experiments, the rotor was tested inside a spinning tester before every MAS NMR measurement. In general, the spinning of the rotor was successful up to 10 kHz. However, several factors had to be considered. The battery had to be pushed to the bottom of the rotor, so that the weight was distributed properly. It can be seen in Figure 4.3a, that the battery is slightly shorter than the length of the rotor. When the battery was centered in the middle of the rotor, spinning stability issues occured. In addition, it is more difficult to spin a dry cell (when no liquid electrolyte was added to the rotor), most likely because the weight distribution inside the rotor was top-heavy due to the current collector wires sticking out the top of the rotor.

Furthermore, spin testing leads to evaporation and leakage of solvent through the rotor cap holes. This is due to the strong centrifugal force that is applied to the rotor under MAS and because of the heat that is generated throughout the process. It is not desired to have the solvent leak out of the cell inside the MAS NMR probe, which could lead to serious damage of the delicate MAS stator. To circumvent this issue, the in situ MAS cell was first spun in the spin tester before being inserted into the NMR probe. In addition, the cell was replenished with electrolyte after collecting an NMR spectrum so that subsequent cycling was not hindered due to a dry cell.

## 4.4 Result and Discussion

In order to ensure that the electrochemical performance of the jelly-roll cell is adequate, the first charge/discharge cycle was monitored. Figure 4.7a shows the cycling curve of an LCO/graphite jelly-roll in situ MAS cell. Low charging currents (C/100) had to be applied to ensure that the electrodes charge and discharge uniformly as a thin titanium wire was used as a current collector instead of copper/aluminum foil. A significant amount of irreversible capacity (as much as 35%) accumulates during the first cycle. This is attributed to the formation of the SEI, as well as plated lithium metal. $^7$Li NMR spectra were collected at the indicated points on the curve in Figure 4.7a. Figure 4.7b and 4.7c show a contour and stacked plot of the $^7$Li NMR data collected under MAS conditions (MAS rate 10 kHz) for the first charge/discharge cycle, respectively. Both anode and cathode species are well-resolved in addition to a remarkable signal to noise owing to the significant increase in the amount of active material used within this in situ cell design.

The region around 0 ppm corresponds to pristine $LiCoO_2$, $LiPF_6$ electrolyte and SEI products. During charge, $LiCoO_2$ (at 0 ppm, pristine) is delithiated to $Li_xCoO_2$ (x<1), resulting in a Knight-shifted $^7$Li NMR signal at around 10 ppm at 3.0 V during the charging process denoted as $C_{3.0V}$ (C — charge) showing a steady increase to around 100 ppm ($C_{4.0V}$) on charge. A small decrease in chemical shift and intensity is seen at the top of charge ($C_{4.1V}$) indicating a delithiation past $x = 0.5$ in $Li_xCoO_2$. This behaviour has been observed previously in ex situ experiments and is attributed to the change of the interlayer distance of the c lattice parameter of $Li_xCoO_2$.[5] It is notable that such a small change in chemical shift (on the order of 2 ppm) would not be resolvable in the static in situ experiments.

On the anode side, lithium-ions are intercalated in between the graphene sheets on charge. The formation of the dilute ($LiC_{36}$ to $LiC_{18}$) and concentrated ($LiC_{12}$ and $LiC_6$) graphite stages can be readily observed through tracking the well-resolved $^7$Li NMR signals.

The lithiation of graphite and their respective $^7$Li NMR signature has been discussed previously.[3,6] Figure 4.7b and 4.7c reveal the appearance of dilute

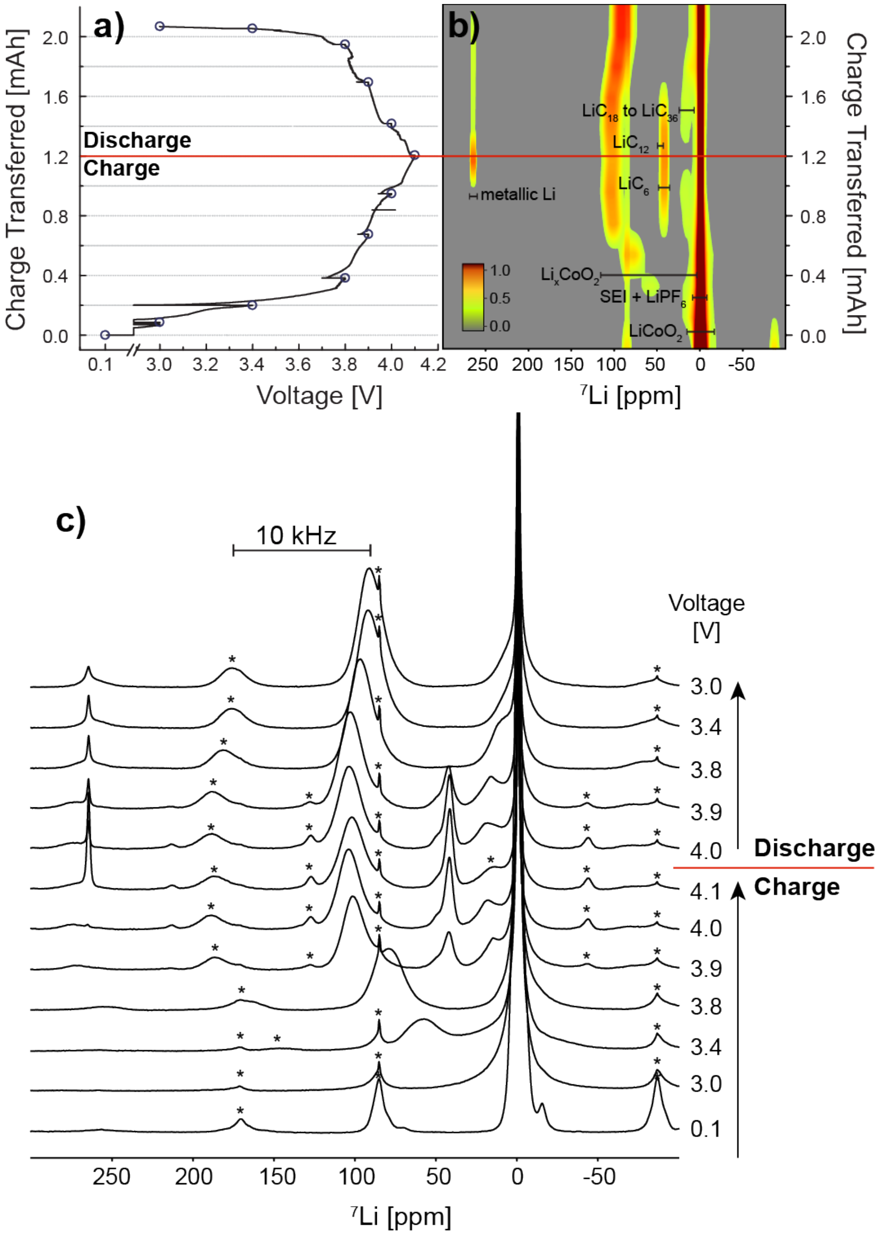

Figure 4.7: (a) Charging profile of the electrochemical cell used for $^7$Li MAS NMR analysis. Circles denote the points used for NMR measurement. Cycling rate corresponds to C/100 under constant current/constant voltage conditions until current reached 10% of its initial value. (b) Contour and (c) Stacked plot single-pulse $^7$Li MAS NMR spectra acquired for the first cycle of $LiCoO_2$/graphite cell, MAS rate 10 kHz. (pulse delay 5 s). Asterisks indicate spinning sidebands.

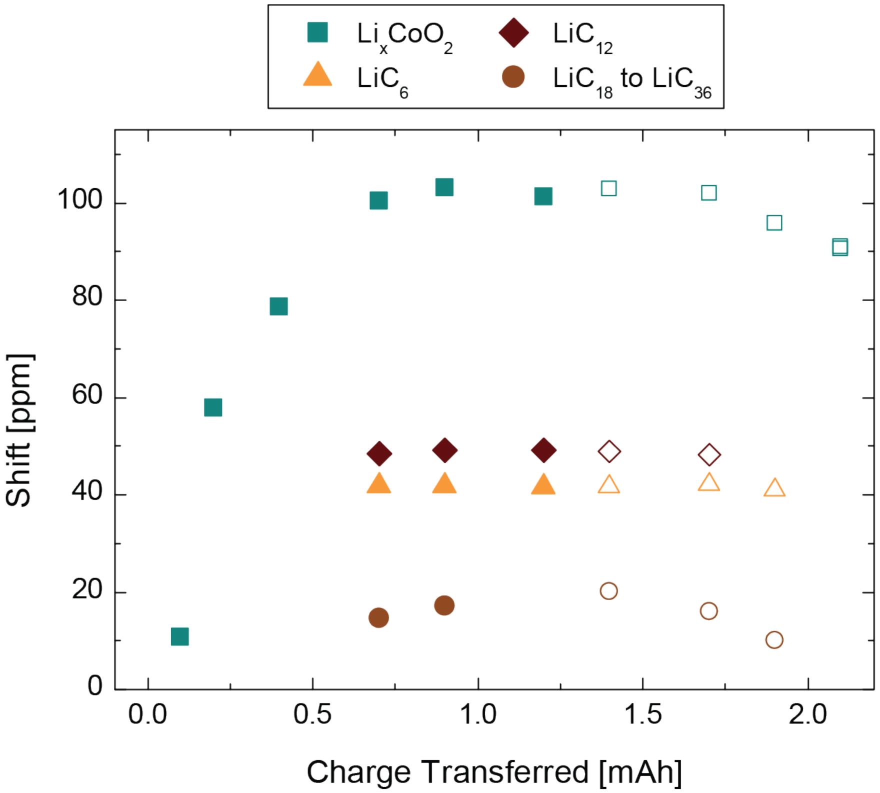

Figure 4.8: NMR shifts extracted from peak deconvolution of single-pulse $^7$Li NMR MAS spectra. Filled and empty symbols denote shifts during charge and discharge, respectively.

stages between 10-20 ppm at the beginning of the charge plateau ($C_{3.9V}$ to $C_{4.0V}$) alongside the concentrated stages ($^7$Li NMR shift $LiC_{12}$: 49 ppm, $LiC_6$: 42 ppm). On further lithiation, the concentrated stages start to dominate the dilute stages until, at the top of charge, all dilute species are transformed to $LiC_{12}$ and $LiC_6$. Figure 4.8 summarizes the shift values for the $Li_xCoO_2$ phase and the dilute and concentrated graphite stages.

The absence of any dilute graphite stages around 20 ppm at $C_{4.1V}$ is difficult to observe in Figure 4.7c due to the overlap with the spinning side bands of $Li_xCoO_2$. MATPASS spectra were collected to confirm their absence at $C_{4.1V}$, as shown in Figure 4.9. MATPASS is a rotor-synchronized pulse sequence as introduced in Chapter 2.4.1, which separates the isotropic and anisotropic contributions of solids with line widths greater than the applied MAS frequency. It has been used in studies of Li-rich battery materials in order to get an uncluttered spectrum without peak overlap.[15,16] Pulse-sequence based strategies for selecting specific interaction and enhancing spectral resolution are significantly enhanced with the availability of this MAS-based in situ methodology. On discharge, the concentrated graphite stages steadily decrease in intensity as they revert to the dilute stages mirroring the charge process. As discharge progresses below $D_{3.8V}$ (D — discharge), graphite is completely delithiated and therefore no longer observable through $^7$Li NMR. In addition, it is notable in Figure 4.9, that on discharge $Li_xCoO_2$ levels off at around 90 ppm ($D_{3.0V}$) instead of reverting to 0 ppm ($Li_xCoO_2$ with x=1).

The loss of active material is attributed to the irreversible lithium species formed during charge, which is consistent with the electrochemical data in Figure 4.7a showing an accumulation of irreversible capacity. However, it is not possible to distinguish between SEI formation and irreversible lithium plating from the electrochemical data alone. In contrast, the $^7$Li in situ NMR data shows clearly that metallic lithium is formed at the top of charge corresponding to a $^7$Li signal at 264 ppm ($C_{4.1V}$) which only partially disappears on discharge indicating that graphite was lithiated past 0 V causing lithium plating. In an electrochemical experiment this formation could only be tracked with the use of a reference electrode. The accumulation of irreversible lithium on the electrode surface in a full cell can, however, be tracked non-invasively through the technique developed here. Irreversible lithium plating on the electrode surface can have tremendous effects for the long-term performance of the cell and is an indicator for possible battery failure.

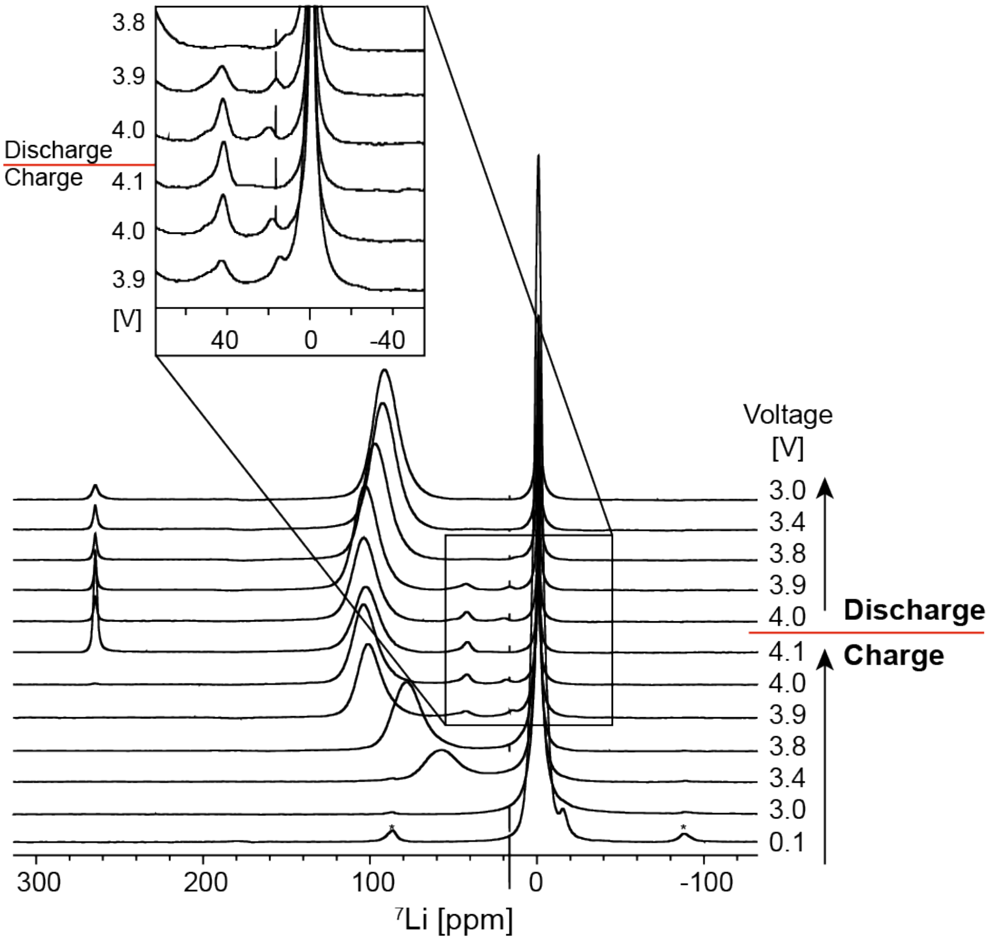

Figure 4.9: MATPASS data for the first electrochemical cycle (recycle delay 0.1 s)

Figure 4.10a and b show the deconvolution of $^7$Li solid-state NMR spectra for the fully charged cell under spinning and static (MAS 10 kHz) conditions, respectively. The delithiated $Li_xCoO_2$ and lithiated graphite species are clearly resolved in the MAS spectrum. In addition, metallic lithium, electrolyte ($LiPF_6$) and SEI products are visible. It is apparent that fitting the static data set is challenging and no clear distinction between the different species can be made due to overlapping of the peaks.

Deconvolution data of all species for the first charge/ discharge cycle is

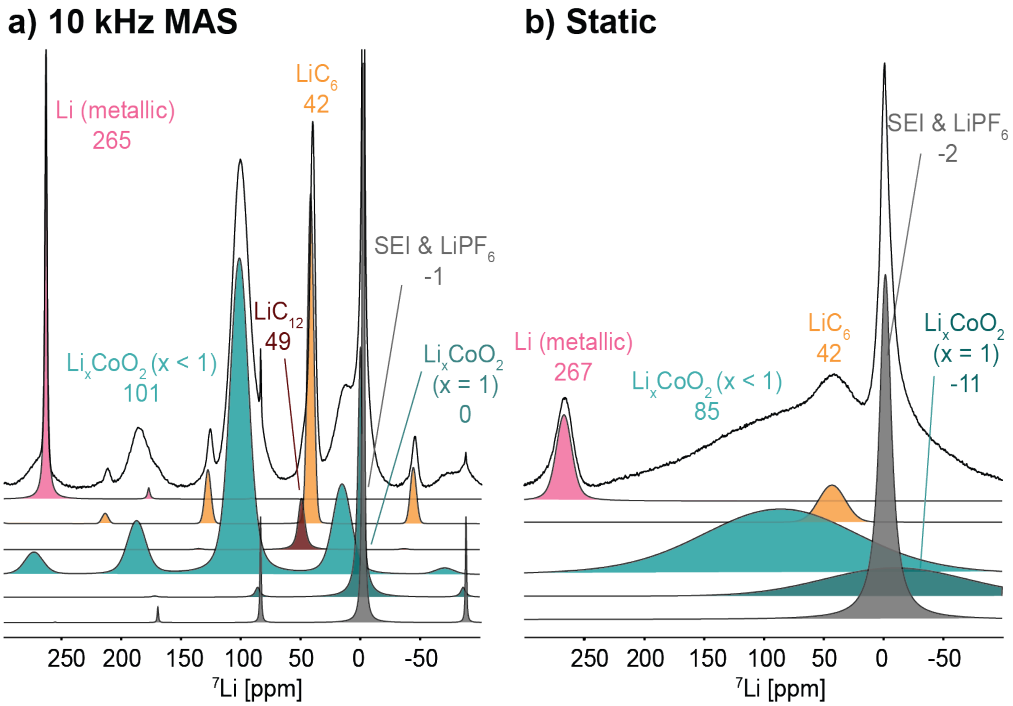

Figure 4.10: Deconvolution of $^7$Li NMR spectra of a fully charged LCO/graphite cell ($C_{4.1V}$) under (a) 10 kHz MAS and (b) static conditions

summarized in Figure 4.11. At low states of charge, only phases of LCO are apparent in the spectra. It can be seen that LCO is only getting partially delithiated on charge, with a substantial amount remaining as $Li_{x=1}CoO_2$ up to 0.4 mA h. At 0.7 mA h both concentrated and dilute stages of graphite appear and grow in intensity up to the end of charge. At the top of charge about 5% to 10% of the signal is attributed to lithium metal, which disappears partially on discharge. On discharge the lithium-ions only partially move back into the LCO structure as indicated by the small intensity of $Li_{x=1}CoO_2$ at the end of discharge, which further strengthens the hypothesis of lithium inventory loss due to the formation of SEI. Is is difficult to quantify exactly how much lithium is lost to degradation products as the electrolyte is replenished after every NMR measurement, leading to the fluctuating integral intensity of the

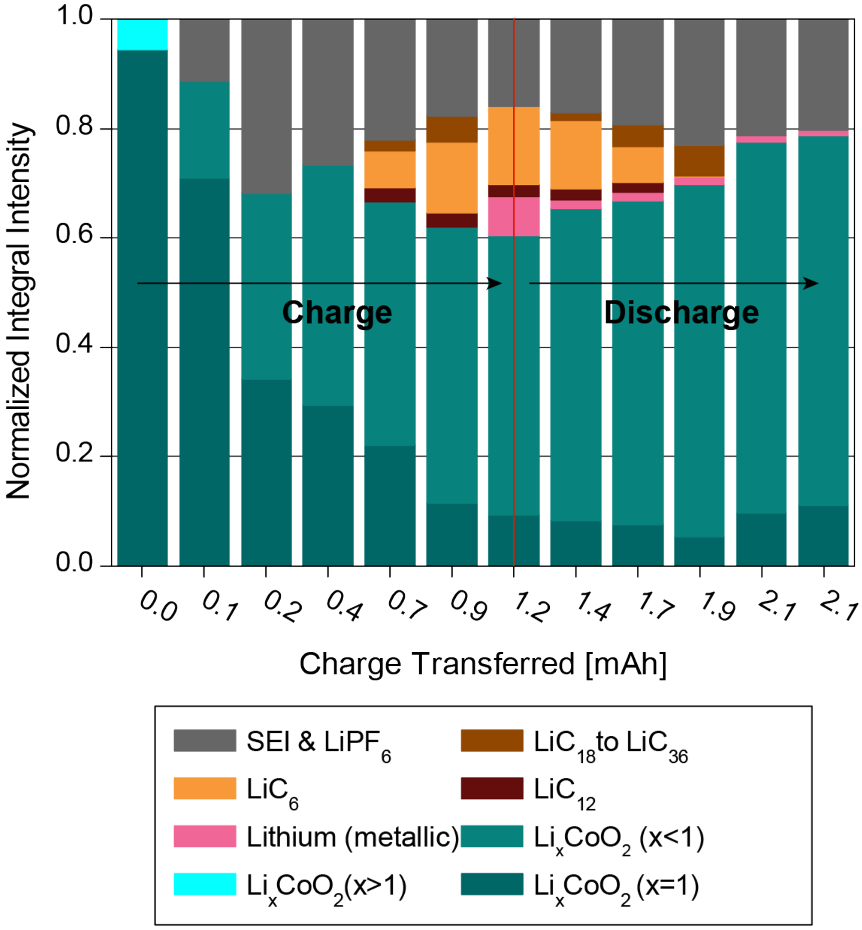

Figure 4.11: Normalized integral intensity of the different electrochemical species extracted from deconvolution data corresponding to the charge transferred.

SEI and $LiPF_6$ signal. Improvements to the design are necessary to circumvent the issue of solvent leakage in these types of cells to make this experiment truly in situ.

## 4.5 Conclusion

This work successfully demonstrates the solid-state MAS $^7$Li NMR analysis of an electrochemical cell under magic-angle spinning conditions. By introducing an in situ method with MAS capability, adequate resolution is achieved which allows for monitoring of the full lithium inventory during cycling. When combined with the MATPASS technique, a tremendous boost in resolution is achieved. This strategy paves the way toward acquisition of valuable in situ data on the formation and transformations of metastable states within the active materials of both electrodes; data that is difficult to obtain from static in situ NMR experiments alone. The remarkable ability to observe the journey of lithium with this in situ method promotes qualitative and quantitative analyses of different Li species in a full cell. This is valuable not only for mechanistic studies of lithium-ion battery materials but also provides a more complete picture of a full electrochemical cell.

## 4.6 Future Work

Further optimization of the cell design such as better sealing or switching to a polymer electrolyte to avoid electrolyte evaporation as well as mounting a photoresistor on the top of the rotor cap to control current rate and to make the experiment truly in operando are possible next steps. In Appendix A a polymer electrolyte is introduced, which shows promising characteristics for being able to be incorporated in these types of in situ cells. This would allow for a more robust setup, which does not require filling the rotor with liquid electrolyte after spinning. In addition, in order to implement this technique to cathode materials with more significant paramagnetic contributions than LCO, improvement to the design is crucial to increase the spinning speed and therefore the spectral resolution that is required for such species. This poses its own challenges as the assembly of a battery inside a 4 mm rotor is challenging enough. As a long-term goal, a wireless charging mechanism would be optimal. Wireless charging and simultaneous spinning of the battery inside the probe is the ultimate goal of this project. A photovoltaic element could be integrated inside the rotor and a light source could be used to charge the battery. If these goals are met they would be the next breakthrough in in operando MAS NMR battery monitoring.

# Bibliography

[1] RE Gerald II, J Sanchez, CS Johnson, RJ Klingler, and JW Rathke. In situ nuclear magnetic resonance investigations of lithium ions in carbon electrode materials using a novel detector. *Journal of Physics: Condensed Matter*, 13(36):8269, 2001.

[2] Michel Letellier, Frédéric Chevallier, Christian Clinard, Elzbieta Frackowiak, Jean-Noël Rouzaud, Francois Beguin, Mathieu Morcrette, and Jean-Marie Tarascon. The first in situ $^7$Li nuclear magnetic resonance study of lithium insertion in hard-carbon anode materials for Li-ion batteries. *The Journal of Chemical Physics*, 118(13):6038–6045, 2003.

[3] Michel Letellier, Frédéric Chevallier, and Mathieu Morcrette. In situ $^7$Li nuclear magnetic resonance observation of the electrochemical intercalation of lithium in graphite; 1st cycle. *Carbon*, 45(5):1025–1034, 2007.

[4] Baris Key, Rangeet Bhattacharyya, Mathieu Morcrette, Vincent Seznec, Jean-Marie Tarascon, and Clare P Grey. Real-time NMR investigations of structural changes in silicon electrodes for lithium-ion batteries. *Journal of the American Chemical Society*, 131(26):9239–9249, 2009.

[5] Keiji Shimoda, Miwa Murakami, Daiko Takamatsu, Hajime Arai, Yoshiharu Uchimoto, and Zempachi Ogumi. In situ NMR observation of the lithium extraction/insertion from $LiCoO_2$ cathode. *Electrochimica Acta*, 108:343–349, 2013.

[6] Sergey A. Krachkovskiy, Jamie M. Foster, J. David Bazak, Bruce J. Balcom, and Gillian R. Goward. Operando Mapping of Li Concentration

Profiles and Phase Transformations in Graphite Electrodes by Magnetic Resonance Imaging and Nuclear Magnetic Resonance Spectroscopy. *The Journal of Physical Chemistry C*, 122(38):21784–21791, 2018.

[7] Michel Letellier, Frédéric Chevallier, François Béguin, Elzbieta Frackowiak, and Jean-Noël Rouzaud. The first in situ $^7$Li NMR study of the reversible lithium insertion mechanism in disorganised carbons. *Journal of Physics and Chemistry of Solids*, 65(2-3):245–251, 2004.

[8] Xiang Li, Mingxue Tang, Xuyong Feng, Ivan Hung, Alyssa Rose, Po-Hsiu Chien, Zhehong Gan, and Yan-Yan Hu. Lithiation and Delithiation Dynamics of Different Li Sites in Li-Rich Battery Cathodes Studied by Operando Nuclear Magnetic Resonance. *Chemistry of Materials*, 29(19): 8282–8291, 2017.

[9] Michel Ménétrier, Ismael Saadoune, Stéphane Levasseur, and Claude Delmas. The insulator-metal transition upon lithium deintercalation from $LiCoO_2$: electronic properties and $^7$Li NMR study. *Journal of Materials Chemistry*, 9(5):1135–1140, 1999.

[10] Elodie Salager, Vincent Sarou-Kanian, M Sathiya, Mingxue Tang, Jean-Bernard Leriche, Philippe Melin, Zhongli Wang, Hervé Vezin, Catherine Bessada, Michael Deschamps, et al. Solid-State NMR of the Family of Positive Electrode Materials $Li_2Ru_{1-y}Sn_yO_3$ for Lithium-Ion Batteries. *Chemistry of Materials*, 26(24):7009–7019, 2014.

[11] Pedro M Aguiar, Jacques-François Jacquinot, and Dimitris Sakellariou. Experimental and numerical examination of eddy (Foucault) currents

in rotating micro-coils: Generation of heat and its impact on sample temperature. *Journal of Magnetic Resonance*, 200(1):6–14, 2009.

[12] Annica I. Freytag, Allen D. Pauric, Meng Jiang, and Gillian R. Goward. $^{7}$Li and $^{29}$Si NMR Enabled by High-Density Cellulose-Based Electrodes in the Lithiation Process in Silicon and Silicon Monoxide Anodes. *The Journal of Physical Chemistry C*, 123(18):11362–11368, 2019.

[13] Roman Nölle, Kolja Beltrop, Florian Holtstiege, Johannes Kasnatscheew, Tobias Placke, and Martin Winter. A reality check and tutorial on electrochemical characterization of battery cell materials: How to choose the appropriate cell setup. *Materials Today*, 32:131–146, 2020.

[14] Johannes Kasnatscheew, Tobias Placke, Benjamin Streipert, Sergej Rothermel, Ralf Wagner, Paul Meister, Isidora Cekic Laskovic, and Martin Winter. A tutorial into practical capacity and mass balancing of lithium ion batteries. *Journal of The Electrochemical Society*, 164(12):A2479–A2486, 2017.

[15] Ivan Hung, Lina Zhou, Frederique Pourpoint, Clare P Grey, and Zhehong Gan. Isotropic high field NMR spectra of Li-ion battery materials with anisotropy >1 MHz. *Journal of the American Chemical Society*, 134(4): 1898–1901, 2012.

[16] Ramesh Shunmugasundaram, Rajalakshmi Senthil Arumugam, Kristopher J. Harris, Gillian R. Goward, and J. R. Dahn. A Search for Low-Irreversible Capacity and High-Reversible Capacity Positive Electrode Materials in the Li–Ni–Mn–Co Pseudoquaternary System. *Chemistry of Materials*, 28(1):55–66, 2015.

## Chapter 5

# In Situ $^7$Li NMR Analysis of Silicon Anodes in Full Cells under Fast-Charging Conditions using a Parallel-Plate Resonator

*This section shows current progress for the in situ analysis of fast-charging of silicon anodes. Data collection and analysis were performed by Annica I. Freytag. Kevin J. Sanders assisted in the collection of magnetic resonance image (MRI) data. Nafiseh Zaker collected the scanning electron microscopy (SEM) image. Measurements were performed at McMaster University.*

## 5.1 Introduction

The rise in popularity of electric vehicles (EVs) in the automobile industry has sparked interest in many research avenues pertaining to LIBs. However, in order for EV's to be competitive with conventional combustion engine vehicles, optimization of their longevity, energy capacity, and fast-charging capabilities is crucial.[1] Particularly, the charging time of current EV's is not ideal. This is largely due to the effect of lithium deposition occuring on the graphite anode when high currents are applied to the cell.[2] Under standard charging conditions (e.g. C/10) lithium diffuses into the graphitic network through different intercalation stages as demonstrated in Chapter 1.[3] However, under fast-charging conditions lithium deposits on the anode surface as metallic lithium, which can have detrimental long-term effects and can lead to battery failure.[4] Currently, the EV industry is shifting towards using composite silicon/graphite electrodes to take advantage of the high capacity of silicon. Silicon cannot only reach much higher capacities than graphite but is also expected to be less prone to lithium deposition under fast-charging conditions.[5]

In situ NMR has been applied to a variety of real-time studies of electrochemical cells in the past and has shown to be a powerful technique to uncover dynamics and phase changes in battery materials in real-time.[6–14] Recently, a novel in situ NMR technique using a parallel-plate (PP) resonator, which allows for quantification of lithium species in graphite during fast-charging (1C) has been demonstrated.[15,16] The field homogeneity throughout the cell is superior to other resonator designs introduced in Chapter 2.6 such as a solenoid coil and can be readily applied to rectangular flat-cell designs without suffering signal loss due to current collectors or other metallic components in the cell. The PP resonator design was first introduced by Meadowcroft et al. to investigate histological tissue through MRI.[17] This cell design allows for an increased filling factor and high sensitivity due to the close proximity of the RF resonator plates to the sample which produces a uniform $\vec{B}_1$ field distribution in the planar region between the two plates. This is of importance for implementing this resonator design for electrochemical cells as current collectors could otherwise interfere with the RF field. The $\vec{B}_1$ field in a PP resonator is generated by the current flowing through the plates in opposing directions, which leads to an additive effect in between the plates and a cancellation on the outside of the resonator.

In the following, we will investigate how different current rates will affect not only the formation of silicides but also the formation of metallic lithium on the surface of silicon anodes using the PP resonator design. In addition, this design makes MRI of the cell possible, which is used to image the distribution of deposited lithium inside the electrochemical cell.

## 5.2 Experimental

A PP resonator (see schematic in Figure 5.1) was built by attaching adhesive copper foil to each side of a flat glass capillary (0.4 x 8.0 x 50.0 mm ID, VitroCom). They were connected with two 47 pF capacitors on one end. On the opposite end, copper wires were soldered in order to attach the PP resonator to an NMR probe. The materials used for building the electrochemical cell were $LiNi_{0.6}Mn_{0.2}Co_{0.2}O_2$ (NMC622, General Motor, 28.86 mg/cm$^2$, 4.5 mAh/cm$^2$, size 5 cm x 0.6 cm) and silicon (General Motors, 2.05 mg/cm$^2$, 4.8 mAh/cm$^2$, size 5 cm x 0.7 cm) in addition to Celgard 2325 separator (5 cm x 0.8 cm). The silicon electrode was first heat-treated at 200°C under vacuum for 30 hours. An SEM image of the pristine silicon electrode was collected on an FEI Magellan 400 with a low accelerating voltage of 2 kV with a 6.3 pA incident current at the Canadian Centre for Electron Microscopy. In the image, the secondary electrons were collected, which are revealing the fine features of the surface in high resolution via the Through-the-lens detector. The SEM image in Figure 5.2 shows non-uniform particle sizes are apparent in the silicon electrode with

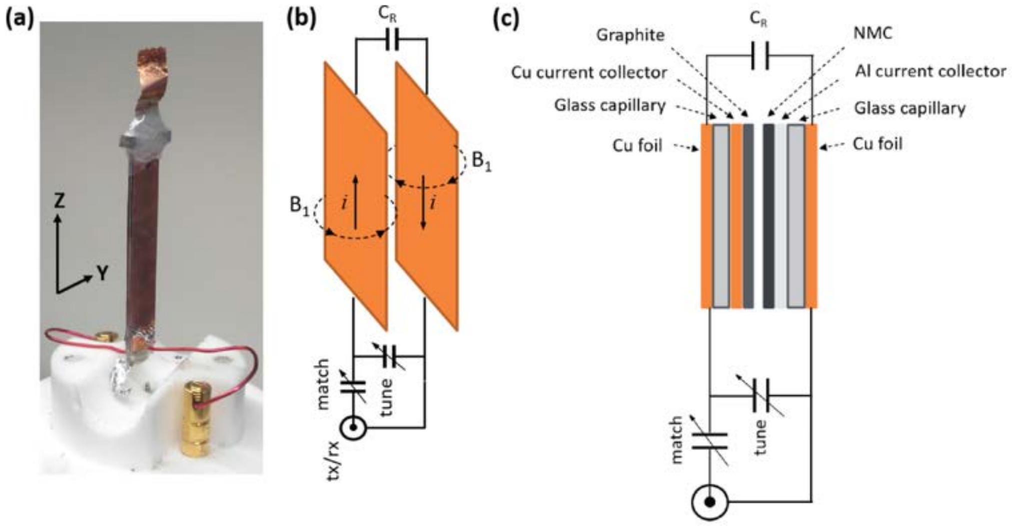

Figure 5.1: (a) in situ parallel-plate resonator cell (b) Schematic of parallel-plate resonator (c) cross-sectional view. Reproduced with permission from the Journal of the Electrochemical Society, 2020, 167, 130514.[16] Copyright ©2020, with permission from ECS.

sizes varying between about 0.5 µm to 2 µm. The electrodes and one layer of separator was inserted into the capillary and a piece of aluminum foil were inserted behind the cathode to act as a current collector as shown in Figure 5.1. The bottom of the capillary was sealed with epoxy (Araldite 2014), dried under vacuum for 24 hours at 80 °C and then moved to an argon-filled glove box (MBraun). The in situ cell was then filled with approximately 0.2-0.3 mL 1M $LiPF_6$ in EC/DEC until saturated.

The formation cycle was performed inside the glove box using an ARBIN BT 2000 battery cycler using a 0.6 mA current for charge and was charged up to 4.2 V (C-rate approximately C/20). After a 2 minutes rest period, the discharge to 3.0 V using a 0.6 mA current was conducted. The irreversible capacity during the first cycle was 37%. The electrolyte was refreshed after the formation cycle before sealing the top of the capillary tube with epoxy. The charging protocol is summarized in Table 5.1. Coin cells using the same

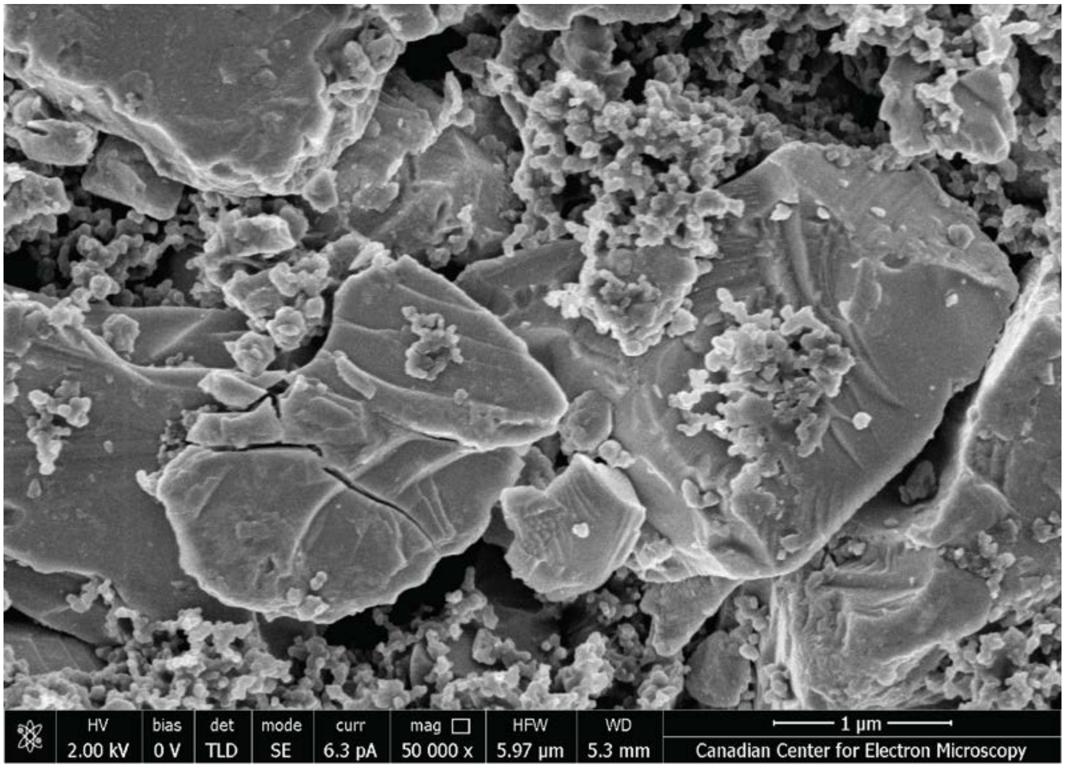

Figure 5.2: SEM image of the pristine silicon anode material revealing micron-sized silicon particles nested in a binder network.

electrode materials and charging protocols (Table 5.2) were assembled and cycled to compare capacity fade to the in situ cell format.

$^7$Li NMR spectra were acquired at 25 °C on a Bruker Avance 300WB spectrometer using a static probe. Pulse-acquire spectra were collected for three consecutive charge cycles (1C, C/4 and 2C) using a recycle delay of 0.2 s, 512 scans, which took about 2 minutes of acquisition time per spectrum using a 32.5 µs $\pi/2$ pulse at 40 W. Charging was stopped to acquire NMR spectra every 10, 40 and 5 minutes for the 1C, C/4 and 2C charge, respectively. Figure 5.3 shows the charging setup for the in situ data collection outside of the NMR magnet. The NMR spectra were processed using ssNake.[18] Zero and first-order phasing was applied to ensure that both the electrolyte and lithium metal region were in phase. Gaussian apodization was set to 90 and a third-order polynomial baseline correction was performed. The spectra were then plotted as a contour plot using Spyder, where the signal intensity was normalized to the maximum signal intensity of the electrolyte peak from the data set. The code used for plotting can be found in Appendix B.

| Cycle # | 1 | 2 | 3 | 4 | 5 | 6 | ≥7 |
|---|---|---|---|---|---|---|---|
| Charge Current (mA) | 0.6 | 1.3 | 1.3 | 8.6 | 2.2 | 17.2 | 1.3 |
| Discharge Current (mA) | 0.6 | 0.6 | 0.6 | 0.6 | 0.6 | 0.6 | 0.6 |

Table 5.1: Charging protocol for in situ NMR charging. Theoretical capacity 13.5 mA h. Note that cycle 4-6 were capacity-limited charges (capacity limited to 8.6 mA h) whereas charging for all other cycles were voltage-limited to 4.2 V. Discharge was limited to 3.0 V.

| Cycle # | 1 | 2 | 3 | 4 | 5 | 6 | ≥7 |
|---|---|---|---|---|---|---|---|
| Charge Current (mA) | 0.3 | 0.6 | 0.6 | 4.2 | 1.1 | 8.4 | 0.6 |
| Discharge Current (mA) | 0.3 | 0.3 | 0.3 | 0.3 | 0.3 | 0.3 | 0.3 |

Table 5.2: Charging protocol for coin cell charging NMC622/silicon. Theoretical capacity 5.7 mA h. Note that cycle 4, 5 and 6 were capacity-limited charges (capacity limited to 4.2 mA h) whereas charging for all other cycles were voltage-limited to 4.2 V. Discharge was limited to 3.0 V.

Chemical shift images were collected using a MicWB40 probe with a Micro2.5 gradient system. In order to verify an even field homogeneity and field of view (FOV) dimensions, a lithium-containing polymer electrolyte (LLTO/PEO/LiTFSI/SN) was imaged with the PP resonator with known

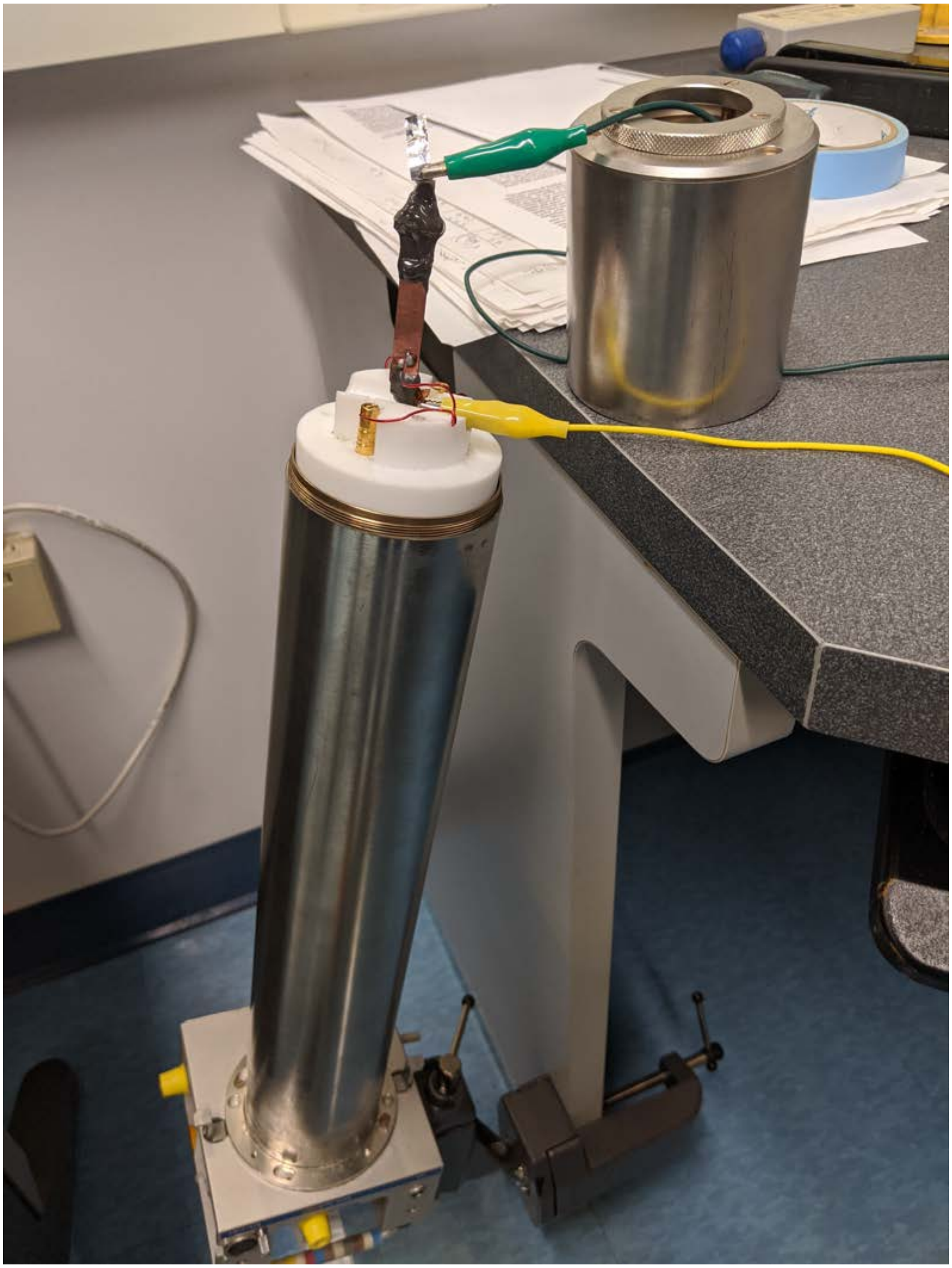

Figure 5.3: Charging setup for in situ NMR experiments using a parallel-plate resonator

dimensions of 0.6 cm by 4.1 cm. The FOV can be calculated by

$$\text{FOV} = \frac{N}{2\gamma t_p G_{max}} \tag{5.1}$$

which gives a FOV in units of cm, with $N$ as the number of phase encoded steps, $\gamma$ is the gyromagnetic ratio in units of G$^{-1}$ s$^{-1}$, $t_p$ the phase encoding time in units of s and $G_{max}$ is the maximum gradient strength in units of G/cm. $G_{max}$ needs to be scaled by the gradient % setting used in the pulse sequence (e.g., gpz6), as well as the shape factor for the gradient pulse. For a sine gradient, this factor is 0.64. $G_{max}$ for the MicWB40 probe is 150 G/cm at 60 A. The X, Y and Z amplifiers only deliver 40 A, therefore $G_{max,x}$, $G_{max,y}$ and $G_{max,z}$ should be treated as 100 G/cm.

Figure 5.4a shows the image of the polymer electrolyte in the spectral region of 7 ppm to −4 ppm collected with 32 steps in the Y dimension with the gradient varying linearly from −31.8 G/cm to 31.8 G/cm and 64 steps in the Z dimension with the gradient varying linearly from −22.9 G/cm to 22.9 G/cm with 128 transients and $t_p$ was set to 160 µs. The corresponding experiment time was 72 h. The obtained FOV dimensions were 5.3 cm in the Z direction and 1.9 cm in the Y direction. The image intensity was normalized to 1. The intensity is slightly higher at the top and bottom of the cell, which could be attributed to a slightly larger concentration of polymer electrolyte in that region. Some blurring along the edges indicate a small reduction of the field. This supports the findings by Krachkovskiy et al. who previously verified the field homogeneity of this particular PP resonator using a 1M LiTFSI in propylene carbonate (PC) solution.[16]

After cycle 6 during in situ charging, chemical shift images of the in situ

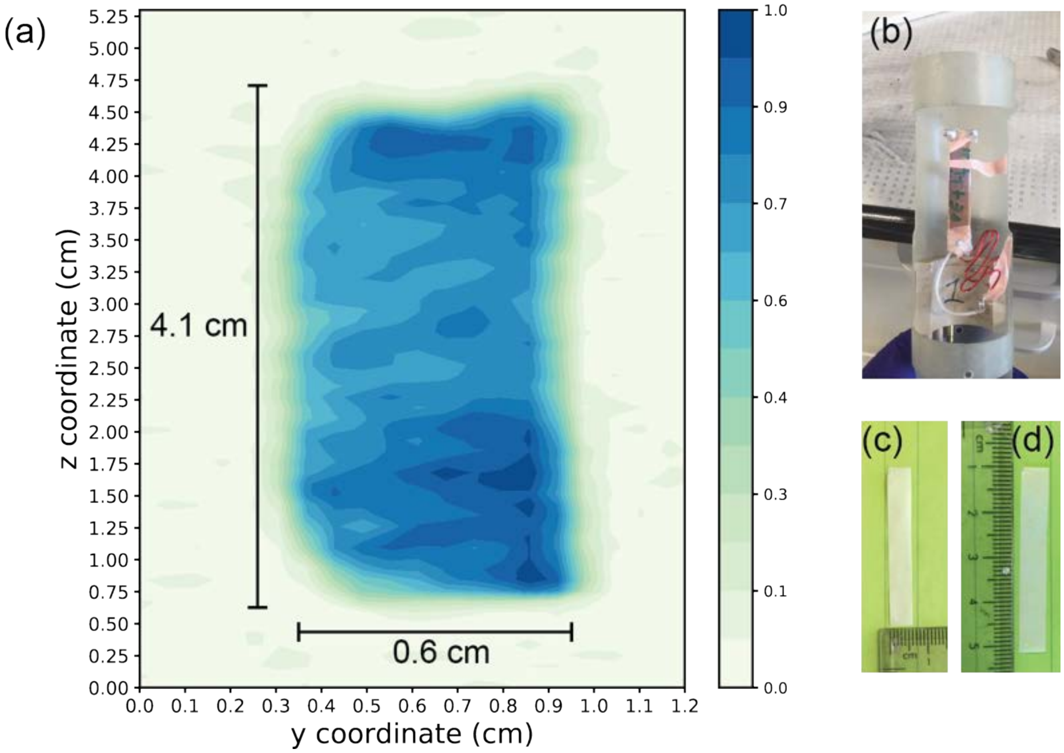

Figure 5.4: (a) Polymer electrolyte phantom chemical shift image (b) Alignment inside the MicWB40 probehead (c)(d) Dimensions of polymer electrolyte.

| | Cell A | | Cell B | |
|---|---|---|---|---|
| | Li metal | Electrolyte | Li metal | Electrolyte |
| $G_{max,y}$ [G/cm] | 22.3 | 22.3 | 15.9 | 1.6 |
| $G_{max,z}$ [G/cm] | 15.3 | 15.3 | 7.6 | 0.8 |
| Shift Region [ppm] | 248 to 287 | -16 to 25 | 243 to 286 | -18 to 24 |
| $t_p$ [µs] | 160 | 160 | 160 | 1600 |
| Recycle Delay [s] | 1 | 2 | 1 | 2 |
| Transients | 128 | 16 | 150 | 70 |
| Experiment Time [h] | 19 | 4.5 | 16.5 | 20 |

Table 5.3: CSI parameters for cell A and B. $G_{max,y}$ and $G_{max,y}$ are the maximum gradient strength values for the Y and Z gradient, respectively. $t_p$ is the gradient pulse length.

cell were collected, which required removal of the cell from the static probe and soldering of the copper wires to the imaging probe sleeve. The cell was aligned vertically in the magnet, where the electrodes are placed parallel to the ZY directions of the gradients. $^7$Li chemical shift imaging (CSI) was performed on both the electrolyte and lithium metal region using the pulse sequence introduced in Chapter 2.5.2. The gradient steps were 16 and 32 for the Y and Z directions, respectively. The setup parameters for two in situ cells (cell A and B) are summarized in Table 5.3.

## 5.3 Result and Discussion

### 5.3.1 In Situ $^7$Li NMR and MRI during Fast-Charging

Figure 5.5 summarizes the charge and discharge capacities for the in situ cell described in the experimental part. It is clear that over the first three cycles a large amount of active lithium is lost irreversibly to either SEI formation or other degradation products. Nevertheless, the cycle 3 discharge capacity reaches 64 % of its theoretical capacity. Cycles 4 to 6 were performed in situ, where the charging process was stopped in regular intervals in order to collect an NMR spectrum. These cycles were capacity-limited (to 8.6 mA h; the discharge capacity from cycle 3) in order to investigate the silicide formation under different charging conditions but keeping the amount of charge transferred the same. If these experiments were voltage-limited, a similar quantitative analysis would not be possible due to the large overpotentials reached during charging of the in situ cell.

Silicon-lithium alloys, or silicides ($Li_xSi$), show structural differences de-

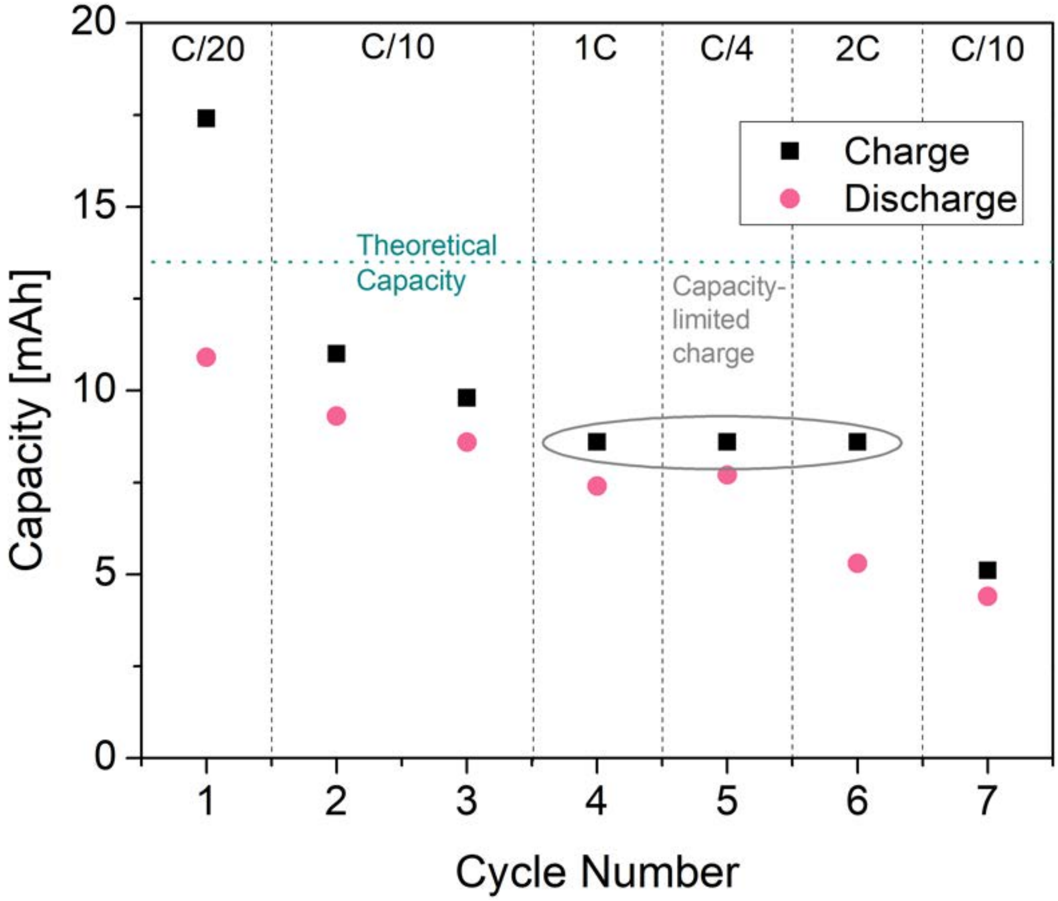

Figure 5.5: Charge and discharge capacities for the first seven cycles during in situ charging. C-rate was calculated based on the theoretical capacity (13.5 mAh). The discharge current is constant at D/20 (0.6 mA), whereas the charge current is 0.6 mA, 1.3 mA, 8.6 mA, 2.2 mA and 17.2 mA for C/20, C/10, 1C, C/4 and 2C, respectively. Note that the C-rate was recalculated before cycle 4 from the discharge capacity of the previous cycle (8.6 mAh) due to accumulation of irreversible capacity during the first three cycles.

pending on the state of charge. Figure 2.16 in Chapter 2 summarizes those structural changes during lithiation and their respective chemical shifts in $^7$Li NMR. At low states of charge polymeric Si clusters form (phase 1), which correspond to a shift range of 0-10 ppm. At x=2 to x=3.5, these polymeric clusters break down to form smaller Si clusters and isolated Si (phase 2), with the shift ranging between 10-20 ppm. At high lithiation, the clusters are broken

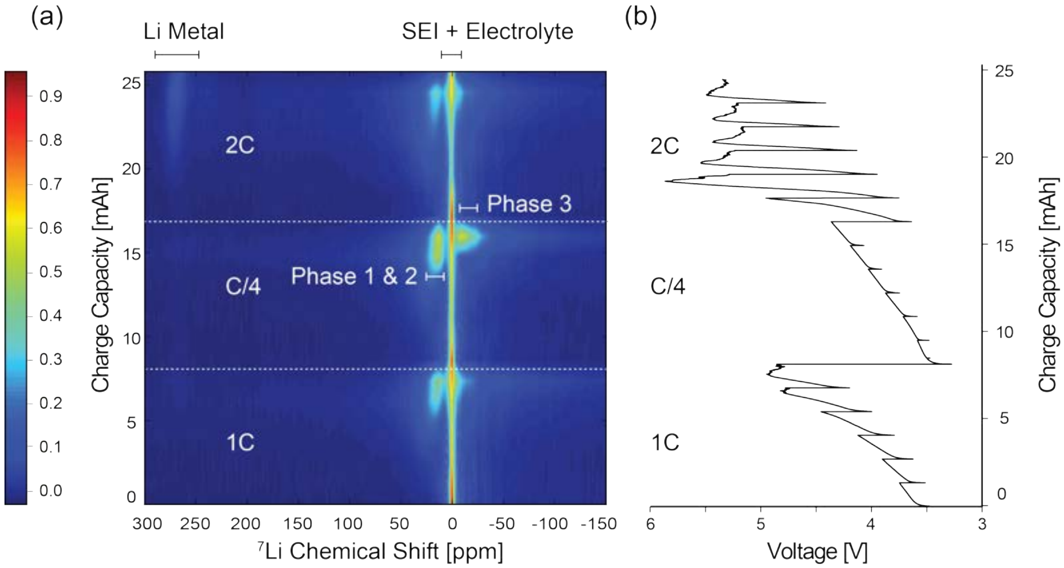

Figure 5.6: (a) Contour plot single-pulse $^7$Li NMR static spectra acquired for three consecutive charge cycles (1C, C/4 and 2C) of an NMC622/Si cell, recycle delay 0.2 s, 512 scans, acquisition time 2 minutes (b) Charging profile of the electrochemical cell; charging was stopped to acquire NMR spectra every 10, 40 and 5 minutes for the 1C, C/4 and 2C charge, respectively. Capacity was limited to 8.6 mAh for all three charges.

down completely and only isolated silicon (phase 3) are apparent. Their shifts range from 5 to -15 ppm. Phase 3 is a metastable phase, which is absent in ex situ studies.[6] It is thought to be the major culprit for capacity fading in silicon anodes as it comes with an increased volumetric expansion and hence cracking of the SEI, which leads to separation of the active material from the current collector.[6] This leads to an increased formation of SEI on subsequent cycles, and therefore a large amount of lithium loss. Ways to mitigate this cracking includes utilizing nano-sized silicon, optimized binder materials to hold together the silicon framework, or by using modified silicon-containing electrodes like silicon monoxide, which was discussed in an earlier study.[11]

Figure 5.6 shows the in situ $^7$Li NMR spectra for the three consecutive in situ charges (1C, C/4 and 2C) as well as the corresponding charge profiles. No plated lithium appears during the 1C and C/4 charge. Lithium metal appears at around 260 ppm in $^7$Li NMR and is indicative of the formation of lithium metal on the surface of the anode. Only during the 2C charge a small amount of lithium metal is plated, visualized by the increase in intensity in the contour plot around 260 ppm at the end of the 2C charge. This bodes well for the use of silicon as an anode material for fast-charging compared to graphite, which already shows significant lithium plating at 1C under similar cycling conditions.[16] The distribution and intensity of silicides (range between 20 to -20 ppm) is quite different for each charge cycle. At a low charge rate (C/4) all three silicide phases (1 to 3) form, whereas at high currents (1C and 2C) the active lithium species preferably form phase 1 and 2 silicides or metallic lithium. The formation of metallic lithium at 2C can be explained by looking at the charge curves in Figure 5.6b. At high currents, voltages above 5 V occur, which can be partially attributed to the cell design. Non-uniform pressure can lead to increased resistance in the cell and therefore a larger overpotential, which in turn could cause the anode potential to dip below 0 V. At anode potentials below 0 V, lithium plating competes with the silicide formation and based on the results, lithium plating seems to be the preferred pathway for the active lithium species under these conditions. In order to investigate this further it is crucial to implement a reference electrode to monitor if the anode potential reaches values below 0 V at high C-rates. The integration of a reference electrode is currently underway which involves a redesign of the in situ cell.

Figure 5.7a and b show chemical shift images collected after cycle 6. Figure 5.7c shows the alignment of the PP cell with respect to the Y and Z gradients in the imaging probe. Note that the cell is slightly tilted to the left, which can

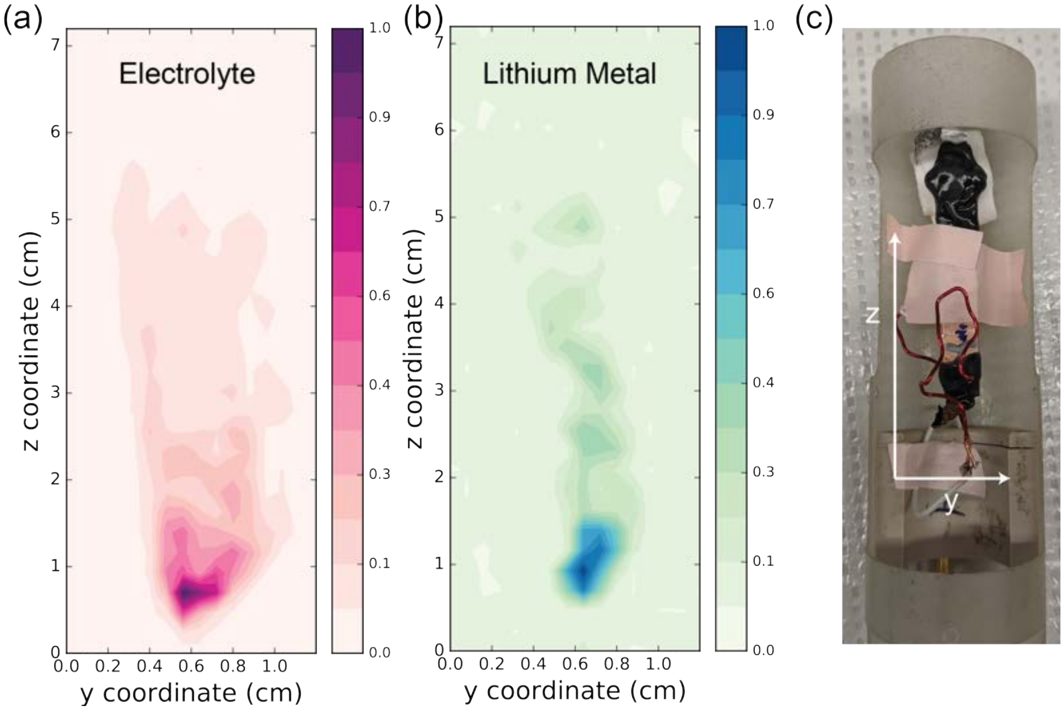

Figure 5.7: (a) MRI of in situ cell of (a) electrolyte and (b) lithium metal region normalized to their respective maximum intensity. Both images were taken after cycle 6 (after 1C, C/4 and 2C charge) in the discharged state (c) photo of in situ cell orientation for MR images

also be seen in the MR images. The images show the distribution of both the electrolyte and lithium metal inside the cell. It is clear that the distribution of lithium metal overlaps with where the electrolyte intensity is highest in the cell. The electrolyte intensity spans over an area of about 0.7 cm in the y-direction and 5.0 cm in the z-direction. However, the large intensity of both electrolyte and lithium metal signal at the bottom of the cell indicates that the in situ cell partially dried out or pressure built-up due to gas formation caused the electrolyte to be "pushed" to the bottom of the cell and therefore lithium metal formation was also favoured to occur at the bottom of the cell where the electrolyte concentration was highest.

### 5.3.2 Reproducibility

Undoubtedly, the large amount of both electrolyte and lithium metal at the bottom of the cell is concerning, which is why a second cell (denoted as cell B in Figure 5.8) was cycled under the same conditions as the previously introduced cell (cell A). Figure 5.8 shows the charging profiles for both cells for the 1C, C/4 and 2C charge. The C-rate for the cells were calculated based on the discharge capacity of cycle 3, which was 8.6 mA h and 10.4 mA h for cell A and B, respectively. It is obvious that the charge profile for cell A is consistently higher than for cell B. Evidently, the $^7$Li in situ NMR spectra at the top of charge for each cycle show differences as well. Cell A in Figure 5.8b shows the formation of small amounts of lithium metal at 260 ppm, whereas cell B does not. In addition, a small shoulder signal at negative shift values suggests the appearance of phase 3 silicides. A more prominent difference between cell A and B is seen in Figure 5.8d. Although both charge profiles look practically identical, the NMR spectra reveal contrasting findings. In cell A a large amount of phase 3 silicides occur at the end of charge, which are absent in cell B. The phase 3 silicide is known to be short-lived and disappears quickly after stopping the current.[6] A comparison of cell A right after the C/4 charge and a consecutive 10 minutes rest period can be found in Figure B.1, which confirms the short life-time of this phase. However, the largest difference between cell A and B is apparent for the 2C charge in Figure 5.8f. Cell A shows a larger overpotential, which coincides with plated lithium appearing in the $^7$Li NMR spectrum. Interestingly, no lithium metal can be seen in cell B during the 2C charge (Figure 5.8f). A comparison of the in situ contour plots for both cells is shown in Figure 5.9. At first glance it can be seen that in cell A an

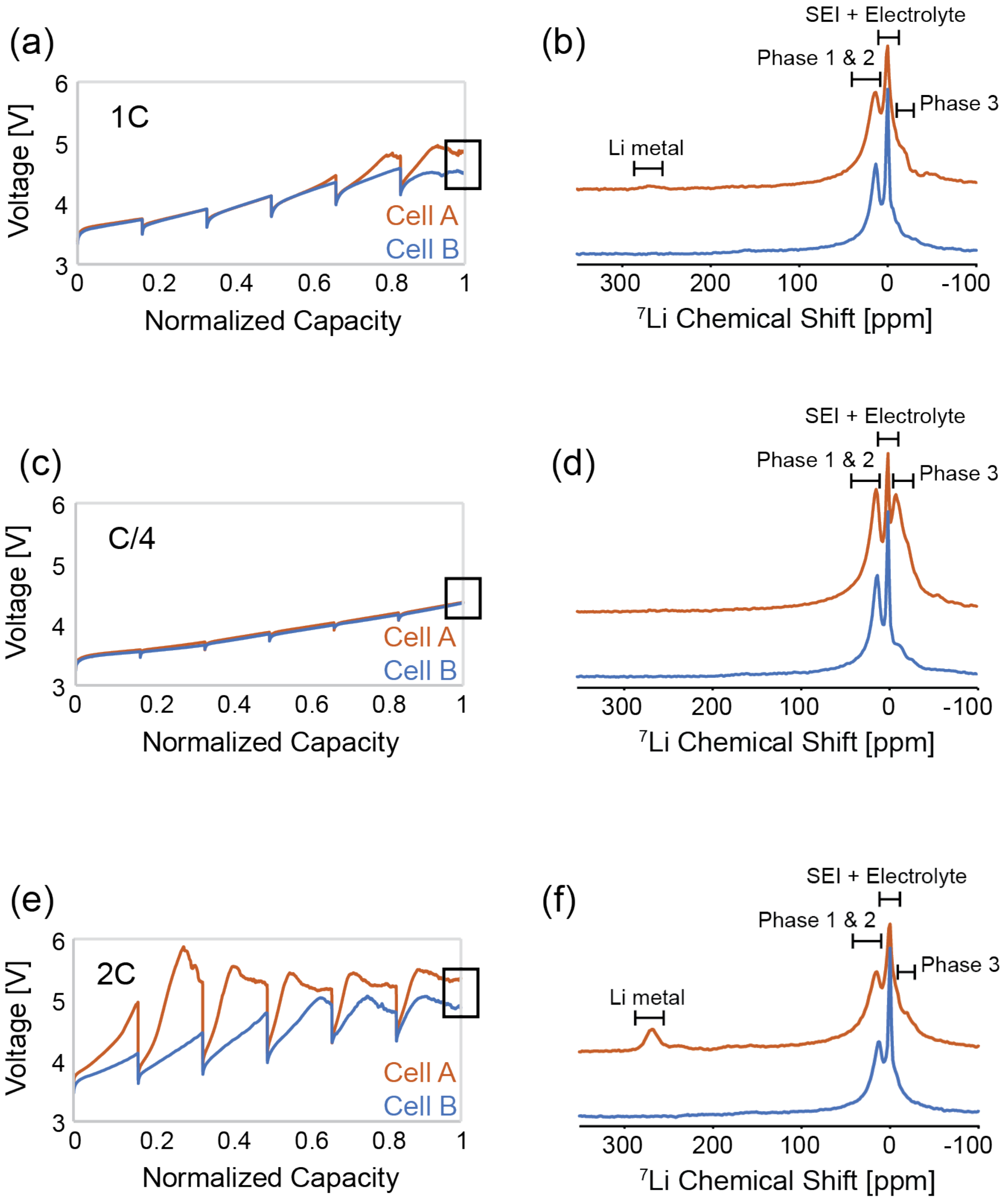

Figure 5.8: (a) 1C, (c) C/4, (e) 2C charge profiles for cell A (orange) and cell B (blue); (b), (d), (f) $^7$Li NMR spectra at the top of charge (black rectangle in charge profile) for cell A and cell B (b) 1C charge (d) C/4 charge (f) 2C charge

overall much larger amount of silicides form than in cell B. This is unexpected, as the quantity of silicides should be similar in both cells because they were charged under the same conditions. This clearly shows that there is a large discrepancy between the two in situ cells, which could be attributed to uneven pressures in the cell. To investigate this further, CSI was conducted on this cell to compare the distribution of the electrolyte in this cell (cell B) to the previous cell (cell A).

Figure 5.10 shows chemical shift images of cell B of the electrolyte and lithium metal region. The formation of lithium metal at the top of the cell is surprising, as this could not be resolved during the in situ NMR collection (Figure 5.8f). One explanation could be that due to the fact that the MRIs are collected with a different probe, which requires the removal from one probe and attaching it with solder to the imaging probe sleeve. It could be that the lithium metal formed outside of the $B_1$ field at the edge of the capillary and then got dislodged during the transfer to the other probe. This is clearly an issue and will need to be addressed in future cell designs. Preferably, an in operando design that allows for the collection of CSIs during cycling to monitor the silicide formation and metallic lithium deposition would be ideal.

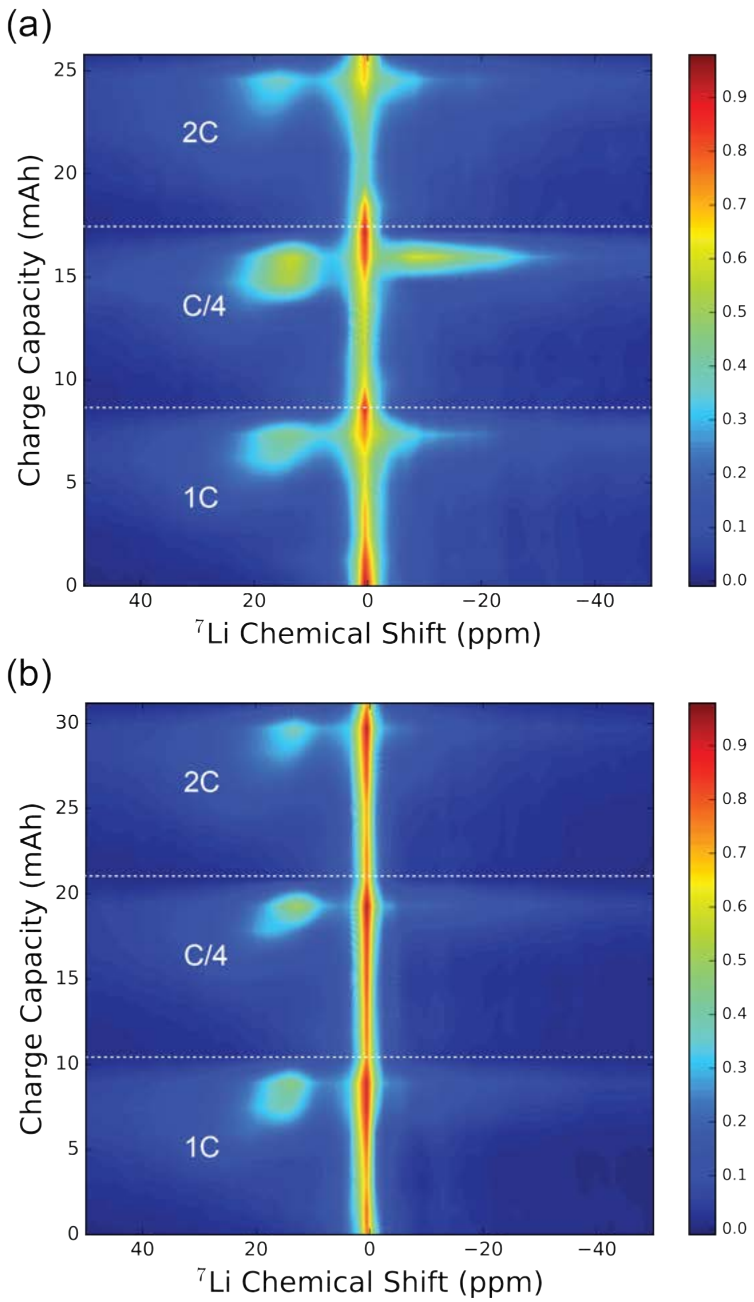

Figure 5.9: (a) Contour plot single-pulse $^7$Li NMR static spectra acquired for three consecutive charge cycles (1C, C/4 and 2C) of an NMC622/Si cell, recycle delay 0.2 s, 512 scans, acquisition time 2 minutes; charging was stopped to acquire NMR spectra every 10, 40 and 5 minutes for the 1C, C/4 and 2C charge, respectively. For all three charges capacity was limited to 8.6 mA h for cell A (a) and 10.4 mA h for cell B (b).

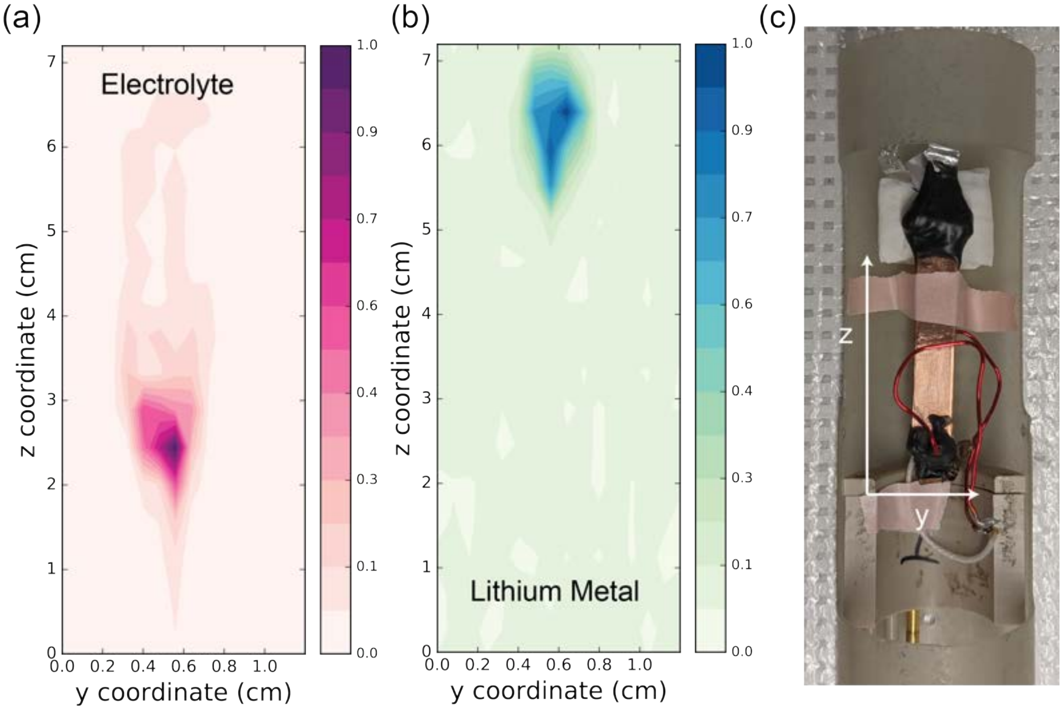

Figure 5.10: (a) MRI of in situ cell B of (a) electrolyte and (b) lithium metal region normalized to their respective maximum intensity. Both images were taken after cycle 6 (after 1C, C/4 and 2C charge) in the discharged state (c) photo of in situ cell orientation for MR images

### 5.3.3 Comparison to a Coin Cell Format

In order to investigate the reproducibility of the data even further and to compare it to a more standard format, a coin cell was cycled using the same active materials as the one used for the in situ cells. Figure 5.11 shows a comparison of the charge and discharge capacities for the in situ and coin cell formats. It is evident, that the in situ cells experience a much larger capacity drop over the first 18 cycles than a coin cell. Cell A reaches only 24% of its theoretical capacity after 18 cycles and cell B reaches 46%, whereas in the coin cell format the discharge capacity after 18 cycles is 4.1 mA h corresponding to a loss of only 28 %.

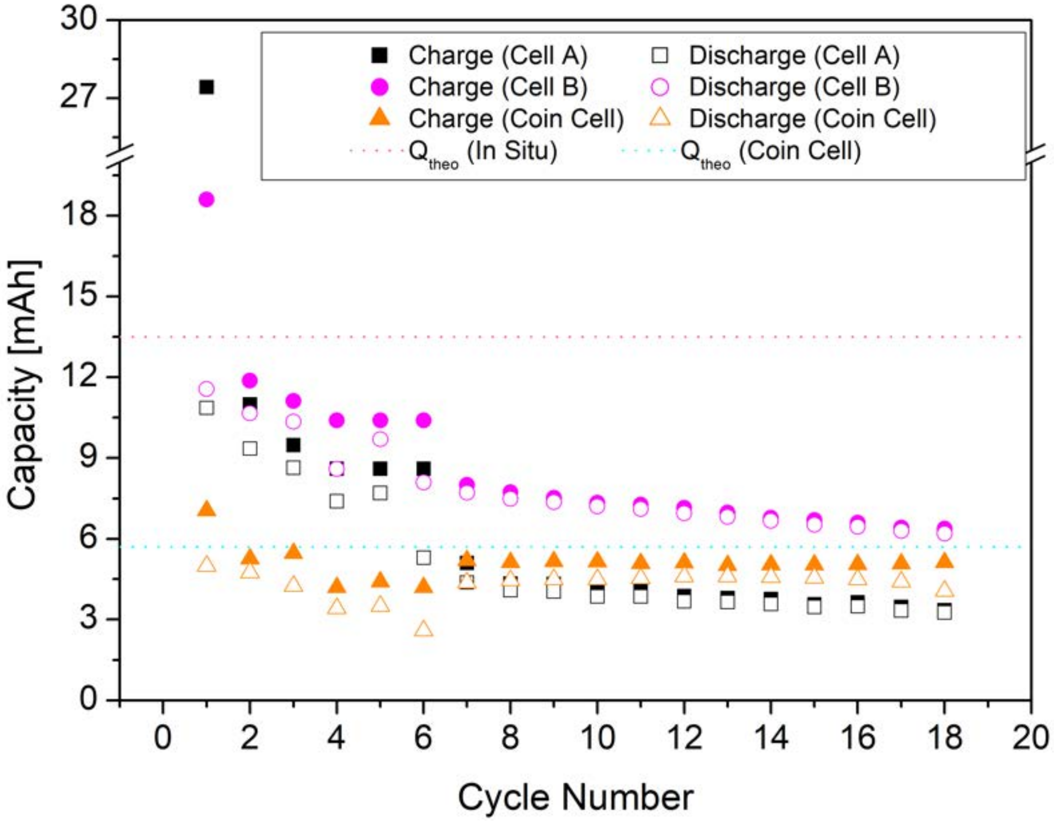

Figure 5.11: Charge and discharge capacities for the first 18 cycles for in situ cell A and B and a coin cell using the same active materials NMC622/silicon. Cycling protocol and applicable currents are found in Table 5.1 and 5.2 $Q_{theo}$ indicates the theoretical capacity values for both in situ cells ($Q_{theo}$ = 13.5 mA h)and the coin cell (surface area 1.27 $cm^2$,$Q_{theo}$ = 5.7 mAh).

When comparing the coin cell to the in situ cell charging profiles it is evident that the coin cells show less of an overpotential than the in situ cells as shown in Figure 5.12. For all three C-rates, the coin cell performs better than the in situ cell. Towards the end of the 1C charge, the in situ cell potential decreases, which is attributed to lithium metal formation. However, the coin cell does not show a similar behaviour. Similarly, during the C/4 charge, the potential curve for the coin cell is consistently lower than for the in situ cell. The largest discrepancy is apparent for the 2C charge, where both cells undergo a drop in potential. The coin cell potential increases dramatically up to about 30% state of charge, whereas the in situ cell potential only starts to decrease around 65% state of charge. Clearly, the large differences between the two different cell designs infers that different electrochemical processes occur in the cells. This brings up the burning question if lithium plating in the in situ cells only occurs at these C-rates because of their inherent higher internal resistance, larger amount of SEI formation, etc. Further experiments utilizing reference electrodes are necessary to verify this in addition to improving the pressure distribution in the cell, which can decrease the overpotential as well.

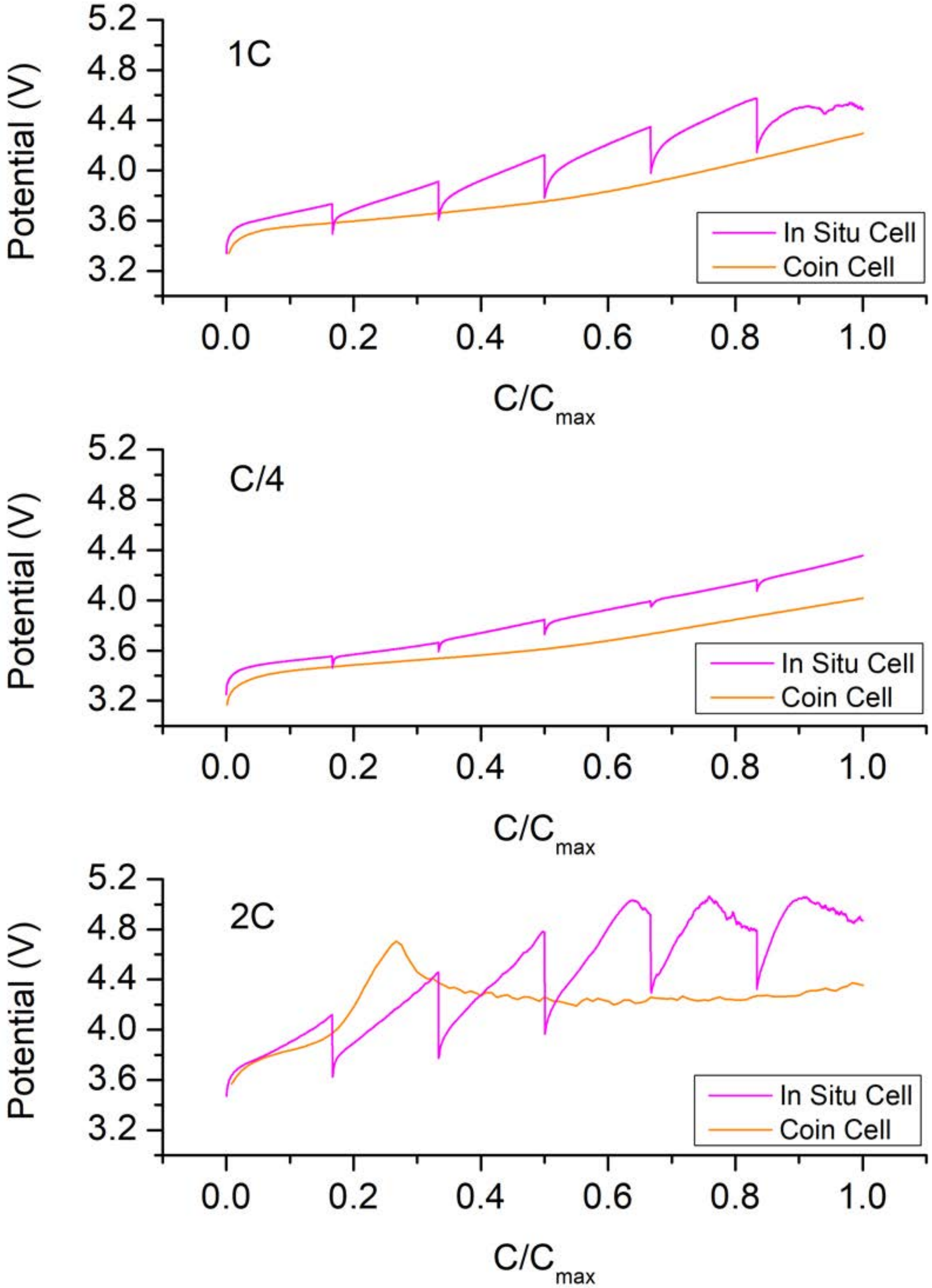

Figure 5.12: Charge profiles for in situ cell B and a coin cell using NMC/silicon as electrodes under different charging conditions (top to bottom: 1C, C/4 and 2C). C/C$_{max}$ indicates the normalized capacity for each charge.

## 5.4 Summary

The in situ method of monitoring of lithium plating in electrochemical cells and in particular the here described silicon anodes are of great interest for the battery community. With silicon anodes being incorporated in commercial cells it is of utmost importance to understand the fast-charging behaviour of such electrodes. The presented study shows interesting similarities and differences between graphite and silicon anodes. It was shown that the herein described in situ NMR technique can be applied to NMC622/silicon cells to investigate the silicide formation under fast-charging conditions.

However, the current in situ cells lack reproducibility, which makes it difficult to extract quantitative information from these experiments. Qualitatively, this study has shown some compelling findings, e.g., the competitive formation of silicides versus lithium metal at high currents. Lithium metal formation seems to always be favoured when these cells reach potentials higher than around 5 V. The challenges concerning overpotentials in these kinds of in situ cells can be studied further by incorporating reference electrodes in order to monitor the potential on the anode side. This is currently being implemented in the Goward group and once optimized for graphite, it should be transferable to silicon anodes also.

In addition, this cell design allows for MRI of the cells. The distribution of lithium metal varies dramatically with each cell. It would be interesting to investigate differences in the plating behaviour when applying even pressure to the cell as well as analyzing silicon/graphite composite electrodes and identify how different doping levels of silicon could have an effect on the lithium plating in graphite electrodes under fast-charging conditions. Additionally, the effect of electrolyte additives and temperature dependence of the lithium deposition mechanism would be of great interest to provide insights into the fast-charging behaviour of silicon anodes.

# Bibliography

[1] Kevin G. Gallagher, Stephen E. Trask, Christoph Bauer, Thomas Woehrle, Simon F. Lux, Matthias Tschech, Peter Lamp, Bryant J. Polzin, Seungbum Ha, Brandon Long, Qingliu Wu, Wenquan Lu, Dennis W. Dees, and Andrew N. Jansen. Optimizing areal capacities through understanding the limitations of lithium-ion electrodes. *Journal of The Electrochemical Society*, 163(2):A138–A149, 2015.

[2] Qianqian Liu, Chunyu Du, Bin Shen, Pengjian Zuo, Xinqun Cheng, Yulin Ma, Geping Yin, and Yunzhi Gao. Understanding undesirable anode lithium plating issues in lithium-ion batteries. *RSC Advances*, 6(91): 88683–88700, 2016.

[3] Rosamaria Fong, Ulrich Von Sacken, and Jeff R Dahn. Studies of lithium intercalation into carbons using nonaqueous electrochemical cells. *Journal of The Electrochemical Society*, 137(7):2009, 1990.

[4] Thomas Waldmann and Margret Wohlfahrt-Mehrens. Effects of rest time after Li plating on safety behavior—ARC tests with commercial high-energy 18650 Li-ion cells. *Electrochimica Acta*, 230:454–460, 2017.

[5] Namhyung Kim, Sujong Chae, Jiyoung Ma, Minseong Ko, and Jaephil Cho. Fast-charging high-energy lithium-ion batteries via implantation of amorphous silicon nanolayer in edge-plane activated graphite anodes. *Nature communications*, 8(1):1–10, 2017.

[6] Baris Key, Rangeet Bhattacharyya, Mathieu Morcrette, Vincent Seznec, Jean-Marie Tarascon, and Clare P Grey. Real-time NMR investigations of

structural changes in silicon electrodes for lithium-ion batteries. *Journal of the American Chemical Society*, 131(26):9239–9249, 2009.

[7] Michel Letellier, Frédéric Chevallier, Christian Clinard, Elzbieta Frackowiak, Jean-Noël Rouzaud, Francois Beguin, Mathieu Morcrette, and Jean-Marie Tarascon. The first in situ $^7$Li nuclear magnetic resonance study of lithium insertion in hard-carbon anode materials for Li-ion batteries. *The Journal of Chemical Physics*, 118(13):6038–6045, 2003.

[8] Oliver Pecher, Paul M Bayley, Hao Liu, Zigeng Liu, Nicole M Trease, and Clare P Grey. Automatic Tuning Matching Cycler (ATMC) in situ NMR spectroscopy as a novel approach for real-time investigations of Li-and Na-ion batteries. *Journal of Magnetic Resonance*, 265:200–209, 2016.

[9] J Arai, Y Okada, T Sugiyama, M Izuka, K Gotoh, and K Takeda. In situ solid state $^7$Li NMR observations of lithium metal deposition during overcharge in lithium ion batteries. *Journal of The Electrochemical Society*, 162(6):A952–A958, 2015.

[10] Annica I Freytag, Allen D Pauric, Sergey A Krachkovskiy, and Gillian R Goward. In Situ Magic-Angle Spinning $^7$Li NMR Analysis of a Full Electrochemical Lithium-Ion Battery Using a Jelly Roll Cell Design. *Journal of the American Chemical Society*, 141(35):13758–13761, 2019.

[11] Annica I. Freytag, Allen D. Pauric, Meng Jiang, and Gillian R. Goward. $^7$Li and $^{29}$Si NMR Enabled by High-Density Cellulose-Based Electrodes in the Lithiation Process in Silicon and Silicon Monoxide Anodes. *The Journal of Physical Chemistry C*, 123(18):11362–11368, 2019.

[12] Keitaro Kitada, Oliver Pecher, Pieter C. M. M. Magusin, Matthias F. Groh, Robert S. Weatherup, and Clare P. Grey. Unraveling the reaction mechanisms of SiO anodes for Li-ion batteries by combining in situ $^{7}$Li and ex situ $^{7}$Li/$^{29}$Si solid-state NMR spectroscopy. *Journal of the American Chemical Society*, 141(17):7014–7027, 2019.

[13] Sergey A. Krachkovskiy, Jamie M. Foster, J. David Bazak, Bruce J. Balcom, and Gillian R. Goward. Operando Mapping of Li Concentration Profiles and Phase Transformations in Graphite Electrodes by Magnetic Resonance Imaging and Nuclear Magnetic Resonance Spectroscopy. *The Journal of Physical Chemistry C*, 122(38):21784–21791, 2018.

[14] Katharina Märker, Chao Xu, and Clare P. Grey. Operando NMR of NMC811/graphite lithium-ion batteries: Structure, dynamics, and lithium metal deposition. *Journal of the American Chemical Society*, 2020.

[15] Andrés Ramírez Aguilera, Bryce MacMillan, Gillian R. Goward, and Bruce J. Balcom. Optimization of a parallel-plate RF probe for high resolution thin film imaging. *Concepts in Magnetic Resonance Part A*, 47A(1):e21465, 2018.

[16] Sergey A. Krachkovskiy, Mohammad Reza, Andres Ramirez Aguilera, Ion C. Halalay, Bruce J. Balcom, and Gillian R. Goward. Real-time quantitative detection of lithium plating by in situ NMR using a parallel-plate resonator. *Journal of The Electrochemical Society*, 167(13):130514, 2020.

[17] Mark D Meadowcroft, Shutong Zhang, Wanzhan Liu, Bu Sik Park, James R Connor, Christopher M Collins, Michael B Smith, and Qing X Yang.

Direct magnetic resonance imaging of histological tissue samples at 3.0 T. *Magnetic Resonance in Medicine: An Official Journal of the International Society for Magnetic Resonance in Medicine*, 57(5):835–841, 2007.

[18] SGJ van Meerten, WMJ Franssen, and APM Kentgens. ssNake: A cross-platform open-source NMR data processing and fitting application. *Journal of Magnetic Resonance*, 301:56–66, 2019.

## Chapter 6

# Outlook

## 6.1 Summary and Conclusion

In this work, new methods for in situ NMR for battery materials were developed and successfully applied to relevant questions in the LIB research field. In the following short summaries of the individual chapters with the emphasis of their importance for the advancement of in situ NMR techniques for battery materials is given.

In Chapter 3 a combination of ex situ $^{29}$Si NMR and ex situ $^{7}$Li NMR was used to investigate the lithiation of silicon (Si) and silicon monoxide (a-SiO). This was made possible by using cellulose-based electrodes, which allowed for an increased active material filling factor in both ex situ and in situ measurements. In situ $^{7}$Li NMR data revealed the formation of amorphous lithium silicides in both Si and a-SiO. Interestingly, at high levels of lithiation, phase 3 silicides were absent in a-SiO. This type of silicide is known to be the major culprit of volumetric expansion in silicon anodes and its absence in a-SiO supports the claim that it shows better long-term cyclability compare to Si anodes. This finding was further investigated through ex situ $^{29}$Si NMR, which revealed that the lithiated domains in a-SiO are of less metallic nature than in Si. For the first time, a combined study of both ex situ $^{29}$Si and in situ $^{7}$Li NMR was conducted and allowed for the characterization and comparison of the lithiated phases in a-SiO and Si.

Chapter 4 introduces a novel in situ NMR technique, which enables the use of magic-angle spinning (MAS). The challenges in assembling an electrochemical cell include, but are not limited to, reducing the amount of metallic components in the cell, optimizing magic-angle spinning stability and applying advanced NMR techniques to increase the resolution of the sites in the NMR spectrum. A tool was designed, which made it possible to assemble an electrochemical cell with high reproducibility by mimicking a commercial roll-to-roll mechanism. The assembled electrochemical cell fits into a 4 mm MAS rotor, which allowed NMR experiments up to a spin rate of 10 kHz. Spinning stability was ensured by using minimal metallic components such as cellulose-based electrodes (introduced in Chapter 3) and titanium wire as current collectors. A proof-of-concept study was performed, which utilized graphite and $LiCoO_2$ as electrode materials in a full-cell format. $^{7}$Li NMR spectra were collected during charge and discharge of the cell revealing all active lithium species in the cell. The clever yet simplistic design makes it possible to implement this technique in other research labs and lays the foundation for in situ MAS NMR of battery materials, which has been demonstrated for the first time in this work. Additionally, by combining this in situ cell with sophisticated NMR techniques such as MATPASS, it should be possible to investigate a variety of electrode materials even at moderate spin rates.

Chapter 5 deals with the analysis of silicon anodes under fast-charging conditions using a novel parallel-plate resonator design for in situ NMR. This type of resonator allows for an even $B_1$ field distribution inside a rectangular electrochemical cell. Silicon anodes were investigated under different charge rates (1C, C/4, and 2C) through this method and gave insights into the lithium plating behaviour when high currents were applied. Lithium plating only occurred when large overpotentials were apparent in the cell, which was mostly attributed to the in situ cell design. Further improvements of the design will allow for increased pressure throughout the cell, which is currently under way in the Goward group. However, using this parallel-plate resonator design it was shown, that magnetic resonance imaging is possible and that the distribution of electrolyte and plated lithium can be imaged through this technique. This is of great interest for the battery community as it gives a non-invasive way to track the formation of lithium species inside the cell.

In this work new in situ NMR techniques for battery monitoring were introduced. It was shown that these techniques can be used to tackle relevant questions in the field of battery research. In addition, the importance of developing new in situ NMR methods was highlighted. In situ NMR is a non-invasive technique with endless possibilities to be used in the analysis of lithium-ion batteries.

## 6.2 Future Avenues

Further improvements to the above introduced cell designs are necessary to perform in operando measurements. The technique introduced in Chapter 4 still requires the removal of the battery/rotor from the NMR probe to perform electrochemical cycling. Possible adjustments to the design to make this technique truly in operando include the incorporation of a solid-state polymer electrolyte (PE) instead of the liquid electrolyte currently used. In Appendix A a PE is analyzed through PFG NMR to obtain diffusion coefficients for a quaternary PE, which shows good diffusional properties at elevated temperatures. It should be possible to replace the liquid electrolyte and separator with the PE using the roll-to-roll mechanism developed in Chapter 4. The cell can then be cycled at elevated temperatures and should eliminate the refilling of liquid electrolyte after applying magic-angle spinning. This requires modification of the cellulose-based electrodes, which need to be prepared with a co-binder like PEO:LiTFSI to increase the interfacial electrode/electrolyte contact. Additionally, a contactless charging/discharging mechanism will have to be developed in order to cycle the cell inside the NMR magnet. First steps could include adding a resistor to the rotor cap after charging the cell in the glove box and monitor the discharge in operando. In order to charge <u>and</u> discharge the cell inside the magnet further improvements could include a wireless charging mechanism, which utilizes a type of photovoltaic element and a light source to charge the cell when the light source is turned on, and discharge when the light source is turned off. This would allow for an in operando measurement under MAS conditions.

The cell design in Chapter 5 has room of improvement as well. The large discrepancies of the electrochemical cycling results to coin cell data indicates that the cell pressure in the in situ cell is uneven, which leads to large overpotentials in the cell. This needs to be overcome to obtain reliable and reproducible data in order to properly quantify the lithium inventory in all active species through in situ $^{7}$Li NMR. In addition, solvent leakage is a great issue in these types of cells. It would be of great interest to expand the tuning range of the parallel-plate resonator to other nuclei such as $^{1}$H so that the solvent distribution inside these cells can be monitored accurately. Furthermore, to monitor the potentials on both anode and cathode, it is crucial to incorporate a reference electrode to the cell, so that NMR results can be directly compared to electrochemical results. An improved design, which addressed these issues should give more accurate results for fast-charging batteries and can potentially be used to monitor batteries in real-time in a non-invasive way.

## Appendix A

# PFG Analysis of a Polymer-Rich Quaternary Composite Solid Electrolyte for Lithium Batteries

*The following chapter is adapted from a publication published in the Journal of the Electrochemical Society (J. Electrochem. Soc. 2020, 167, 070557).*[1] *Annica I. Freytag collected the PFG $^7$Li NMR data and performed the data analysis. Hilal Al-Salih conducted the synthesis and electrochemical analysis of the polymer electrolytes as well as the conductivity study.*

This project was a collaborative study on designing and characterizing a quaternary composite solid-state electrolyte (CSE) which consists of a solid electrolyte ($Li_{0.33}La_{0.55}TiO_3$, LLTO) and a polymer electrolyte (Poly(ethylene oxide):Lithium bis(tri-fluoromethanesulfonyl)imide, PEO:LiTFSI) along with a solid plasticizer (Succinonitrile, SN). For detailed information on the materials used, preparation of the CSE films and other characterization techniques the reader is referred to the publication.[1] In the following, the NMR study is presented. The long-term goal for this study is to find a suitable polymer electrolyte for the in situ MAS project. The most important properties include bendability, excellent conductive and diffusive properties, and the possibility to incorporate it into electrochemical cells.

## A.1 Introduction

All-solid-state batteries continue to grow as an alternative to replace the traditional liquid-based ones not only because they provide increased safety but also higher power and energy densities. However, current solid-state electrolytes are either ceramics that are brittle but highly conducting (e.g., LLTO) or polymer electrolytes that are poorly conducting but form flexible films with desired mechanical properties (e.g., PEO:LiTFSI). In this work, we have developed a quaternary CSE to combine the benefits of the two types along with SN as a solid plasticizer. The CSE has been characterized using pulsed-field gradient (PFG) $^7$Li NMR. The CSE was integrated into a solid-state coin-type cell cathode which shows good cycling performance at C/20 and 55 °C maintaining specific discharge capacity at 143.2 mA h g$^{-1}$ after 30 cycles. This newly formulated quaternary CSE is proven to give the best combination of properties and should give new insights in the synthesis approach of quaternary CSEs with different chemistry.

## A.2 Experimental

NMR measurements were performed on a 300 MHz spectrometer fitted with a variable temperature unit using a Diff50 probe. For $^7$Li NMR measurements the CSE film (70 wt% PEO, 12 wt% LiTFSI, 9 wt%, LLTO and 9 wt% SN) was cut into a rectangular sheet and rolled up to fit inside a 4 mm magic-angle spinning rotor. The rotor was then inserted into a 5 mm NMR tube. This allows for easy cleaning of the NMR tube and even distribution of the sample inside the spectrometer. The film was then heated at 75°C for 4 h inside the magnet before conducting diffusion measurements. Measurements were performed between 30°C–70°C. A 20-minute waiting period was included before conducting diffusion measurements to allow for the sample to equilibrate at the correct temperature (range: 30°C–70°C). A stimulated echo gradient pulse sequence as introduced in Chapter 2.5.1 was used with the gradient length $\delta$ fixed at 2.5 ms and the diffusion time $\Delta$ set between 30–200 ms. The b value ($g^2\gamma^2\delta^2\,(\Delta - \delta/3)$ term in Equation 2.23) was kept constant for each temperature by varying the applied gradient strength and the diffusion time. The number of scans varied between 32 and 1024 scans with the gradient steps being kept constant at 32. Recycle delays were set between 1.0–2.5 s. $T_2$ relaxation of LLTO is approximately an order of magnitude smaller than in LiTFSI, leading to a filtering of the LLTO signal under the above conditions. Solely the dynamics of LiTFSI in the polymer matrix is observed in this study. Diffusion data sets were fit using a single or (where applicable) multi-component fit in Matlab.

## A.3 Results

Diffusion behaviour of PEO-containing polymer electrolytes has been studied extensively in the past.[2] Detailed dynamic NMR studies have revealed the dependence of the cation mobility on the morphology of the polymer matrix.[3,4] It has been shown that an increase in amorphous domains leads to a better-connected conductive network. In particular, the polymer chain motion is

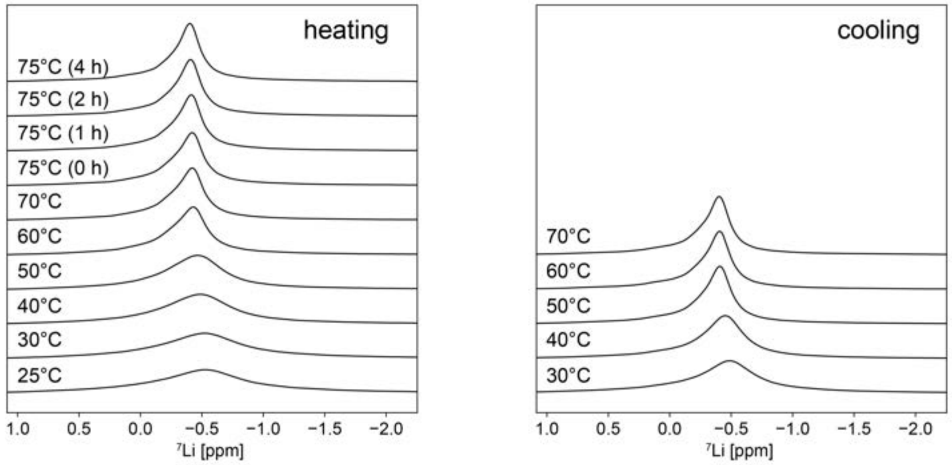

Figure A.1: $^{7}$Li NMR spectra of the CSE film as a function of temperature during heating cycle (left) and cooling cycle (right).

essential in facilitating ionic diffusion in polymer electrolytes.[5,6] $^{7}$Li NMR spectroscopy was performed for the CSE film to gain insight on the interaction and ion dynamics at different temperatures. The spectra shown in Figure A.1 reveal a single, broad peak throughout the heating and cooling cycles which is attributed to the LiTFSI species. The linewidth decreases with increasing temperature indicating a change in ion mobility due to the increase in amorphicity of the polymer network at high temperatures.

$^{7}$Li PFG NMR was performed in order to investigate the diffusion in the CSE film. Diffusion curves were obtained in the range of 30 °C to 70 °C. Example diffusion curves and their respective fits are shown in Figure A.2. At high temperatures a single diffusion process dominates, allowing for an accurate single-component fit while a single-component fit is not appropriate at lower temperatures. Figure A.2c shows an example for a two-component fit, which utilizes a breakpoint fit procedure to extract the two different diffusion coefficients from the linearized data.

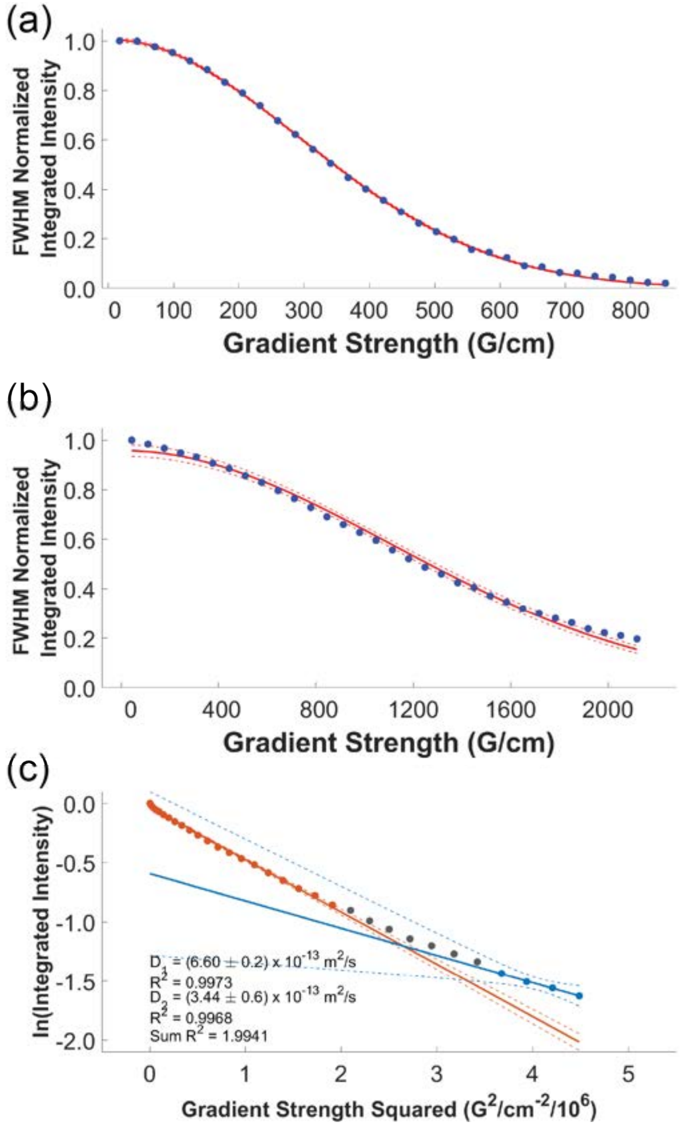

Figure A.2: Example fit of diffusion data for the 70 wt% PEO, 12 wt% LiTFSI, 9 wt%, LLTO and 9 wt% SN composite solid electrolyte at (a) 337 K using a single-component fit (b) at 305 K using a single-component fit (c) linearized diffusion data fit using a two-component fit at 305 K

Figure A.3a shows the diffusion coefficients extracted from the fits in Figure A.2. At high temperatures (55 °C to 70 °C) a linear dependence is apparent while at intermediate temperatures a coexistence of two components with slightly different diffusivities is apparent. It is evident, that there is a significant

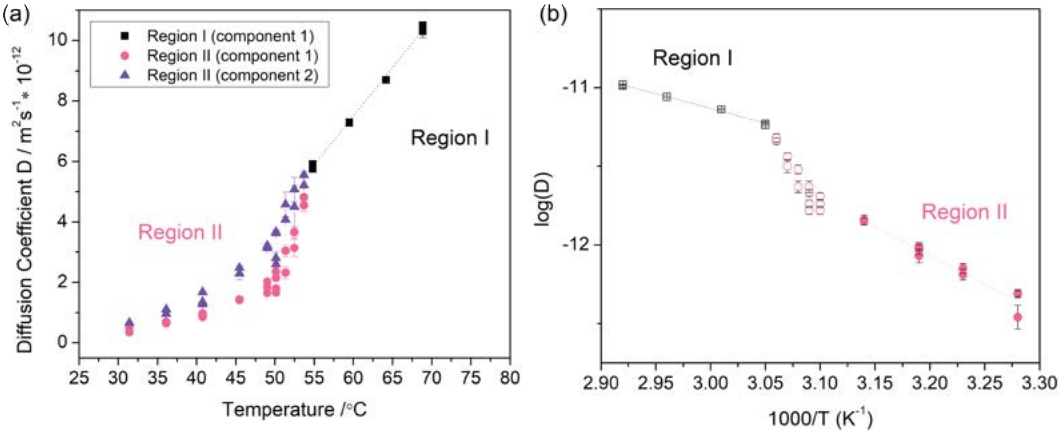

Figure A.3: (a) Diffusion coefficients of the CSE film as a function of temperature (b) Arrhenius plot of the diffusion coefficient of the CSE film.

change in the diffusion behaviour between 45 °C to 55 °C. This is in agreement with the change of morphology around the transition temperature of PEO (PEO's transition temperature is at 65 °C), where presumably regions with varying degree of crystallinity are apparent. This gradual phase change is observed around 50 °C, which shows as a deviation from linear behaviour in the Arrhenius plot in Figure A.3b. These two different regions have contrasting diffusion behavior with activation energies for region I and region II of 38±1 kJ/mol and 67±6 kJ/mol, respectively. The change in activation energy with temperature is in line with what is observed in the Arrhenius plots obtained from ionic conductivity measurements (Figure A.4) and can be attributed to the polymer morphology which has a significant influence on the diffusion pathways. This might indicate that in polymer-rich CSE composites the ionic conductivity is dominated by the polymer dynamics and not the ceramic as was shown by Zheng et al.[7] for LLZO:PEO composites where tracking of Li ion pathways at higher ceramic content proved the dominance of ceramic related pathways.

To assess the electrochemical performance of the CSE film, 2325 coin-type

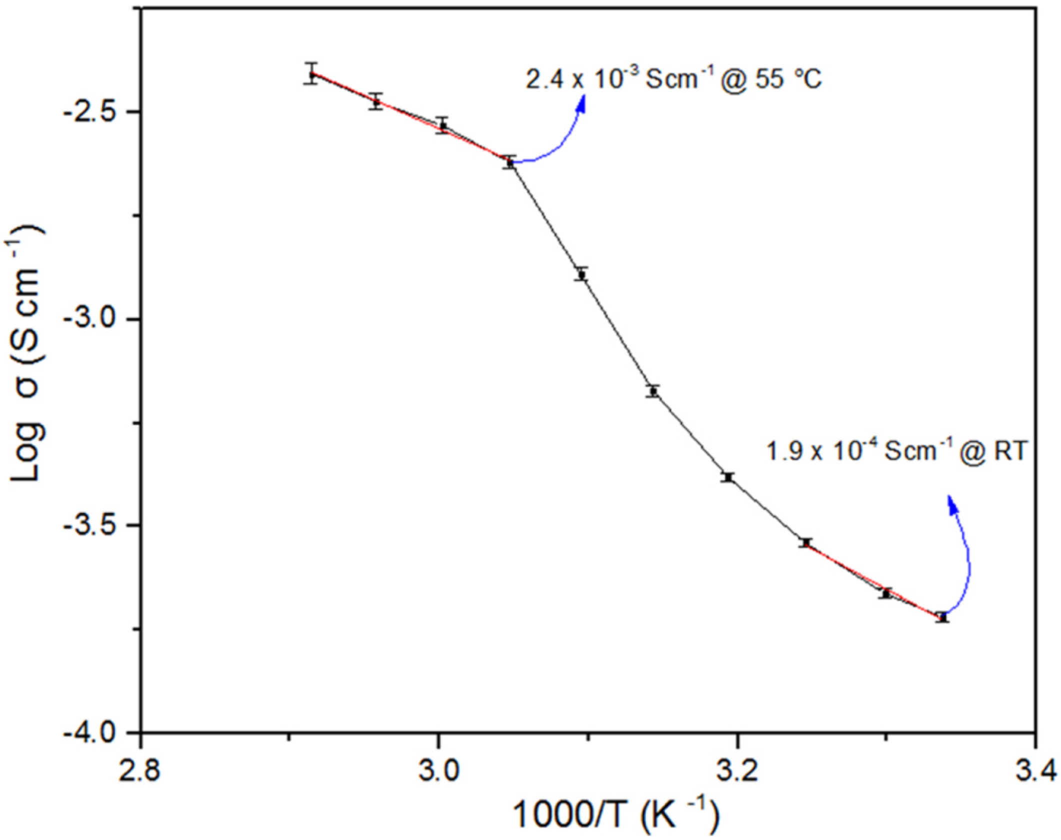

Figure A.4: Conductivity vs T "Arrhenius plot" of the 10S CSE film.

cells were assembled by sandwiching the film between a $LiNi_{0.5}Mn_{0.3}Co_{0.2}O_2$ (NMC532) cathode (fabricated following common procedures of mixing NMC532 powder with PVDF binder and a carbon additive) and a lithium disc. Charge-discharge tests were then carried out in the potential range of 2.5–4.2 V at 55°C and at a cycling rate of C/20. These cells showed poor cycling performance and provided an initial discharge capacity of only $7\,mA\,h\,g^{-1}$. This is mainly attributed to the poor interfacial contact between the cathode and the electrolyte and the internal resistance inside the cell which was calculated to be 2030±10 Ω. To improve the interfacial resistance, we assembled new coin-type cells which employs our in-house made cathode that utilizes PEO:LiTFSI (2:1) as a co-binder to help improve the cathode/electrolyte interfacial contact. Figure

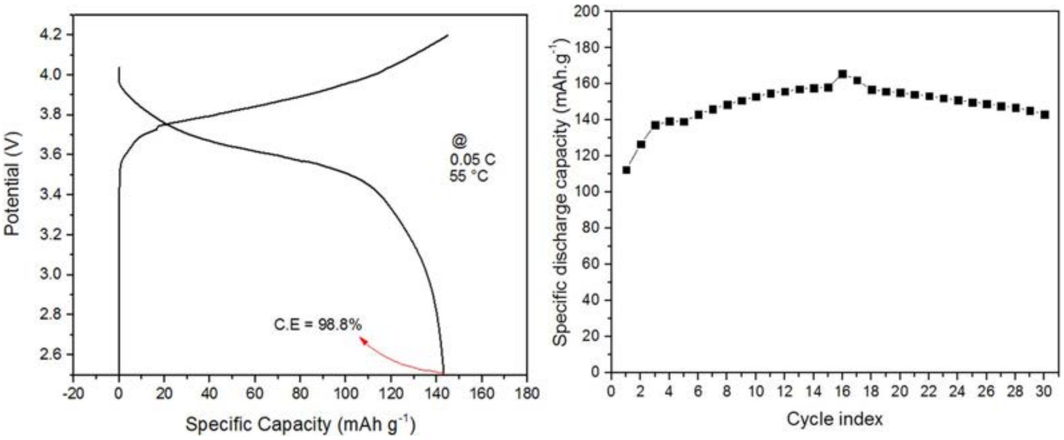

Figure A.5: Charge-discharge curve of the CSE film at 0.05 C and 55°C (left) and cycling performance at 55°C (right)

A.5 shows the charge-discharge curve and the cycling performance. Notably, the specific discharge capacity improved significantly to values closer to the known experimental values (around 150 mAhg$^{-1}$). The initial capacity reached 112 mAhg$^{-1}$ then it kept on increasing for the first 16 cycles which indicates the continuous homogenization of the components inside the composite and at the interface inside the battery. After 30 cycles, the battery discharge capacity reached 143.2 mAhg$^{-1}$ and the columbic efficiency achieved was 98.8%.

## A.4 Conclusion

A polymer-rich quaternary composite solid-state electrolyte composed of PEO-LiTFSI-LLTO-SN was characterized through PFG NMR. It was shown, that at temperatures of 55°C and above a change in morphology and therefore an increase in diffusivity and conductivity is apparent. This can be attributed to the formation of more amorphous regions in this CSE due to the use of a plasticizer like SN.

A coin-cell battery was fabricated by incorporating PEO:LiTFSI as a binder in the NMC 532-based cathode. This was essential to overcome the cathode-electrolyte interfacial resistance issue. The discharge capacity achieved by the battery Li/CSE/NMC 532 after 30 cycles was 143.2 mAhg$^{-1}$ at C/20 and 55°C. We can conclude that quaternary CSEs are promising candidate for next-generation solid-state lithium batteries and in particular a great candidate for the use in an in situ MAS cell. It should be possible to integrate this CSE instead of the separator which would be a great step towards an in operando type setup. However, this requires modification of the cellulosic-based electrodes used in the current cells (addition of a PEO:LiTFSI binder), which will need to be optimized under these new conditions.

# Bibliography

[1] Hilal Al-Salih, Allan Huang, Chae-Ho Yim, Annica I. Freytag, Gillian R. Goward, Elena Baranova, and Yaser Abu-Lebdeh. A polymer-rich quaternary composite solid electrolyte for lithium batteries. *Journal of The Electrochemical Society*, 167(7):070557, 2020.

[2] Stephen Munoz and Steven Greenbaum. Review of Recent Nuclear Magnetic Resonance Studies of Ion Transport in Polymer Electrolytes. *Membranes*, 8(4):120, 2018.

[3] W Gorecki, M Jeannin, E Belorizky, C Roux, and M Armand. Physical properties of solid polymer electrolyte PEO(LiTFSI) complexes. *Journal of Physics: Condensed Matter*, 7(34):6823–6832, 1995.

[4] C. Berthier, W. Gorecki, M. Minier, M.B. Armand, J.M. Chabagno, and P. Rigaud. Microscopic investigation of ionic conductivity in alkali metal salts-poly(ethylene oxide) adducts. *Solid State Ionics*, 11(1):91–95, 1983.

[5] J. P. Donoso, T. J. Bonagamba, H. C. Panepucci, L. N. Oliveira, W. Gorecki, C. Berthier, and M. Armand. Nuclear magnetic relaxation study of poly(ethylene oxide)–lithium salt based electrolytes. *The Journal of Chemical Physics*, 98(12):10026–10036, 1993.

[6] Wladimir Gorecki, Christel Roux, Martin Clémancey, Michel Armand, and Elie Belorizky. NMR and conductivity study of polymer electrolytes in the imide family: P(EO)/Li[N($SO_2C_nF_{2n+1}$)($SO_2C_mF_{2m+1}$)]. *ChemPhysChem*, 3(7):620–625, 2002.

[7] Jin Zheng, Mingxue Tang, and Yan-Yan Hu. Lithium ion pathway within $Li_7La_3Zr_2O_{12}$-polyethylene oxide composite electrolytes. *Angewandte Chemie International Edition*, 55(40):12538–12542, 2016.

## Appendix B

# In Situ $^7$Li NMR Analysis of Silicon Anodes in Full Cells under Fast-Charging Conditions using a Parallel-Plate Resonator

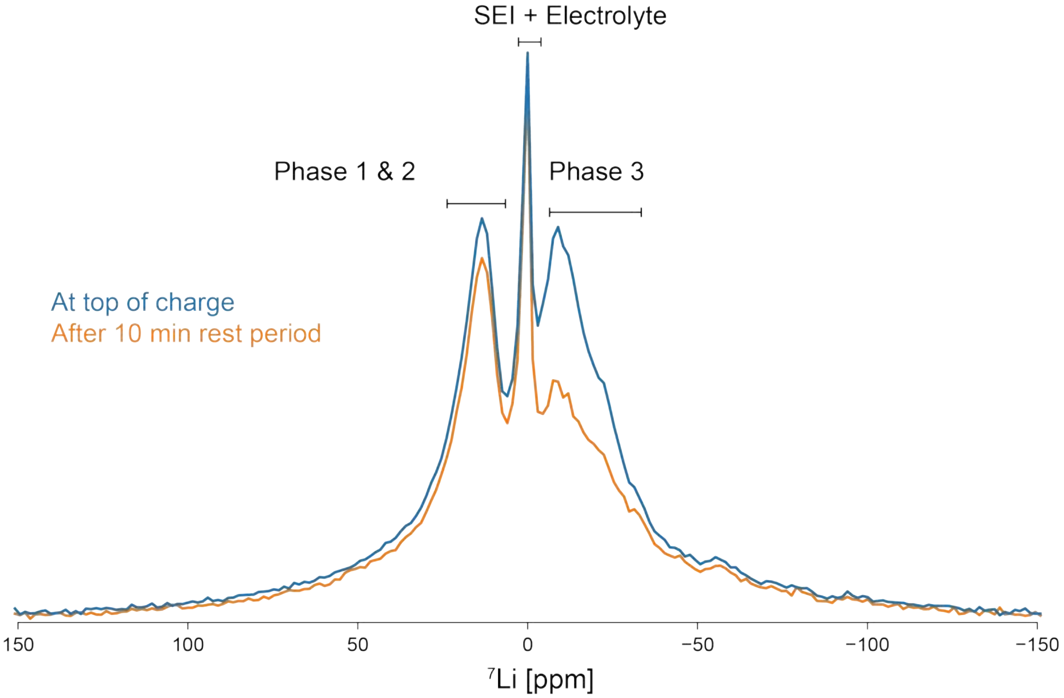

Figure B.1: Comparison of top of charge $^7$Li NMR spectrum to after a 10 minutes rest period for cell A after the C/4 charge.

```
# -*- coding: utf-8 -*-
"""
Created on Sun Oct  4 18:26:57 2020

@author: Annica Freytag
"""

import numpy as np
import scipy as sc
import matplotlib.pyplot as plt
import scipy.io as sio
from numpy import loadtxt


file1 = np.matrix.transpose(loadtxt("in_situ_2409_2.txt",delimiter='\t'))
#file2 = np.matrix.transpose(loadtxt("PP_28092020_11_12_2.txt",delimiter='\t'))

max1 = np.amax(file1)
#max2 = np.amax(file2)

file1 = file1/max1
#file2 = file2/max2
#lines1 = file1.read().split('\t')


#x1 = np.array([0.084,0.168,0.252,0.336,0.42,0.504,0.588,0.672,0.756,0.84,0.924,1.008,1.092,1.176,
#y1 = np.array([0.125,0.25,0.375,0.5,0.625,0.75 ,0.875,1,  1.125, 1.25,1.375,1.5,1.625,1.75,1.875  ,

x = np.linspace(-1430,1633,2048)
y = np.linspace(31.2,0,22)
#level = np.array([0,1,2,3,4,5,6,7,8,9,10])/10
level = np.linspace(-0.01,1,100)

fig1,ax1 = plt.subplots(figsize=(8,6))
plt.xticks(fontsize=12) #sets tick step size to 0.4
plt.yticks(fontsize=12)
cs = ax1.contourf(x,y,file1,level,cmap='jet', fontsize=18)
artists, labels = cs.legend_elements()

ax1.set_xlim([50,-50])
ax1.set_xlabel("$^7$Li Chemical Shift (ppm)", fontsize=18)
ax1.set_ylabel("Charge Capacity (mAh)", fontsize=18)

fig1.colorbar(cs,format="%.1f")
#cs2 = ax1[1].contourf(x,y,file1,level,cmap='RdYlBu_r', fontsize=18)
#ax1[1].set_xlim([100,-100])
#ax1[1].set_xlabel("Shift (ppm)", fontsize=18)
#plt.legend(artists, labels, handleheight=2)
plt.savefig('1709_in_situ_2409_zoom.svg')

plt.show()
```

1

Figure B.2: Spyder code to plot in situ data as a contour plot

## B.1 Chemical Shift Imaging Pulse Sequence Program

```
prosol relations=<triple>
#include <Avance.incl>
#include <Grad.incl>
#include <Delay.incl>
define list<gradient> diff=<sprite>
define list<gradient> diff2=<sprite_DI>
"p2=p1*2"
"d21=d20-de"
"acqt0=-p1*2/3.1416"
1 ze
2 d1 pl1:f1
3 p1 ph1
20u UNBLKGRAMP
p30:gp6*diff2
d20 BLKGRAMP
p1 ph1
2u
p2 ph2
2u
p1 ph1
20u UNBLKGRAMP
p30:gp7*-1*diff
d21 BLKGRAMP
```

```
go=2 ph31
30m mc #0 to 2
F1QF(igrad diff)
F2QF(igrad diff2) exit
ph1=0 0 1 1 2 2 3 3 ;x
ph2=1 3 0 2 3 1 2 0 ;y
ph31=0 0 1 1 2 2 3 3 ;follows 90
;pl1 : f1 channel - power level for pulse (default)
;p1 : f1 channel - high power pulse
;p19: gradient pulse 2 (spoil gradient)
;p30: gradient pulse (little DELTA)
;d1 : relaxation delay; 1-5 * T1
;d16: delay for gradient recovery
;d20: diffusion time (big DELTA)
;ns: 2 * n
;td1: number of experiments
;FnMODE: QF
; use xf2 and DOSY processing
;for z-only gradients:
;use gradient files:
;gpnam6: SMSQ10.100
```